

# ABSTRACT

Title of dissertation:      MECHANICAL CHARACTERIZATION OF  
NORMAL AND CANCEROUS BREAST  
TISSUE SPECIMENS USING ATOMIC  
FORCE MICROSCOPY

Rajarshi Roy

Dissertation directed by:   Professor Jaydev P. Desai  
Department of Mechanical Engineering,  
Robotics, Automation, and Medical  
Systems (RAMS) Laboratory.

Breast cancer is one of the most common malignancies among women worldwide. Conventional breast cancer diagnostic methods involve needle-core biopsy procedures, followed by careful histopathological inspection of the tissue specimen by a pathologist to identify the presence of cancerous lesions. However, such inspections are primarily qualitative and depend on the subjective impressions of observers. The goal of this research is to develop approaches for obtaining quantitative mechanical signatures that can accurately characterize malignancy in pathological breast tissue. The hypothesis of this research is that by using contact-mode Atomic Force Microscopy (AFM), it is possible to obtain differentiable measures of stiffness of normal and cancerous tissue specimens.

This dissertation summarizes research carried out in addressing key experimental and computational challenges in performing mechanical characterization on breast tissue. Firstly, breast tissue specimens studied were 600  $\mu\text{m}$  in diameter,

about six times larger than the range of travel of conventional AFM X-Y stages used for imaging applications. To scan tissue properties across large ranges, a semi-automated image-guided positioning system was developed that can be used to perform AFM probe-tissue alignment across distances greater than  $100\text{ }\mu\text{m}$  at multiple magnifications. Initial tissue characterization results indicate that epithelial tissue in cancer specimens display increased deformability compared to epithelial tissue in normal specimens. Additionally, it was also observed that the tissue response depends on the patient from whom the specimens were acquired.

Another key challenge addressed in this dissertation is accurate data analysis of raw AFM data for characterization purposes. Two sources of uncertainty typically influence data analysis of AFM force curves: the AFM probe's spring constant and the contact point of an AFM force curve. An error-in-variable based Bayesian Changepoint algorithm was developed to quantify estimation errors in the tissue's elastic properties due to these two error sources. Next, a parametric finite element modeling based approach was proposed in order to account for spatial heterogeneity in the tissue response. By using an exponential hyperelastic material model, it was shown that it is possible to obtain more accurate material properties of tissue specimens as opposed to existing analytical contact models.

The experimental and computational strategies proposed in this dissertation could have a significant impact on high-throughput quantitative studies of biomaterials, which could elucidate various disease mechanisms that are phenotyped by their mechanical signatures.

MECHANICAL CHARACTERIZATION OF NORMAL AND  
CANCEROUS BREAST TISSUE SPECIMENS USING ATOMIC  
FORCE MICROSCOPY

by

Rajarshi Roy

Dissertation submitted to the Faculty of the Graduate School of the  
University of Maryland, College Park in partial fulfillment  
of the requirements for the degree of  
Doctor of Philosophy  
2014

Advisory Committee:

Professor Jaydev P. Desai, Chair

Professor Carol Keefer, Dean's Representative

Professor Balakumar Balachandran

Professor Nikhil Chopra

Professor Teng Li

© Copyright by  
Rajarshi Roy  
2014

1. Portions reprinted, with permission, from: **Rajarshi Roy**, Wenjin Chen, Lauri Goodell, Jun Hu, David J. Foran and Jaydev P. Desai, “Microarray-facilitated Mechanical Characterization of Breast Tissue Pathology Samples using contact mode Atomic Force Microscopy (AFM)”, *International Conference on Biomedical Robotics and Biomechatronics* pp. 710 - 715, 2010.
2. Portions reprinted, with permission, from: **Rajarshi Roy**, Wenjin Chen, Lei Cong, Lauri Goodell and David J. Foran, Jaydev P. Desai, “Towards Automated Mechanical Characterization of Biological Samples using Atomic Force Microscopy (AFM)”, *2011 ASME Dynamic Systems and Control Conference*, November 2011.
3. Portions reprinted, with permission, from: **Rajarshi Roy**, Lei Li, Carol L. Keefer and Jaydev P. Desai, “An Error-In-Variables (EIV) based Bayesian Probabilistic Approach to Estimating Cell Mechanical Properties using Atomic Force Microscopy”, *International Conference on Biomedical Robotics and Biomechatronics*, pp. 389–394, June 2012.
4. Portions reprinted, with permission, from: **Rajarshi Roy**, Wenjin Chen, Lei Cong, Lauri Goodell, David J. Foran and Jaydev P. Desai, “A Semi-Automated Positioning System for contact-mode Atomic Force Microscopy (AFM)”, *IEEE Transactions on Automation Science and Engineering*, vol. 10 no. 2, pp. 462-465, 2013.
5. Portions reprinted, with permission, from: **Rajarshi Roy**, Wenjin Chen, Lei Cong, Lauri Goodell, David J. Foran and Jaydev P. Desai, “Probabilistic Estimation of Mechanical Properties of Biomaterials Using Atomic Force Microscopy”, *IEEE Transactions on Biomedical Engineering*, vol. 61 no. 2, pp. 547-556, 2014.

## Acknowledgments

I am deeply grateful to all those people who made this dissertation possible and made my graduate school experience something that I would cherish for the rest of my life.

Firstly, I would like to thank my advisor, Professor Jaydev P. Desai for giving me the opportunity to work in his laboratory on an extremely challenging project over the past five years. His enthusiasm, constant encouragement and patience, especially during my initial graduate school years, is something I am profoundly grateful for. He always made himself available, even at late nights, for troubleshooting with the AFM. It has been a pleasure to work and learn from him over the past five years.

I would also like to thank my collaborators, Dr. Wenjin Chen and Professor David J. Foran from the Rutgers Cancer Institute of New Jersey. Without their critical feedback at various stages of this project, this dissertation would not have been possible. It has been a pleasure to work and collaborate with them.

Next, I would like to thank Dr. Carol Keefer taking the time out of her busy schedule to teach me various intricacies of light microscopy and the components of optical microscopes. I could always count on her to provide me with lab accessories urgently whenever I ran out of them.

My colleagues at the Robotics, Automation and Medical Systems lab have been instrumental in enriching my graduate experience - I learnt a lot from them. Dr. Anand Pillarisetti helped me get acquainted with the AFM. Dr. U-Xuan Tan

provided great help when I was starting with the MP-285 micromanipulator. Dr. Mingyen Ho greatly assisted me with any computer hardware problems I had. I had a lot of fruitful discussions on computational modeling with Dr. Kevin Lister. It has been a pleasure discussing various aspects of this project with Dr. Yang Bo, Elif Ayvali, Chad Kessens, Hyuntae Kim and Dr. Hardik Pandya. I would like to express my gratitude to all members of the RAMS laboratory who have helped me during my graduate studies.

Special thanks to Mr. Melvin Fields for his prompt response with any computer related problems I had.

I would also like to thank Xavier Pelle, Suvajyoti Guha, Snehaunshu Chowdhury, Ishita Chakraborty, Sandip Biswas and Sagar Chowdhury for their friendship during these last five years.

I owe my deepest gratitude to my parents, who have constantly stood beside me through all the difficult phases I had during these last five years. The values and morals that I have imbibed from them kept me strong when the going got tough. Thank you!

I would also like to acknowledge the financial support from the National Science Foundation (NSF) and National Institutes of Health (NIH) for the research presented in this dissertation.

Lastly, I would like to apologize to those I've inadvertently left out. Thanks again!!

# Table of Contents

List of Tables	vi
List of Figures	vi
List of Abbreviations	xii
1 Introduction	1
1.1 Motivation . . . . .	1
1.2 Proposed Solution . . . . .	7
1.3 Organization . . . . .	9
2 Pilot Mechanical Characterization Studies on Breast Tissue Pathology sam- ples using Atomic Force Microscopy	10
2.1 Overview . . . . .	10
2.2 Material and Methods . . . . .	10
2.2.1 Tissue Microarray (TMA) preparation and Annotation . . . .	10
2.2.2 AFM experimental setup . . . . .	14
2.2.3 Contact-mode operation of AFM . . . . .	16
2.2.4 Operating modes for AFM indentation . . . . .	19
2.2.4.1 Deflection-controlled AFM force curves . . . . .	19
2.2.4.2 Indentation-controlled AFM force curves . . . . .	21
2.2.5 Data Analysis . . . . .	23
2.3 Results and Discussions . . . . .	26
2.4 Conclusions . . . . .	30
3 Improvements to the AFM experimental protocol for tissue characterization	33
3.1 Overview . . . . .	33
3.2 Problem Statement and Proposed Solution . . . . .	34
3.3 AFM experimental setup with the IGPS . . . . .	39
3.4 Image-Guided Navigation . . . . .	40
3.4.1 Tracking of the ROI . . . . .	40
3.4.2 Control Scheme . . . . .	43
3.5 ROI positioning protocol . . . . .	45
3.6 Results and Discussion . . . . .	49
3.6.1 Characterization of Epithelium-Stroma boundary . . . . .	49
3.6.2 Characterization of patient specific tissue specimens . . . . .	53
3.7 Conclusions . . . . .	55
4 Probabilistic Estimation of the Elastic Modulus	58
4.1 Overview . . . . .	58
4.2 Problem Statement and Proposed Solution . . . . .	59
4.2.1 Uncertainty in the contact Point . . . . .	59
4.2.2 Uncertainty in AFM Probe Calibration . . . . .	64

4.3	Bayesian Analysis . . . . .	71
4.3.1	Transformation of raw data . . . . .	71
4.3.2	Classical Error-In-Variables Model . . . . .	75
4.3.3	EIV-based Changepoint Modeling: Likelihood . . . . .	77
4.3.4	EIV-based Changepoint Modeling: Posterior . . . . .	81
4.3.5	EIV-based Changepoint Modeling: Gibbs Sampling . . . . .	82
4.4	Results and Discussions . . . . .	87
4.4.1	Implementation of the Gibbs Sampler . . . . .	87
4.4.2	Simulated Data . . . . .	88
4.4.3	AFM studies on histological breast tissue . . . . .	92
4.4.4	Sensitivity Analysis . . . . .	96
4.4.4.1	Varying $\sigma_{sp}$ . . . . .	96
4.4.4.2	Varying $\mu_{sp}$ . . . . .	98
4.5	Conclusions . . . . .	99
5	Constitutive material modeling of the tissue specimens under AFM indentation . . . . .	104
5.1	Overview . . . . .	104
5.2	Experimental Challenges in enforcing Hertzian assumptions . . . . .	105
5.3	Related Work . . . . .	109
5.4	Problem Statement and Proposed Solution . . . . .	116
5.5	Finite Element Modeling . . . . .	121
5.5.1	Discretization and Parameter Estimation . . . . .	121
5.5.2	Constitutive Material Models . . . . .	125
5.5.3	Sensitivity Analysis . . . . .	129
5.6	Contact Estimation . . . . .	133
5.6.1	BDP approach without continuity [1] . . . . .	134
5.6.2	Continuity-constrained weighted BDP approach . . . . .	136
5.6.3	Choice of $f_i$ for automated data analysis . . . . .	139
5.7	Results . . . . .	140
5.7.1	Parameter reidentification on simulated force curves . . . . .	141
5.7.2	Implementation on elastic map . . . . .	145
5.8	Conclusions . . . . .	149
6	Conclusions and Future Work . . . . .	151
6.1	Conclusions . . . . .	151
6.2	Contributions . . . . .	153
6.3	Future Work . . . . .	154
A	Finite indentation response of Hertz and Dimitriadis contact models . . . . .	156
	Bibliography . . . . .	158



## List of Tables

2.1	AFM probe parameters used for characterization experiments . . . .	16
2.2	AFM probe spring constant for all experiments . . . . .	26
2.3	Summary of AFM indentation experiments. Results shown as mean $\pm$ standard deviation. P-values less than $\alpha(= 0.05)$ are highlighted in bold. . . . .	29
3.1	X-Y travel range of automated AFM scanners, arranged in increasing order of their travel range. . . . .	38
3.2	AFM experimental setting parameters. . . . .	53
3.3	Summary of AFM raster-scanning results on patient specific tissue specimens. Results expressed as mean $\pm$ standard deviation. . . . .	54
4.1	Variation of elastic modulus with change in contact point. . . . .	61
4.2	Summary of AFM probe calibration results using the thermal method. Results expressed as mean $\pm$ standard deviation. . . . .	69
4.3	Conjugate Prior Distributions . . . . .	81
4.4	Hyperparameter Values . . . . .	88
4.5	Model performance on simulated data . . . . .	92
5.1	Summary of implementation of the EIV-Bayesian Changepoint algorithm on two experimental force curves E1 and E2 (Figs. 5.5 and 5.6 respectively acquired on a tissue specimen.) . . . . .	117
5.2	Parameters used to construct the simulated force curves. . . . .	141
5.3	Summary of algorithm performance on force curves S1-S3. Units of $E$ and $E_0$ are in kPa. G.T. indicates ground truth. . . . .	145

## List of Figures

1.1	Stained histopathological images of (a) ductal carcinoma in situ, (b) lobular carcinoma in situ and (c) invasive ductal carcinoma [2]. . . . .	2
1.2	Schematics of (a) Micropipette Aspiration, (b) Magnetic Twisting Cytometry, (c) Optical Tweezer and (d) contact-mode Atomic Force Microscopy. . . . .	6
1.3	Length scales of various biological specimens, together with the appropriate force measuring instruments. . . . .	6
2.1	(a) Stained slide image and (b) adjacent unstained slide image ©2010 IEEE. . . . .	11

2.2	An example of one tissue sample as has been used in different steps of experiment: (a) A low resolution stained image of the tissue microarray. (b) The VM image of an H&E stained tissue core. (c) The same core annotated by a pathologist. (d) The unstained adjacent tissue core (VM image). Please note that tissue distribution in this image is nearly the same as (b) but nearly impossible to distinguish by eye. (e) Image taken from the AFM microscope during AFM experiments ©2013 IEEE. . . . .	13
2.3	AFM experimental setup ©2010 IEEE. . . . .	14
2.4	Hydrated tissue specimen on microscope slide. . . . .	15
2.5	CAD drawing of a typical AFM probe used for tissue characterization experiments. . . . .	16
2.6	Schematic of contact-mode AFM operation. . . . .	17
2.7	(a) Screenshot of MFP3D software panel used to acquire AFM force curves in the deflection-controlled mode. (b) Acquired AFM force curve with a deflection setpoint of 50 nm. The red and blue arrows indicate the direction of the probe's motion. . . . .	20
2.8	Screenshot of cropped MFP3D software panel used to acquire AFM force curves in the indentation-controlled mode. (a) Screenshot of 10 nm deflection-trigger. (b) Acquired force curve with 10 nm deflection trigger. (c) Screenshot of 250 nm indentation trigger. (d) Acquired force curve with 250 nm indentation trigger. The red and blue arrows indicate the direction of the probe's motion. . . . .	22
2.9	Contact estimation algorithm. . . . .	24
2.10	Hertzian contact of an elastic half-space by a sphere of radius $R$ . . . .	25
2.11	Histology images (20X magnification) cropped from four representative regions probed in set 1. (a) and (b) are regions with normal epithelial (A8) and cancerous epithelial (A13) tissue respectively, (c) and (d) are regions with normal stromal (A22) and cancerous stromal (A12) tissue respectively ©2010 IEEE. . . . .	26
2.12	Force-Indentation plots obtained in set 1 at (a) normal epithelial regions (A8), (b) cancer epithelial regions (A13), (c) normal stromal regions (A22) and (d) cancer stromal regions (A12) along with their Hertzian fits and the mean $R^2$ values. Inside each annotated region, roughly 5-8 force curves were taken. Note that despite a target indentation of 250 nm, the tissue indentation varied from 150 - 500 nm. This was primarily on account of incorrect contact estimation in the indentation-controlled mode. . . . .	27
3.1	Flowchart describing manual AFM indentation experiments. (M) = Manual, (A) = Automated. . . . .	35

3.2	Manual registration between unstained and stained images. (a) Stained TMA core image annotated by the pathologist as regions A1, A2 and A3. (b) Brightfield image while performing AFM indentation on a point in annotation A3 after manually registering the stained image (c) Stained TMA core image overlaid with the points probed during AFM experiments on the unstained slide. Observe that annotation A2 has been incorrectly sampled by the AFM. . . . .	36
3.3	AFM Experimental Setup with the MP-285 micromanipulator ©2013 IEEE. . . . .	40
3.4	Extracted features with strong intensity gradients. Observe that prominent features are impurities floating in the liquid environment of the sample. . . . .	41
3.5	Normalized cross correlation algorithm used for tracking at two time instants (a) and (b). The top images correspond to $I_t = I(p_x, p_y, t)$ with the ROI marked with a white box, while the bottom ones are the result images $R$ , where with the estimated ROI position $(\hat{p}_{x,t+1}, \hat{p}_{y,t+1})$ appear as spots of high intensity. . . . .	42
3.6	Calibration of the scaling matrix $S$ using a cover-slip with uniform grids at $100 \mu m$ . . . . .	44
3.7	Tracking protocol for probe-ROI alignment at 10X and 20X. (a) Stained image of tissue core annotated by the pathologist at low resolution (10X). (b) Brightfield image from the AFM-optical microscope. A coarse ROI is selected to match one of the annotated regions in (a). (c) Positioning at 10X. (d) Registration of the coarse ROI at 20X ©2013 IEEE. . . . .	45
3.8	Flowchart describing AFM indentation experiments using the image-guided positioning system (IGPS). (M) = Manual, (A) = Automated.	47
3.9	(a) Representative AFM force curve on a tissue sample mounted on the end-effector. (b) Corresponding force-indentation curve overlaid with the Hertzian fit and (c) Tracking Performance ©2013 IEEE. . .	48
3.10	Elastic maps on normal tissue cores along with their correponding brightfield images. . . . .	50
3.11	Elastic maps on cancer tissue cores along with their correponding brightfield images. . . . .	51
3.12	Uninterpretatble force curve with no prominent non-contact regime. .	52
4.1	Representative AFM force curve on mESC, with candidate contact points shown in red blocks: (a) Whole AFM force curve and (b) transition region from non-contact to contact regime. . . . .	60
4.2	AFM Probe Calibration using the thermal method. (a) An AFM force curve on a tissue-free hard glass surface and (b) thermal spectrum of the probe in PBS solution. The rectangular probe of Table 4.2 (rated compliance of $0.222 \text{ m/N}$ ) was used to generate these results ©2014 IEEE. . . . .	67

4.3	Representative AFM force curve of $d v/s z$ and $d v/s \delta$ . Please note that the $d v/s \delta$ curve is displaced 10nm on the deflection axis for ease of visualization ©2014 IEEE. . . . .	72
4.4	Schematic of the EIV-Bayesian Changepoint algorithm ©2014 IEEE.	82
4.5	Results of the EIV-Bayesian Changepoint algorithm on simulated data with $n = 1000$ datapoints. (a) Simulated AFM force curve with contact occurring at datapoint $k = 650$ and (b) marginal posterior of the contact point index $k$ , along with the posterior mean $[\hat{k}] = 653$ and the 95% confidence intervals $[642, 660]$ . . . . .	89
4.6	Marginal posterior distributions in (a) $\beta_{22}$ (b) $s$ (c) $\sigma_1$ and (d) $\sigma_2$ . . . . .	91
4.7	Image of tissue region where probing was conducted to obtain the results in this section. AFM indentation experiments on breast tissue were conducted in the probing ROI ©2014 IEEE. . . . .	93
4.8	Results of the EIV-Bayesian Changepoint algorithm on a representative AFM force curve on breast tissue with $n = 783$ datapoints. (a) AFM force curve with the posterior mean of the contact point index at $[\hat{k}] = 433$ . (b) Marginal posterior of $k$ . . . . .	95
4.9	(a) Marginal posterior in $s$ and (b) marginal Posterior of $E$ . . . . .	96
4.10	Boxplots of the marginal posterior distributions (a) in $E$ , (b) in $s$ and (c) $k$ . Please note that the $\sigma_{s_d}$ has been assumed to be equal to $\sigma_{s_p}$ . The fourth boxplot ( $\sigma_{s_p} = 0.032$ ) corresponds to the experimental probe compliance variance as obtained in Table 4.2 ©2014 IEEE. . . . .	97
4.11	Boxplots indicating the effect of varying $\mu_{s_p}$ on the marginal posteriors (a) in $E$ and (b) in $s$ ©2014 IEEE. . . . .	100
5.1	Schematic of force-displacement behavior for (a) adhesion-free indentation, (b) indentation with adhesion and (c) representative AFM force curve on breast tissue specimens showing absence of prominent adhesive region. . . . .	106
5.2	Finite-indentation of a thin specimen by a rigid hemispherical indenter.	107
5.3	Effect of heterogeneity in the spatial stiffness distribution. (a) An elasticity map in the cancer core [from Fig. 3.11(b)], (b) corresponding 2-D representation of the R-square of Hertzian fits and (c,d) representative force-indentation plots showing the inadequacy of the Hertz model to describe the entire ROI's constituent behavior. . . . .	110
5.4	Effect of finite deformation on the force response during spherical indentation. (a) Simulated force response on a finite element model of a tissue specimen (cyan) and a Hertzian force response of the same elastic modulus (purple) and (b) corresponding indentation stress ( $\sigma^*$ ) - indentation strain ( $\epsilon^*$ ) using Eqns. (5.3a - c). . . . .	114
5.5	Results of Gibbs Sampling on the posterior distribution using (a) Hertz contact model, (b) Dimitriadis's contact model and (c) Long's contact model on force curve E1. . . . .	118

5.6	Results of Gibbs Sampling on the posterior distribution using (a) Hertz contact model, (b) Dimitriadis's contact model and (c) Long's contact model on force curve E2. . . . .	119
5.7	Evidence of lack of material homogeneity in the direction of indentation. (a) AFM force curves. Please note that the force curves have been displaced to have the same approximate contact point at (0,0).(b) Corresponding force-indentation curves. Note the change in the nature of the force-indentation curves at 200 nm and 300 nm indentation. . . . .	121
5.8	Finite element models: (a) undeformed mesh, (b) deformed mesh. . .	123
5.9	Flowchart of the algorithm used to obtain optimized material properties using the inverse FE approach. . . . .	124
5.10	Performance of the (a) Yeoh and (b) Fung hyperelastic models in describing the force response for force curve shown in Fig. 5.6. . . .	127
5.11	Effect of varying the hyperelastic parameters of the Yeoh (a,b,c) and Fung (d,e) hyperelastic models individually. . . . .	129
5.12	Sensitivity of the Fung model parameters at varying indentations. (a) $\Delta = 100$ nm, (b) $\Delta = 200$ nm, (c) $\Delta = 400$ nm, (d) $\Delta = 600$ nm, (e) $\Delta = 900$ nm and (f) $\Delta = 1400$ nm. Also shown in the third row (g-i) are enlarged figures of (d-f) where the range of $b$ is reduced to 1 – 6. The white dotted line at 400 kPa indicates the elastic modulus of the linearly elastic material. . . . .	130
5.13	Classification curve, showing the variation of $b_{R_{FE,thresh}^2}^{max}(\Delta)$ with $\Delta$ for different values of $R_{FE,thresh}^2$ . Also shown are the curve fits for $b_{R_{FE,thresh}^2}^{max}(\Delta)$ . . . . .	132
5.14	Performance of the three contact estimation methods for simulated force curves S1 - S3 (shown row-wise). The first column shows the sum of squared residuals (SSR) using unconstrained BDP (red) for force curves S1-S3 (a),(d),(g) respectively. The second column shows SSR variations using constrained BDP (blue and green) for S1-S3 (b),(e),(h) respectively. The third column shows the corresponding contact point on the force curves S1-S3 (c),(f),(i) respectively. The contact point estimates using the unconstrained and constrained BDP approaches are also shown at the base of the SSR curve. . . . .	143
5.15	Implementation of the proposed algorithm for automated characterization for simulated force curves S1 - S3 (shown row-wise). Note that the inverse FE correction step was not required for curve S1. . . . .	144

5.16	Implementation of the proposed algorithm for automated characterization on a tissue ROI shown previously in Fig. 5.3. (a) Elastic map using the Dimitriadis model only without any Inverse FE corrections, (b) Corresponding post-contact $R_{Dim}^2$ fit, (c) Elastic map ( $\hat{E}$ ) with inverse-FE correction, (d) Corresponding $R_{net}^2$ fit, where $R_{net}^2 = \max(R_{Dim}^2, R_{FE}^2)$ . White spaces indicate force curves that were not analyzed due to presence of multiple potential contact points such as those in Fig. 5.7. . . . . .	146
5.17	(a) Variation of estimated Fung parameter $\hat{b}$ from the Inverse FE analysis as a function of the estimated indentation (using the contact estimate), (b) zoomed image. Also overlaid in red is $b_{0.992}^{max}(\Delta)$ . . . . .	148
5.18	Representative force-indentation plot with low estimated $b$ value ( $\hat{E}_0, \hat{b}$ ) = (153.21 kPa, 0.005) with $R_{FE}^2 = 0.977$ . The Dimitriadis solution was $\bar{E}_{Dim}$ was 146.14 kPa with $R_{Dim}^2 = 0.975$ . . . . .	148
A.1	(a) Variation of $E_{Hertz}/E$ and $E_{Dim}/E$ for $R = 2.5 \mu\text{m}$ , (b) Corresponding $R^2$ fit quality, (c) Variation of $E_{Hertz}/E$ and $E_{Dim}/E$ for $R = 5.0 \mu\text{m}$ and (d) Corresponding $R^2$ fit quality. . . . .	157

## List of Abbreviations

AFM	Atomic Force Microscopy
BDP	Bi-domain Polynomial
CAD	Computer-Aided Diagnostic
C.I.	Confidence Interval
<i>cov</i>	Covariance
DCIS	Ductal carcinoma <i>in situ</i>
ECM	Extracellular Matrix
EIV	Error-In-Variables
FE	Finite Element
FIEL	Force Integration to Equal Limits
G.T.	Ground Truth
H&E	Hematoxylin and Eosin
IGPS	Image-Guided Positioning System
InvOLS	Inverse Optical Lever Sensitivity
i.i.d	independent and identically distributed
KLT	Kanade-Lucas-Tomasi
LCIS	Lobular carcinoma <i>in situ</i>
LDV	Laser Doppler Vibrometry
MA	Micropipette Aspiration
MCMC	Markov Chain Monte Carlo
mESC	mouse Embryonic Stem Cell
MTC	Magnetic Twisting Cytometry
OT	Optical Tweezers
PBS	Phosphate Buffered Saline
ROI	Region-Of-Interest
SIFT	Scale-Invariant Feature Transform
SSR	Sum of Squared Residuals
TMA	Tissue Microarray
<i>thresh</i>	threshold
<i>var</i>	Variance
VM	Virtual Microscopy
NSF	National Science Foundation
NIH	National Institutes of Health
RAMS	Robotics, Automation, and Medical Systems Laboratory

# Chapter 1

## Introduction

### 1.1 Motivation

It is estimated by the American Cancer Society that 232,340 new cases of invasive breast cancer are expected to be diagnosed among women in the US during 2013, and an estimated 40,030 breast cancer deaths alone are expected in 2013 [3]. Traditional assessments of cancer involve a biopsy procedure, followed by detailed histopathological analysis of the sampled tissue to identify the presence of cancerous lesions.

Histology is the branch of biology that studies the microscopic structure of animal or plant tissues. The most common histological procedure is to embed fixed tissue chunks in paraffin blocks, thinly section them, treat the sectioned tissue slices with various staining techniques, and then study them under an optical microscope. This method has enabled pathologists and clinicians to study human tissue in its normal and diseased forms for hundreds of years and is still playing an indispensable role in clinical pathology and biology research. Four types of tissue are present in human body: epithelial tissue, stromal tissue, nervous tissue and muscles; and they interweave together in distinctive patterns throughout the human body.

Most breast cancers are broadly classified by pathologists into the following categories [2]:



1. *Carcinoma in situ*: These involve neoplastic proliferation that is limited to the ducts [called ductal carcinoma *in situ* (DCIS) - see Fig. 1.1(a)] and lobules [called lobular carcinoma *in situ* (LCIS) - see Fig. 1.1(b)] by the basement membrane.
2. *Invasive/Infiltrative carcinoma*: These involve neoplastic proliferation that have penetrated through the basement membrane into the stromal tissue [see Fig. 1.1(c)].

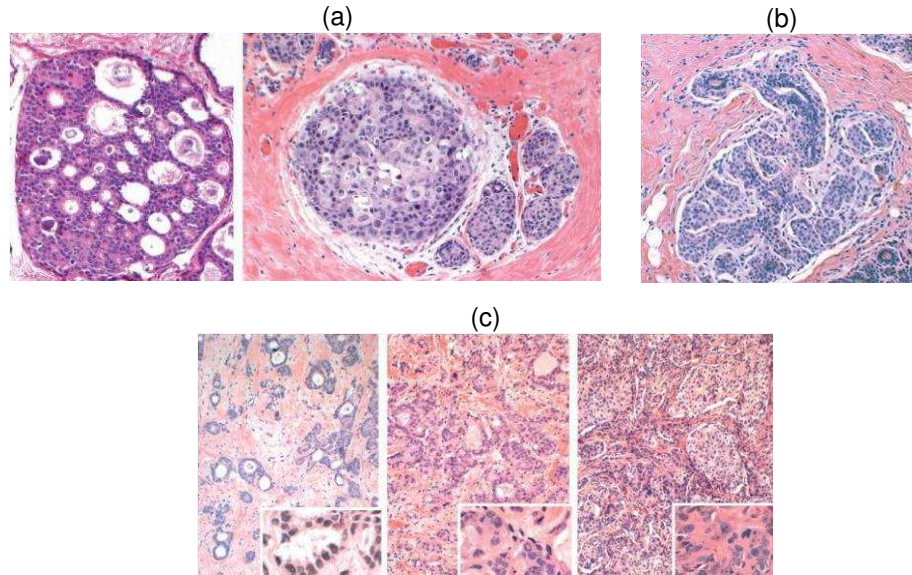


Figure 1.1: Stained histopathological images of (a) ductal carcinoma in situ, (b) lobular carcinoma in situ and (c) invasive ductal carcinoma [2].

While the interpretation of stained images leads to insights into the onset and progression of malignancy in a tissue specimen, this exercise is largely qualitative and based on the subjective impressions of observers. To address this, researchers have proposed a range of computer-aided diagnostic (CAD) methods that assist physicians in rendering more informed clinical decisions. A comprehensive review of

the recent advances in automated interpretation of digital microscopy images and CAD methods with relevance to histopathological tissue is given in [4].

The correlation between pathophysiological processes and the mechanical properties of the tissue they affect has been the subject of substantial research for a number of years. Pathophysiological changes that occur in macroscale tissue have been studied by imaging tools like ultrasound [5], magnetic resonance imaging [6] and computed tomography [7], and there is reason to believe that these changes may manifest at the single cellular level [8]. Li *et al.* [9] reported increased deformability in cancerous breast epithelial cells compared to normal breast epithelial cells, while similar increase in deformability was reported in cancerous bladder cells [10]. It has been hypothesized that the cellular cytoskeleton plays a dominant role in the onset and progression of cancer. Actin reorganization was speculated to be the cause of alteration in mechanical properties in bladder cells [10], breast epithelial cells [9], mouse fibroblast cells [11] and keratinocytes [12]. Changes in deformability in the extracellular matrix (ECM), that provides structural support to the cells, was reported to activate malignancy in breast epithelial cells [13], while the role of cell-ECM binding in cancer has been investigated in [14].

While the structural changes in cellular architecture and the surrounding ECM induced by cancer has been widely documented at the cellular scale [8], the morphological changes inside a developing tumor lesion is not clearly understood yet. Indeed, the difference between cellular and tissue-level manifestation of cancer can be noted by observing the apparent dichotomous impact of cancer across length scales: pathologists use breast palpation to locate the presence of stiff nodules,

which correspond to hardening of the neighboring tumor stromal tissue [15], while cell biophysicists widely report increased deformability in malignant cells compared to healthy ones, as mentioned earlier [8].

There are several reasons for investigating the mechanical changes that accompany onset and progression of cancer at the tissue level as opposed to the cellular level. Studying the tumor at the tissue level provides direct insight into the underlying architectural changes that occur within a developing lesion and the surrounding tissues, and the degree of malignancy can be quantified in the tissue's native environment. In contrast, the relevance of single-cell study is somewhat questionable since it is not representative of a three-dimensional tissue environment.

Another distinct advantage of studying tumor-level breast cancer is the improved throughput associated with histological tissue preparation. Using techniques like tissue microarray (TMA) [16] technology, where representative samples from numerous biopsy procedures can be assembled onto a single microscope slide, it is possible to characterize many sub-classes of cancer in a reasonably short period of time. It is therefore enticing to imagine a battery of mechanical signatures of various subclasses of cancer complementing the digitized stained-image information from an imaging system to greatly enhance the capability of current computer-aided diagnostic methods in making informed clinical decisions.

Advances in cancer biomechanics research has been supplemented by a surge in the development of mechanical property measurement techniques at the micro/nano scale [17]. Some of the most common methods used to quantify mechanical properties of biomaterials are given as follows (see Fig. 1.2 [17]):

1. *Micropipette Aspiration (MA)*: In this technique, a biological cell is drawn into a pipette using a known suction pressure. The aspiration length quantifies the deformability of various types of cells.
2. *Magnetic Twisting Cytometry (MTC)*: This method involves attaching magnetic beads to functionalized surfaces of cells. Application of a known magnetic field deforms the surface of the cell, which characterizes the cellular elastic and viscous properties.
3. *Optical Tweezers (OT)*: In this method, a highly focused laser beam is aimed at a dielectric bead, usually attached to the biological specimen. The high intensity of the laser creates a “trap” which holds the bead and the attached specimen at the focusing point. In many cases, two beads are attached to two diametrically opposite surfaces of a cell.
4. *Atomic Force Microscopy (AFM)*: The AFM system consists of a micro-cantilever probe that is piezoelectrically controlled to deform tissue samples by a fixed amount. Based on the AFM probe and tissue-sample interaction forces, the cantilever deflects, which is then optically sensed. This deflection and the corresponding change in light intensity is related to the stiffness of the sample probed by the AFM.

While the MA, MTC and OT based mechanical assays all possess the ability to quantify mechanical properties of micro/nano scale biomaterials, AFM surpasses these techniques in its versatility in quantifying mechanical properties of biomateri-

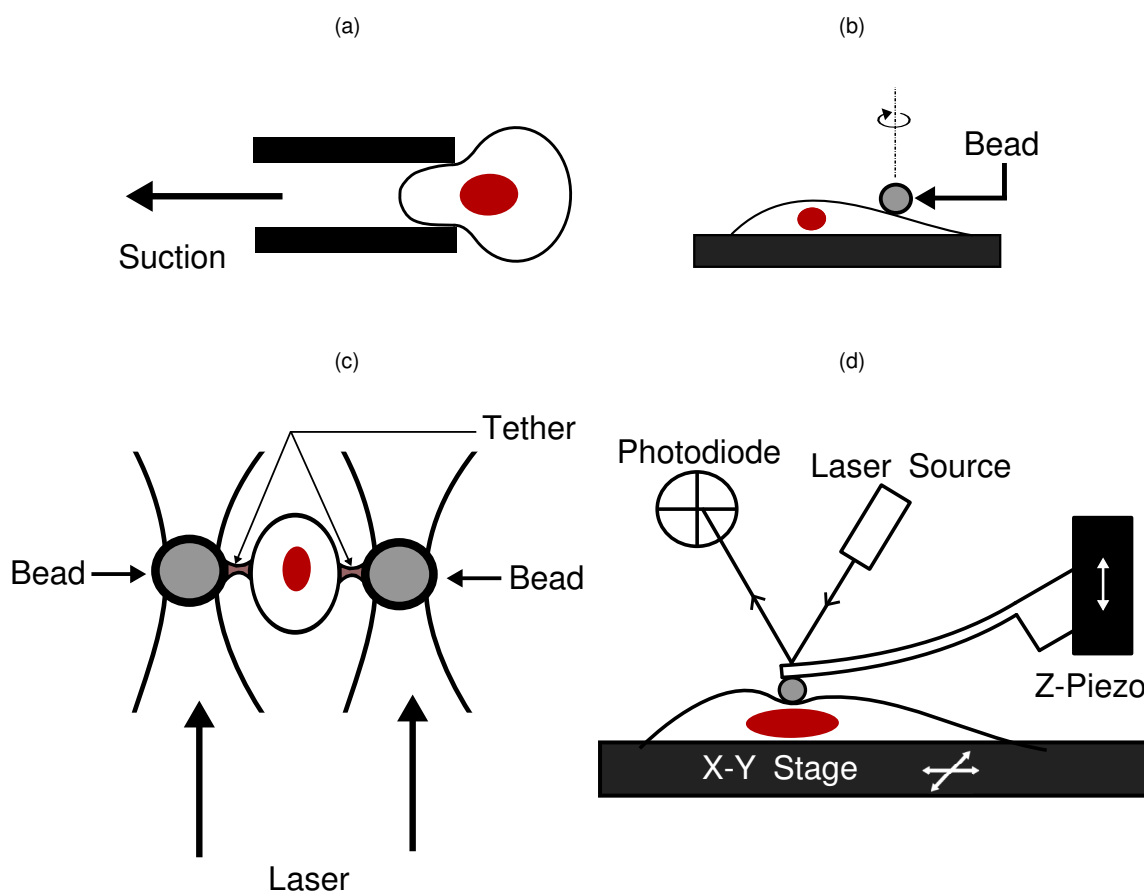


Figure 1.2: Schematics of (a) Micropipette Aspiration, (b) Magnetic Twisting Cytometry, (c) Optical Tweezer and (d) contact-mode Atomic Force Microscopy.

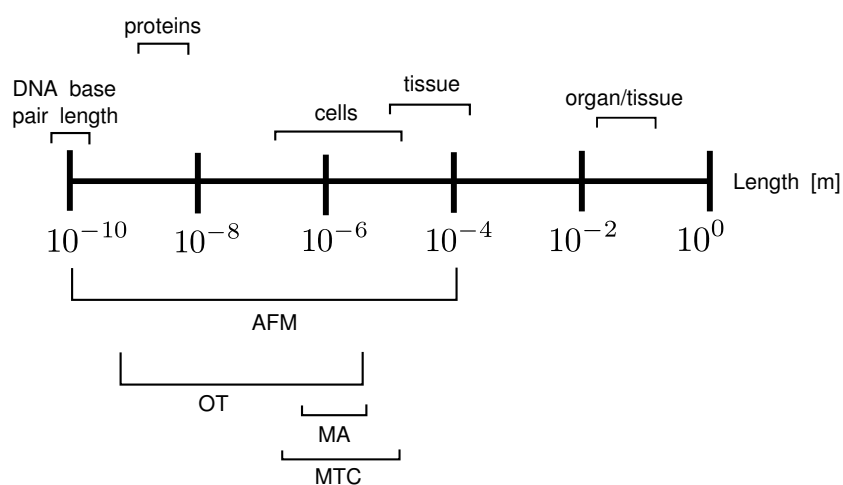


Figure 1.3: Length scales of various biological specimens, together with the appropriate force measuring instruments.

als across various length scales (see Fig 1.3). It also allows minimal sample preparation and therefore samples can be studied in their physiological environment. Apart from its ability to measure nanoscale to picoscale forces, it is also widely used as an imaging tool [18].

*With this background in breast cancer and the mechanical assays that hold the potential to quantify it, it is hypothesized that using the AFM in contact mode, differentiable measures of local stiffness in histopathological breast tissue could reveal insights into the nature and progression of breast cancer that could supplement traditional staining based histological assessments for diagnostic purposes.*

## 1.2 Proposed Solution

The research objectives that have been addressed in this work are stated as follows:

1. *Tissue preparation protocol and preliminary feasibility study:* In order to ensure that AFM sampling in the tissue is restricted to a region of biological interest, it is necessary to have a predefined map of the tissue specimen which can be used as a reference to navigate through the specimen under AFM indentation. Virtual-microscopy (VM) enabled TMA technology for this purpose. The results of preliminary characterization studies show that cancerous epithelial tissue exhibits increased deformability compared to normal epithelial tissue.
2. *Experimental improvements in the AFM sampling procedure:* Human breast

tissue being highly heterogeneous wherein functional breast epithelial cells are surrounded by stromal tissue in a complex intertwined manner, sampling a particular cell type is highly labor-intensive and inefficient. To enhance the positioning throughput prior to AFM indentation, a long-range image-guided positioning system (IGPS) has been developed that improves efficiency in AFM tissue characterization experiments significantly, and the developed setup serves as a useful supplement to commercial AFM X-Y stages with limited scanning range.

3. *Error quantification in tissue stiffness estimates from indentation data:* A critical pre-requisite to effective tissue characterization is accurate data analysis of raw AFM data. Variability in two key experimental parameters give rise to inaccurate estimation of the tissue mechanical properties: (1) the *contact-point* in an AFM force curve, which relates to the probe's vertical position when it first makes contact with the tissue and (b) the probe's *spring constant*, which converts the probe deflection into the contact force. To this end, an error-in-variables (EIV) based Bayesian Changepoint algorithm has been developed to investigate the impact of these uncertainties in the mechanical characterization process.
4. *Constitutive modeling of breast tissue:* The direct implication of spatial heterogeneity in breast tissue specimens is that tissue response might not be adequately captured through linearized analytical contact models such as the Hertz contact model. Violations to Hertzian contact theory has been investi-

gated by using numerical procedures and an exponential type phenomenological hyperelastic constitutive model has been proposed to estimate nonlinear tissue properties from AFM data.

### 1.3 Organization

Single-cell mechanical characterization using AFM has been well-researched in the past[19] and this dissertation commences by following a cell-based AFM characterization protocol as a starting point. In chapter 1, the background and motivation for this study is discussed. In chapter 2, the operation of the AFM, the tissue preparation and AFM experimental protocol are introduced and the results of preliminary AFM indentation experiments on breast tissue specimens are discussed. Following this, the development of a semi-automated positioning system is reported in chapter 3, which improves efficiency in the AFM characterization experiments on tissue compared to preliminary tissue characterization. In chapter 4, details of a probabilistic mathematical model using EIV-Bayesian Changepoint scheme is elaborated, which is used to estimate tissue mechanical properties from AFM data after taking into consideration the innate errors in the AFM system. In chapter 5, constitutive material modeling of the tissue specimens under AFM indentation is discussed. Finally, in chapter 6, contributions of this dissertation and the future goals of this project are discussed.



## Chapter 2

### Pilot Mechanical Characterization Studies on Breast Tissue

#### Pathology samples using Atomic Force Microscopy

#### 2.1 Overview

This chapter discusses the results of pilot studies of AFM indentation on human breast tissue. Epithelial and stromal tissue regions were selected from normal and cancerous tissue specimens and AFM indentation experiments were carried out on these regions. In section 2.2, the materials and methods used to prepare the tissue microarray map of prescribed locations, the AFM experimental setup with its operating principle and the AFM data analysis are discussed. In section 2.3, the tissue elasticity results are presented. This chapter is concluded in section 2.4 with a discussion of the merits and demerits of the experimental protocol and suggested improvements.

#### 2.2 Material and Methods

##### 2.2.1 Tissue Microarray (TMA) preparation and Annotation

Tissue Microarray (TMA) technology is a relatively new technique for harvesting tiny cylinders of tissue and arranging them on a recipient paraffin block in a matrix-like format [16]. TMA has been widely used as a high throughput analytical

tool for conducting large scale molecular studies on tissue specimens. Tissue cores of 0.6 mm diameter were extracted from paraffin-embedded normal and breast cancer tissue blocks and assembled into 4 quadrupled tissue microarray blocks using Auto Tissue Arrayer (Beecher ATA-27). Two consecutive 4  $\mu\text{m}$  slices of each TMA were cut and fixed onto glass slides (see Fig. 2.1).

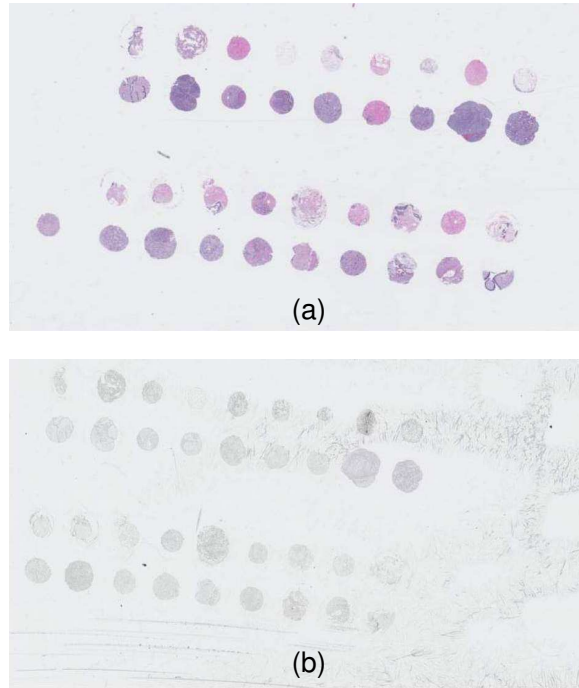


Figure 2.1: (a) Stained slide image and (b) adjacent unstained slide image ©2010 IEEE.

One of each set of consecutive slides was stained with hematoxylin and eosin (H&E) and cover-slipped. Following the extraction on tissue cores, Virtual Microscopy (VM) technology was used to generate digital scans of the tissue segments. VM automatically scans a specimen in a fixed high resolution and allows users to navigate the digital specimen as if they were viewing the specimen using a traditional microscope [see Fig 2.2(a) and 2.2(b)]. Both the stained and unstained

tissue slides were digitized using Trestle/Zeiss MedMicro scanning system at 40x equivalent resolution into a tiled TIFF format and uploaded onto the web server at <http://virtualscope.umdj.edu> for subsequent viewing and annotation.

The H&E slides were examined by a certified pathologist to confirm histological validity of specimen and one pair of consecutive slides was selected based on the fact that they contained adequate amount of breast parenchyma for the experiments. The certified pathologist then annotated valid normal epithelial regions; normal stromal regions; cancer epithelial regions and cancer stromal regions using the online annotation tool [Fig 2.2(c)], while the labels were concealed to the personnel performing the AFM tests. The AFM operator was only provided information on the regions to be indented.

Using TMA technology in the experimental design served three primary purposes. First and foremost, the configuration of TMA specimen facilitated navigation about the specimens and dictated that each sampling that was taken using the AFM probe could be applied unambiguously to specific tissue cores by registering the stained and unstained core images. Second, as each TMA slide can contain dozens to hundreds of tissue cores, each potentially originating from a different patient, TMA technology provides abundant specimen sources and experiment design possibilities. Third, it has been proven that TMA technology preserves the microscopic tissue architecture in each tissue disc for visual assessment as well as for various qualitative and quantitative assessments [16, 20, 21, 22, 23].

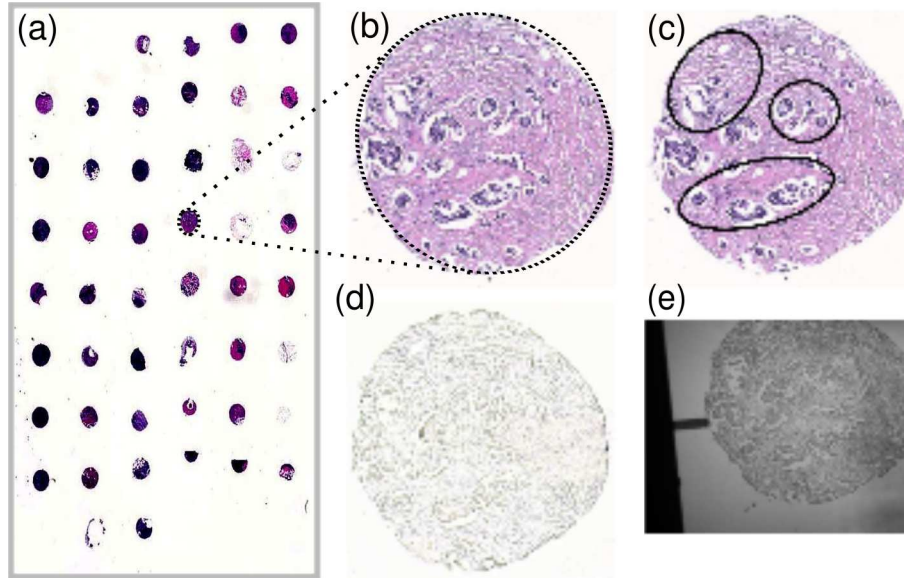


Figure 2.2: An example of one tissue sample as has been used in different steps of experiment: (a) A low resolution stained image of the tissue microarray. (b) The VM image of an H&E stained tissue core. (c) The same core annotated by a pathologist. (d) The unstained adjacent tissue core (VM image). Please note that tissue distribution in this image is nearly the same as (b) but nearly impossible to distinguish by eye. (e) Image taken from the AFM microscope during AFM experiments ©2013 IEEE.

### 2.2.2 AFM experimental setup

Prior to AFM experiment, the unstained adjacent slide from the annotated one was de-paraffinized with xylenes and hydrated with graded alcohols, then kept in Phosphate buffered saline (PBS).

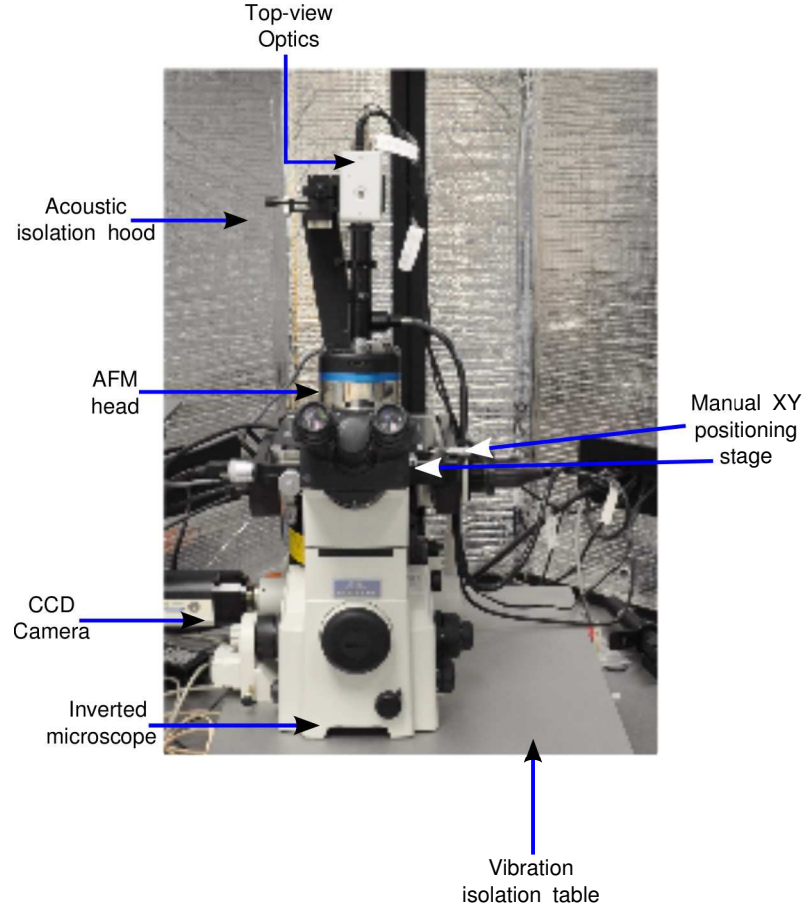


Figure 2.3: AFM experimental setup ©2010 IEEE.

The Atomic Force Microscope (AFM) system consists of the AFM head and controller (MFP-3D-BIOTM, Asylum Research) and an inverted microscope (Model: TE2000U, Nikon, Inc) coupled to it such that the AFM head rests on the microscope (Fig. 2.3). The whole setup is placed on a vibration isolation table (manufactured by Herzan) and is isolated from external noise using an acoustic hood. The X-Y

range of the automated scanning stage is  $90\text{ }\mu\text{m}$  and the Z-range is  $40\text{ }\mu\text{m}$ .

The region of the slide containing the tissue cores was encircled by a hydrophobic barrier (Fig. 2.4) using a Pap-Pen (Invitrogen Corporation, Carlsbad, CA), and PBS solution was intermittently added in the encircled region to ensure that the tissue cores did not dry up. The barrier prevents the PBS solution from spilling over to the X-Y scanning stage while performing tissue-AFM probe alignment.

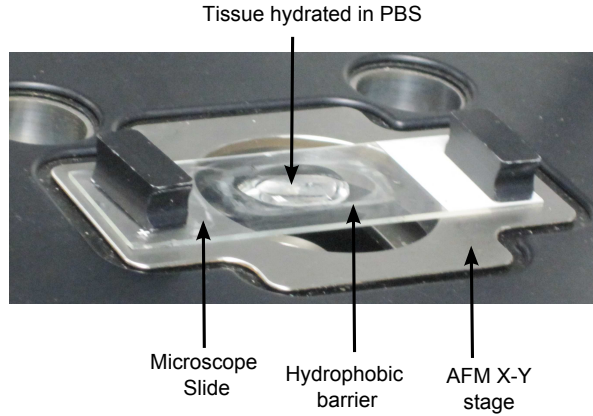


Figure 2.4: Hydrated tissue specimen on microscope slide.

After locating each array core on the slide, the annotated regions of interest within each core were identified by closely following the annotated map [Fig. 2.2(c)] and  $\sim 5$ -8 indentations were carried out within the annotated region.

AFM cantilevers with pyramidal tips have been shown to produce stress concentration on the sample and may also potentially damage the tissue [24]. Hence, AFM cantilevers with spherical glass tips (Novascan Technologies, spherical bead of diameter  $5\text{ }\mu\text{m}$ ) were used for the AFM indentation experiments (see Fig. 2.5). Typical probe dimensions are tabulated in Table. 2.1.

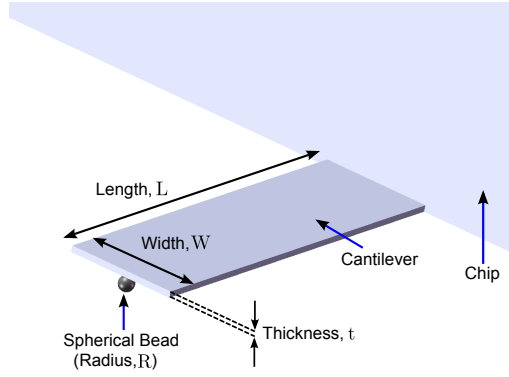


Figure 2.5: CAD drawing of a typical AFM probe used for tissue characterization experiments.

Table 2.1: AFM probe parameters used for characterization experiments

Typical Parameters	
Length, $L$	$130 \mu\text{m}$
Width, $W$	$35 \mu\text{m}$
Thickness, $t$	$2 \mu\text{m}$
Bead Radius, $R$	$5 \mu\text{m}$
Spring Constant	$4.50 \text{ N/m}$

### 2.2.3 Contact-mode operation of AFM

Fig. 2.6 shows a schematic of the contact-mode operation of the AFM. The AFM probe is lowered vertically towards the specimen using the piezoelectric scanner (also called the z-piezo), while its deflection is measured by monitoring the deviation in laser signal reflected from the backside of the AFM probe and sensed through a photodiode. When the probe is far away from the specimen, the vertical  $z$  position and the deflection,  $d$ , are recorded as  $z_1$  and  $d_1$  respectively [Fig. 2.6(a)]. As the probe is lowered, it makes contact with the specimen at  $(z_k, d_k)$  [Fig. 2.6(b)]. The probe is further lowered till its maximum vertical displacement at  $(z_n, d_n)$

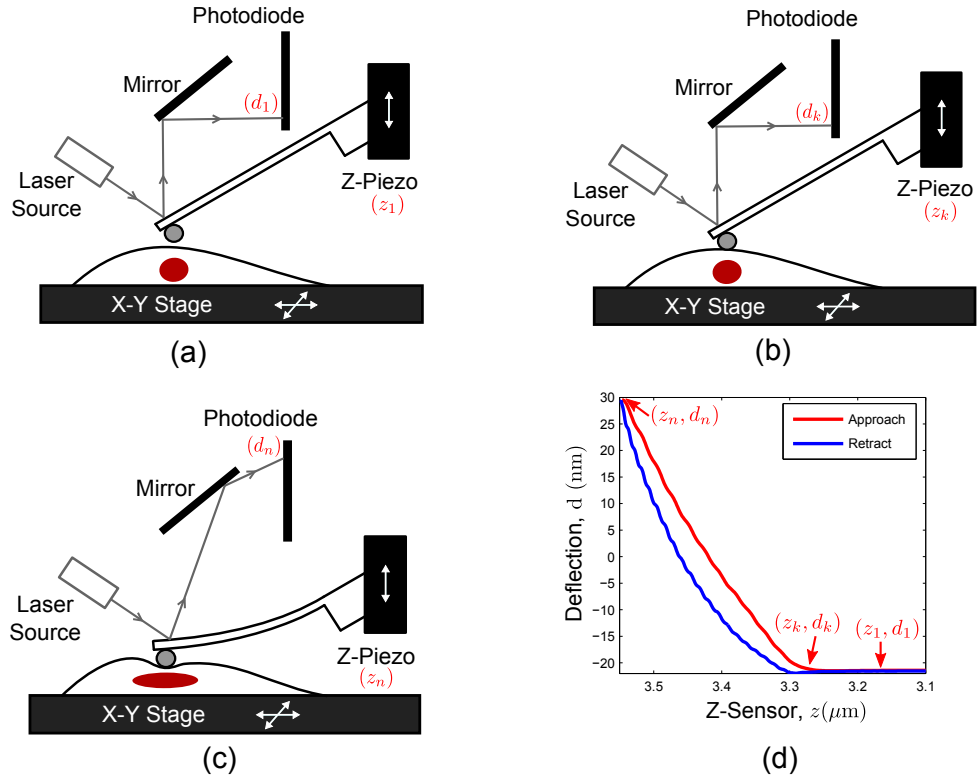


Figure 2.6: Schematic of contact-mode AFM operation.



[Fig. 2.6(c)]. After this, the probe is retracted in the opposite vertical direction. A 2D representation of the deflection,  $d$ , as a function of the vertical displacement,  $z$ , constitutes an AFM **force curve** [Fig. 2.6(d)]. When the probe is lowered towards the specimen the force curve is termed as the **approach force curve**. During the probe retraction phase, the force curve is termed as **retract force curve**.

Given  $n$  data points in a force curve<sup>1</sup>, the net indentation in the sample is given by the following equation [24]:

$$\Delta = (z_n - z_k) - (d_n - d_k) \quad (2.1)$$

The AFM measures the probe deflection, which needs to be related to force. For low deflection regimes, it is possible to treat the cantilever probe as a linear spring of spring constant  $k_c$ . The value of  $k_c$  is obtained by calibrating the probe's spring constant prior to an AFM experiment. The "thermal method" [25] was used for calibrating the probe's spring constant using Asylum Research software (IGOR Pro, Wavemetrics, Inc.)<sup>2</sup>. The force,  $F$ , then can be related to the deflection by :

$$F = k_c(d_n - d_k) \quad (2.2)$$

Now that force  $F$  and indentation  $\Delta$  can be obtained from the AFM force curve, all that remains is to curve-fit the force and indentation to a contact model

---

<sup>1</sup>Henceforth, by the term "force curve", the approach part of the AFM force curve is implied. In this dissertation, data analysis was not carried out on the retract portion of the force curve, which is typically used to quantify viscoelastic properties.

<sup>2</sup>Details of the probe calibration procedure are given in chapter 4.

to estimate the material properties of the specimen. This is discussed in section 2.2.5.

## 2.2.4 Operating modes for AFM indentation

There are two modes in which the AFM force curves are acquired: *deflection-controlled* mode and the *indentation-controlled* mode. These determine the amount of vertical travel of the AFM probe towards (and into) the specimen.

### 2.2.4.1 Deflection-controlled AFM force curves

The deflection-controlled mode is considered to be the “gold standard” for acquiring AFM force curves, and is the most commonly used mode used for AFM indentation experiments. In this mode, a constant deflection setpoint  $[(d_n - d_1)$ , see Fig. 2.7(a)] is set and the probe is lowered towards the specimen till the probe deflection ( $d_n$ ) with respect to the non-contact deflection ( $d_1$ ) reaches the deflection setpoint [Fig. 2.7(b)]. At this point, the probe is retracted from the specimen. Fig. 2.7 shows the acquisition of an AFM force curve in the deflection-controlled mode with 50 nm deflection setpoint. The deflection can be directly related to the contact force by multiplying with the probe spring constant, consequently, the deflection-controlled mode is also termed as *force-controlled* mode. Henceforth, this mode is referred to as the force-controlled mode.

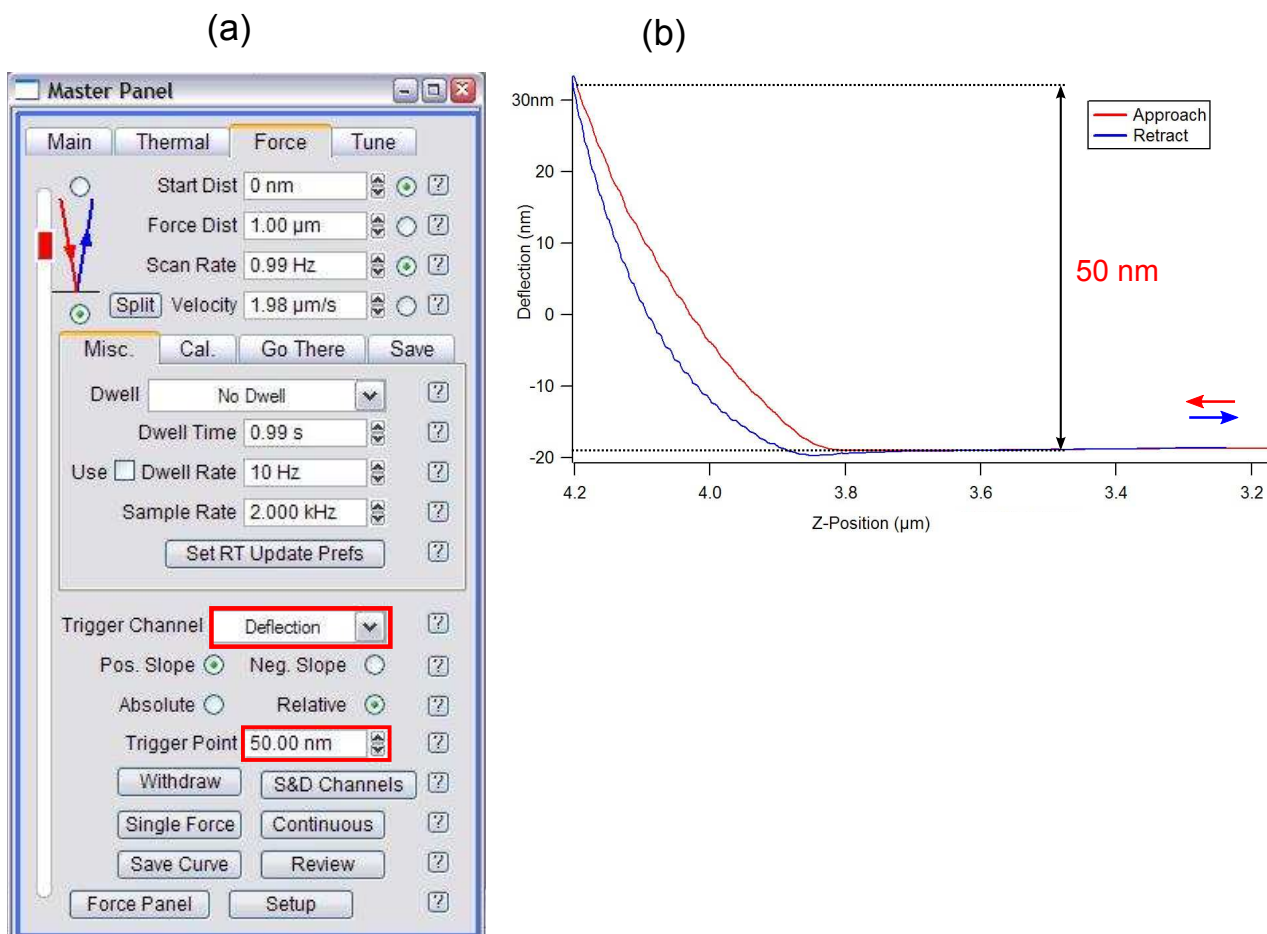


Figure 2.7: (a) Screenshot of MFP3D software panel used to acquire AFM force curves in the deflection-controlled mode. (b) Acquired AFM force curve with a deflection setpoint of 50 nm. The red and blue arrows indicate the direction of the probe's motion.

#### 2.2.4.2 Indentation-controlled AFM force curves

For force curves acquired using the same deflection setpoint through the force-controlled mode, specimen elasticity variations manifest as variability in indentation (soft materials show larger indentations than stiffer materials for the same deflection setpoint). Therefore, the force-controlled mode is not useful when a constant sample indentation is desired.

The *indentation-controlled* mode is used to address this need. In order to achieve a specific indentation in a force curve, the contact location  $(z_k, d_k)$  [please see Fig. 2.6(d)] must be known. However, there is no way for the AFM to identify the contact point in a given force curve: it can only measure the deflection,  $d$ , and the vertical z-position,  $z$ .

To achieve a target indentation in the indentation-controlled mode, first an AFM force curve is acquired for a very low deflection setpoint ( $\sim 10$  nm) in the force-controlled mode [Fig. 2.8(a,b)]. The vertical position abscissa  $\bar{z}_n$  at which this deflection setpoint is reached is recorded [Fig. 2.8(b-inset)]. Then, a target indentation setpoint is set [Fig. 2.8(c)] and a second force curve is acquired. In this second force curve, the contact location  $z_k$  is set to  $\bar{z}_n$  from the first force curve. Based on this estimated contact point, the probe is lowered by the z-piezo till the indentation  $[(z_n - z_k) - (d_n - d_k)]$  reaches the target indentation depth [Fig. 2.8(d)]. In Fig. 2.8, a deflection setpoint of 10 nm and an indentation setpoint of 250 nm was used for the first and second force curves respectively.

While the indentation-mode appears attractive, particularly in the context of

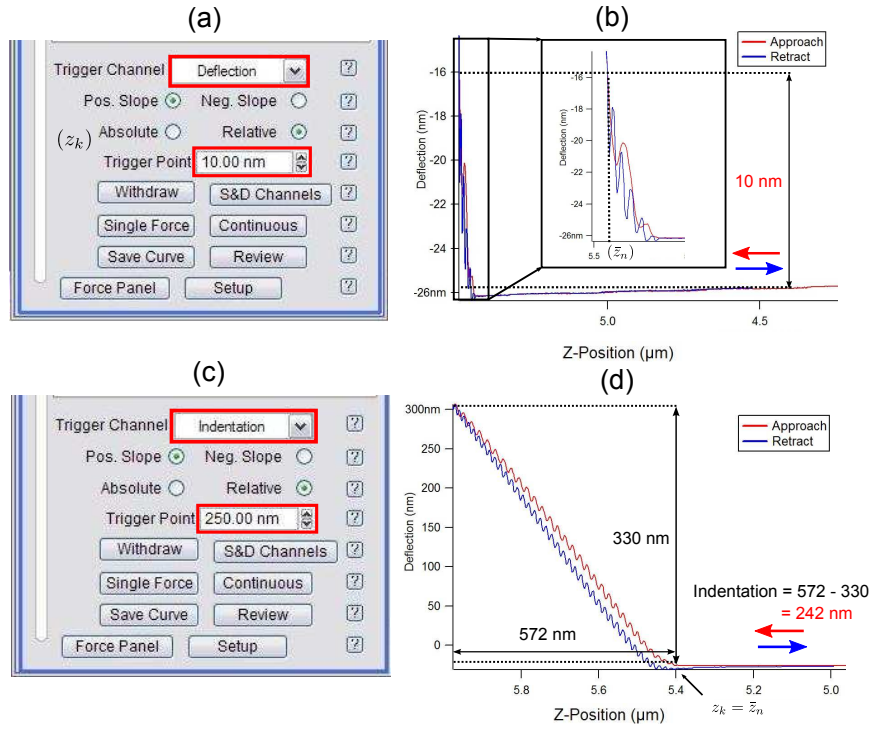


Figure 2.8: Screenshot of cropped MFP3D software panel used to acquire AFM force curves in the indentation-controlled mode. (a) Screenshot of 10 nm deflection-trigger. (b) Acquired force curve with 10 nm deflection trigger. (c) Screenshot of 250 nm indentation trigger. (d) Acquired force curve with 250 nm indentation trigger. The red and blue arrows indicate the direction of the probe's motion.

analyzing force curves for mechanical characterization [shallow indentations ( $< 50$  nm) for a  $4\text{ }\mu\text{m}$  thick tissue sample) do not provide enough information about the tissue response, while too large indentations<sup>3</sup> necessitate complex contact models that account for nonlinearity in the tissue response], there are significant shortcomings of this approach. Firstly, the tissue specimen is indented twice in this mode, as opposed to the force-controlled mode where only one force curve is acquired at a given location on the tissue surface. Not only does this double the time taken to conduct characterization experiments, but this mode also subjects the tissue to preconditioning effects due to the effect of the first force curve. Secondly, prior knowledge of the tissue specimen’s stiffness is necessary while acquiring the first force curve, because even a small setpoint may result in large tissue indentation if the tissue stiffness in the probed region is considerably less than the probe’s spring constant. If this is the case, the deflection setpoint for the first force curve has to be lowered and the process repeated.

### 2.2.5 Data Analysis

The mechanical properties are obtained by processing the force-curves offline. Two steps are needed for this: determining the contact point  $(z_k, d_k)$ , and curve fitting the post-contact force indentation data to a contact model.

To determine the contact point  $(z_k, d_k)$ , a derivative-based algorithm (Fig. 2.9) proposed in [24], was used. In this method, the slope between two deflection dat-

---

<sup>3</sup>The impact of large indentations on the estimated elastic modulus has been studied in detail in Chapter 5.

apoints  $d_i$  and  $d_{i+p}$  is compared to a predefined threshold value  $s_{setpt}$ . If the slope exceeds  $s_{setpt}$ , then the contact point is estimated to be  $(z_{\hat{k}}, d_{\hat{k}}) = (z_{i+p/2}, d_{i+p/2})$ . Based on the experimental force curves,  $p = 10$  and  $s_{setpt} = 5 - 20$  nm is used.

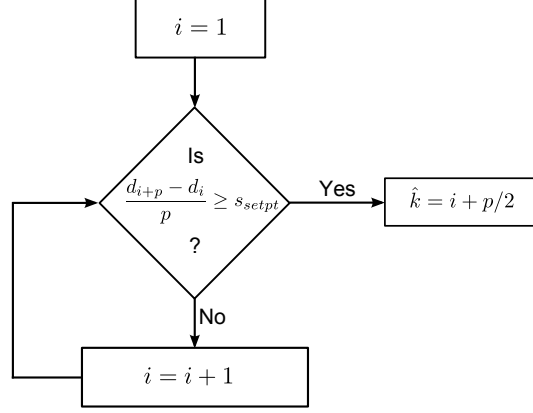


Figure 2.9: Contact estimation algorithm.

The Hertz contact model [26] was used for extracting the elastic modulus from the acquired force curves. The contact force,  $F$ , is related to the indentation,  $\Delta$ , of an elastic half-space by:

$$F = \frac{4\sqrt{R}}{3} \left[ \frac{1 - \nu^2}{E_1} + \frac{1 - \nu^2}{E_2} \right]^{-1} \Delta^{1.5} \quad (2.3)$$

where  $E_1$  and  $E_2$  are the elastic moduli of the indenter and the half-space and  $\nu_1$  and  $\nu_2$  are the Poisson's ratio of the indenter and the half-space respectively. The contact radius,  $a$ , is given by the following relation:

$$a = \sqrt{R\Delta} \quad (2.4)$$

Hertzian theory involves the following assumptions:

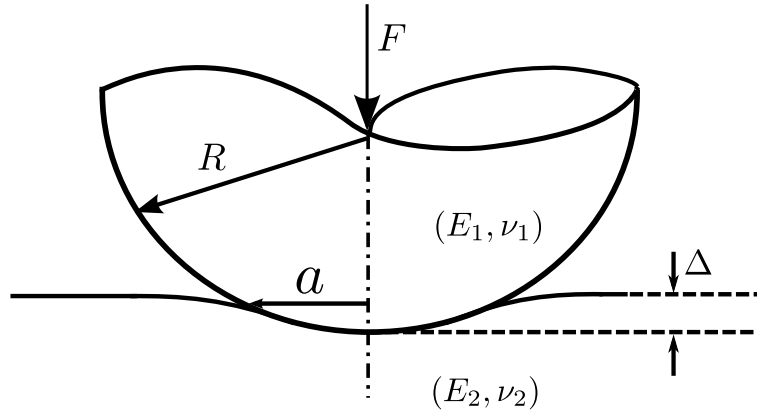


Figure 2.10: Hertzian contact of an elastic half-space by a sphere of radius  $R$ .

1. The sphere and the half-space are homogeneous and isotropic.
2. The indentations and strains in the half-space are infinitesimal and therefore linearized continuum theory is applicable.
3. The contact between the sphere and the half-space are considered frictionless.
4. There is no adhesion between the sphere and the indenter.
5. Both the sphere and the half-space are linearly elastic materials.

Assuming the tissue to be incompressible,  $\nu_2$  can be set to 0.5. For the case of indentation of the tissue with an probe (with an attached spherical bead),  $E_2 \gg E_1$ , hence Eqn. (2.3) can be re-written as:

$$F = \frac{4E_2\sqrt{R}}{3(1-\nu_2)^2} \Delta^{1.5} \quad (2.5)$$



## 2.3 Results and Discussions

The AFM experiments conducted were primarily aimed at examining the difference in the mechanical properties at (a) epithelial and stromal regions of normal breast tissue and (b) epithelial and stromal regions of cancerous breast tissue.

Three separate sets of AFM indentation studies were performed to investigate the variations in elasticity in normal and cancerous samples. The calibrated spring constants in each set are tabulated in Table 2.2. The experiments were conducted in the indentation-controlled mode by setting an indentation setpoint of 250 nm.

Table 2.2: AFM probe spring constant for all experiments

Set	Calibrated Spring Constant	Theoretical Spring Constant
1	2.50 N/m	4.50 N/m
2	3.89 N/m	4.50 N/m
3	3.25 N/m	4.50 N/m

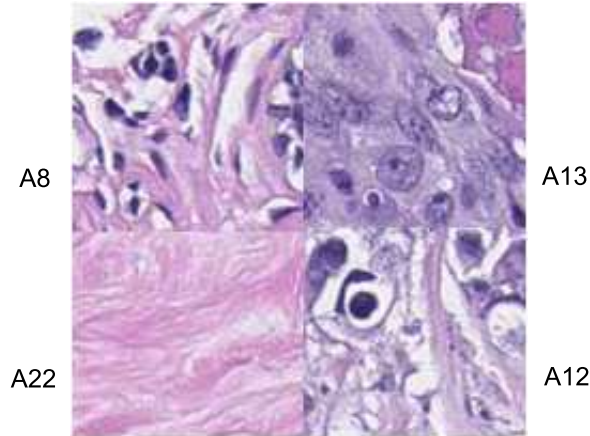


Figure 2.11: Histology images (20X magnification) cropped from four representative regions probed in set 1. (a) and (b) are regions with normal epithelial (A8) and cancerous epithelial (A13) tissue respectively, (c) and (d) are regions with normal stromal (A22) and cancerous stromal (A12) tissue respectively ©2010 IEEE.

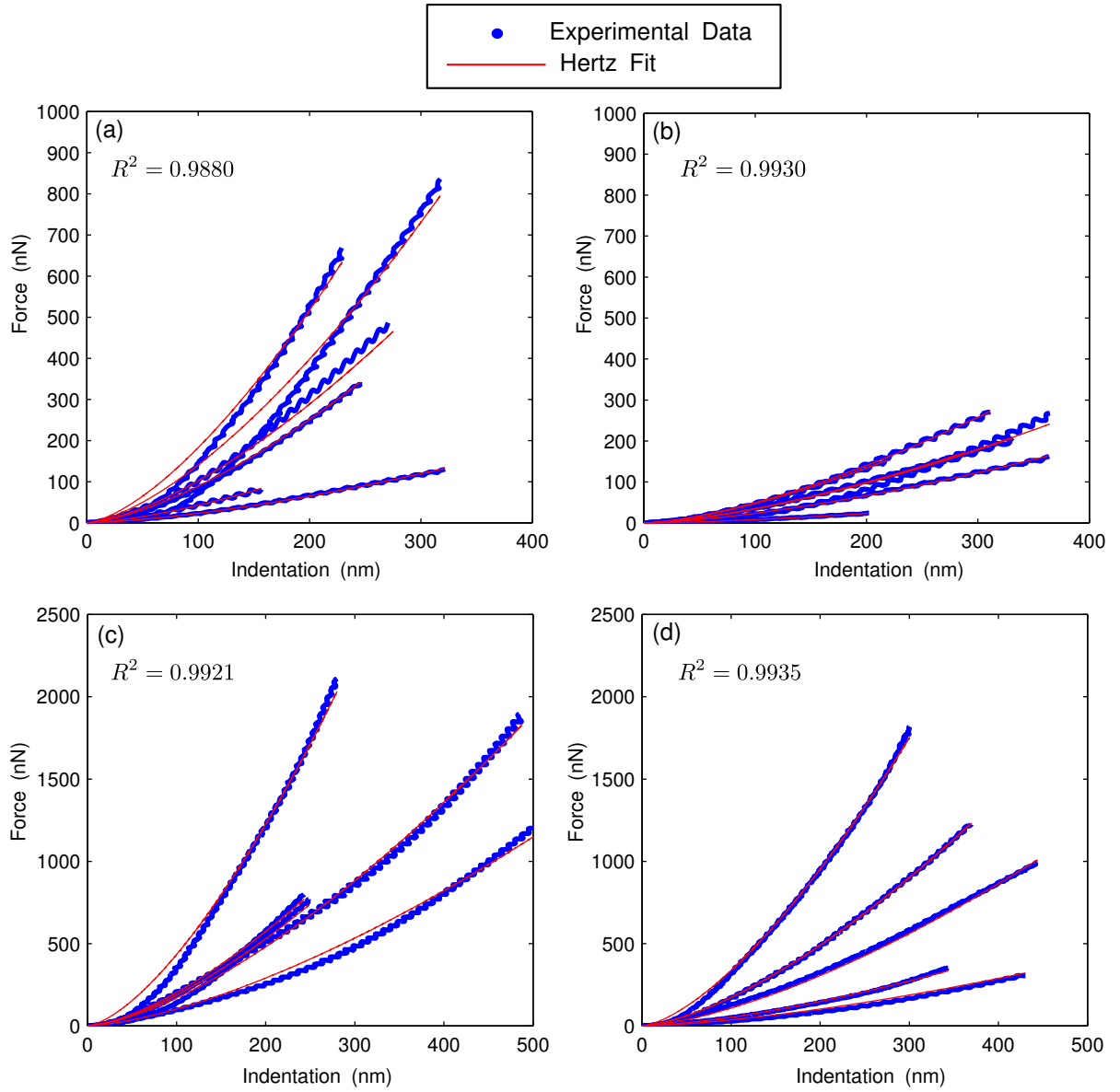


Figure 2.12: Force-Indentation plots obtained in set 1 at (a) normal epithelial regions (A8), (b) cancer epithelial regions (A13), (c) normal stromal regions (A22) and (d) cancer stromal regions (A12) along with their Hertzian fits and the mean  $R^2$  values. Inside each annotated region, roughly 5-8 force curves were taken. Note that despite a target indentation of 250 nm, the tissue indentation varied from 150 - 500 nm. This was primarily on account of incorrect contact estimation in the indentation-controlled mode.

The force-indentation curves and the associated Hertz fits obtained by probing 5-8 locations on each of the annotations (A8, A13, A22 and A12 as shown in Fig. 2.11) in set 1 are shown in Fig. 2.12. From the force plots, it is evident that cancerous epithelial regions exhibit lower stiffness compared to normal epithelial regions.

A summary of the results of all three sets of experiments is tabulated in Table 2.3. In set 1, 23 and 25 regions were probed in normal and cancerous epithelial tissue respectively, and 12 and 18 regions were probed in normal and cancerous stromal tissue respectively. The mean elastic modulus of the epithelial regions was computed to be  $981.80 \pm 576.72$  kPa and  $522.79 \pm 274.66$  kPa for normal and cancerous tissue respectively. The mean elastic modulus of the stromal regions was computed to be  $2342.65 \pm 968.38$  kPa and  $1335.58 \pm 1087.87$  kPa for normal and cancerous tissue respectively. Using an unpaired t-test, the normal epithelial regions were found to be significantly stiffer than cancerous epithelial regions ( $p = 0.006$ ).

In set 1, the overall stiffness of 35 probed regions in normal tissue was significantly stiffer than the overall stiffness of 53 probed regions in cancer tissue ( $p=0.009$ ). Also, the overall stiffness of 30 probed regions in stromal tissue was significantly stiffer than the overall stiffness of 48 probed regions in epithelial tissue ( $p=0.0001$ ).

In set 2, however, only 3 cancerous stromal regions could be probed. Likewise, in set 3, only 7 normal epithelial regions could be probed. Undersampling in the cancerous stromal regions and normal epithelial regions in sets 2 and 3 respectively was primarily due to (1) fewer annotated regions to sample from and (2) region

Table 2.3: Summary of AFM indentation experiments. Results shown as mean  $\pm$  standard deviation. P-values less than  $\alpha(= 0.05)$  are highlighted in bold.

		Epithelial		Stromal	
		Normal	Cancerous	Normal	Cancerous
Set 1	Sampled Points	23	25	12	18
	Elastic Modulus (kPa)	$981.80 \pm 576.72$	$522.79 \pm 274.66$	$2342.65 \pm 968.38$	$1335.58 \pm 1087.87$
		<b>0.006</b>		<b>0.015</b>	
Set 2	Sampled Points	37	13	14	3
	Elastic Modulus (kPa)	$985.99 \pm 1059.99$	$326.36 \pm 128.23$	$2288.18 \pm 1839.41$	$\times^\dagger$
		<b>0.031</b>		$\times^\dagger$	
Set 3	Sampled Points	7	21	34	26
	Elastic Modulus (kPa)	$\times^\dagger$	$186.40 \pm 204.21$	$400.03 \pm 328.23$	$308.29 \pm 241.91$
		$\times^\dagger$		0.236	

<sup>†</sup> Elastic modulus and p-value results in these fields are excluded due to insufficient sample size arising out of undersampling in the corresponding tissue regions.

localization errors arising out of manual registration methods, i.e. the AFM probings were carried out outside the specified annotations. Hence, no conclusive inferences could be made about the comparison between epithelial and stromal tissue response in normal and cancerous specimens in sets 2 and 3 respectively, and therefore, the elastic modulus values in the cancerous stromal regions in set 2 and normal epithelial regions in set 3 have not been presented in Table 2.3.

## 2.4 Conclusions

In this chapter, the results of preliminary AFM characterization studies on breast tissue specimens have been discussed. The preliminary feasibility studies indicate that the AFM holds the potential to objectively distinguish between normal and cancerous tissue. It was observed that cancer tissue exhibited significantly less stiffness than normal tissue and that epithelial regions exhibited less stiffness than stromal regions. It was also shown that cancerous epithelial regions were significantly softer than normal epithelial regions. Overall results indicated that tissue had higher stiffness as compared to previously reported measurements on cultured cell lines or isolated single cells [9],[10]; however, this is most likely attributed to the general tissue architecture in which the AFM studies are carried out. These results demonstrate the feasibility of applying AFM on histologically prepared tissue samples; and this approach can potentially provide a unique pathway to gaining insight into the biophysical changes at the onset and progression of breast cancer and other diseases.

The pilot studies also highlighted certain limitations of using the current experimental AFM system used for characterizing the tissue specimens. Since the AFM allows individual pointwise estimation of local stiffness in the tissue specimens, only fraction of the tissue provided on a TMA specimen could be sampled during each experiment setting. This is primarily due to the laborious nature of conducting these experiments, where specimens need to be manually translated after a force curve is acquired on a tissue region. Despite the fact that the AFM user visually registers stained and unstained tissue images to ensure AFM probings are conducted within the specified annotated region, such manual registration methods are not guaranteed to be completely error-free. As seen in the results in Table 2.3, stromal and epithelial regions were significantly undersampled by the AFM in sets 2 and 3 respectively due to incorrect probing localizations. This impediment is further aggravated when the number of annotations are limited. Reducing human intervention in carrying out these tasks by automating the process of region localization and automated indentation can increase robustness in characterizing breast tissue specimens using AFM. This is discussed in greater detail in chapter 3.

The elastic modulus values reported in this chapter also depend on the spring constant of the AFM probe being used. While several calibration schemes have been proposed [25][27], all of these methods report on a certain amount of variability ( $\sim 5-17\%$ ) [28]. Another concern with AFM indentation experiments is the sensitivity of the estimated elastic modulus to estimation errors in the contact point [29]. These issues are discussed in detail in chapter 4.

While the Hertz model was used to characterize the tissue specimens, it is true

that *a priori* assumptions of Herztian contact theory are not always applicable to soft biological samples that often exhibit hyperelastic behavior [30]. However , the focus of this preliminary work was to investigate the variations (if any) in stiffness in normal and cancerous tissue specimens, and the Hertz model provides a rough estimate of the stiffness of tissue specimens. Aspects of constitutive modeling of the tissue specimens are discussed in detail chapter 5.

## Chapter 3

# Improvements to the AFM experimental protocol for tissue characterization

### 3.1 Overview

In chapter 2, it was shown that using stiffness measures as a biomarker, contact-mode AFM could be used to differentiate spatially between normal and cancerous histological breast tissue specimens. By visually relating stained annotated images and unstained images acquired from AFM integrated optical microscope during AFM sampling, manual registration of tissue regions of interest (ROI) with the stained annotation was performed, and by using manual adjusting screws attached to the base of the AFM stage, the tissue specimens could be aligned with the AFM probe.

In this chapter, some of the shortcomings of using manual registration and positioning methods are discussed in detail that were briefly alluded to at the end of chapter 2. As opposed to pointwise tissue elasticity measures, elastic maps are proposed as a technique to quantify the spatial distribution of tissue specimen's elastic modulus. The development of a semi-automated image-guided positioning system to automate some of the positioning tasks involved in tissue characterization is reported in this chapter. Using the developed system, it becomes possible to



acquire much larger experimental datasets within the same experimental setting.

### 3.2 Problem Statement and Proposed Solution

There were several experimental challenges that were encountered in the preliminary AFM characterization studies in chapter 2. These are elaborated as follows:

- *Low sample size:* In the preliminary characterization studies, 78, 67 and 88 regions were sampled in experimental sets 1, 2 and 3 respectively. While the tissue elasticity did display a trend, characterization studies for conclusive histopathological inference would clearly require much larger datasets, potentially in the order of hundreds or thousands.
- *Low throughput during AFM experiments:* One of the primary causes for low sample size was the repetitive manual positioning tasks that were required to be carried out in between two consecutive force curve acquisitions. These included (a) moving the tissue slide so that another tissue region inside the annotation could be sampled, (b) manually registering the stained and unstained images and (c) translating the tissue slide to probe annotated regions in a different core. All these tasks carried out multiple times leads to AFM operator fatigue, and severely restricts throughput. A flowchart showing the various steps involved in manual tissue characterization is shown in Fig. 3.1.
- *Lack of Automated Registration:* As stated in the previous bullet point, manual registration remains another major impediment to improving throughput in conducting AFM based tissue characterization. The relatively large length

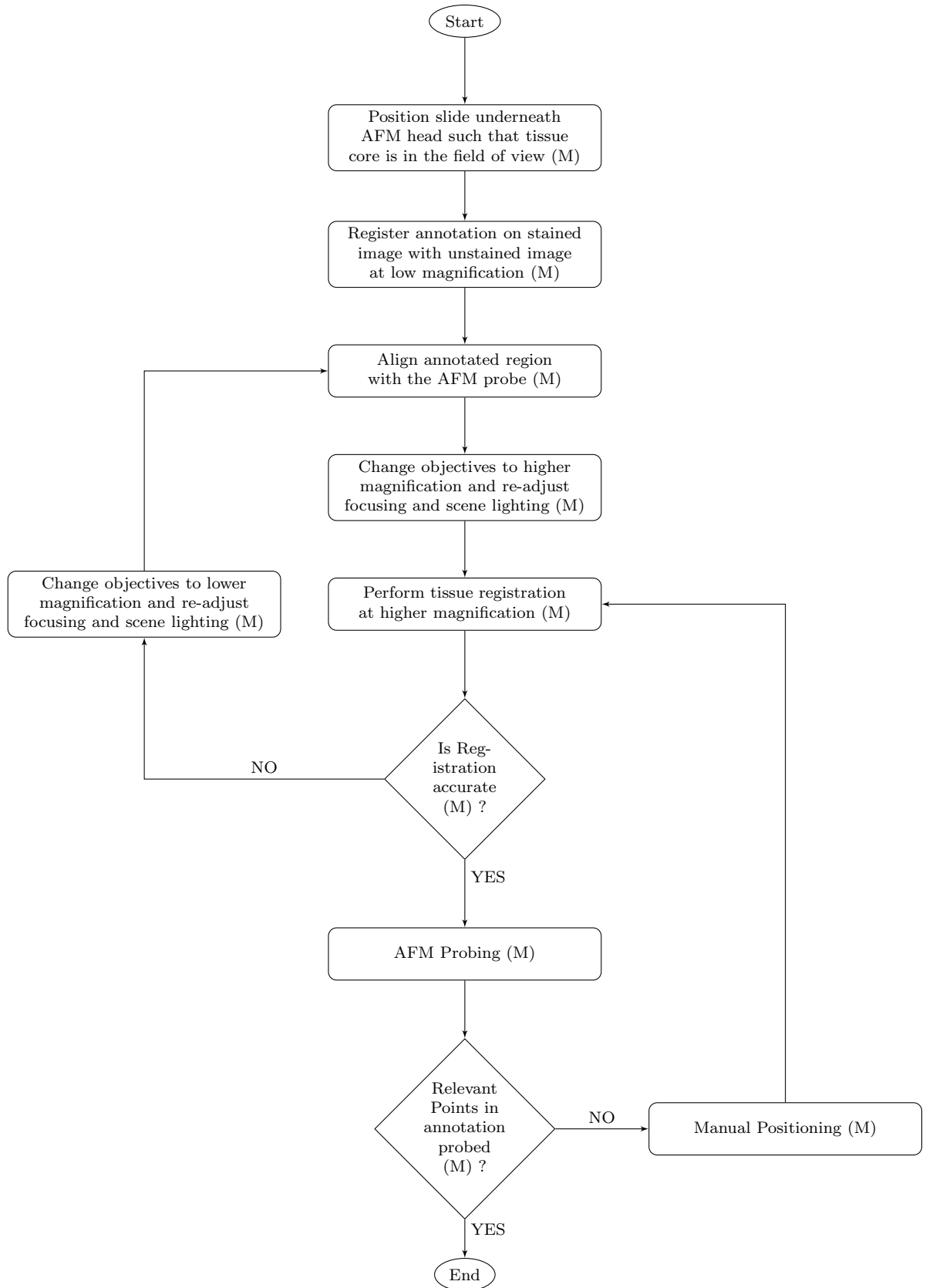


Figure 3.1: Flowchart describing manual AFM indentation experiments. (M) = Manual, (A) = Automated.

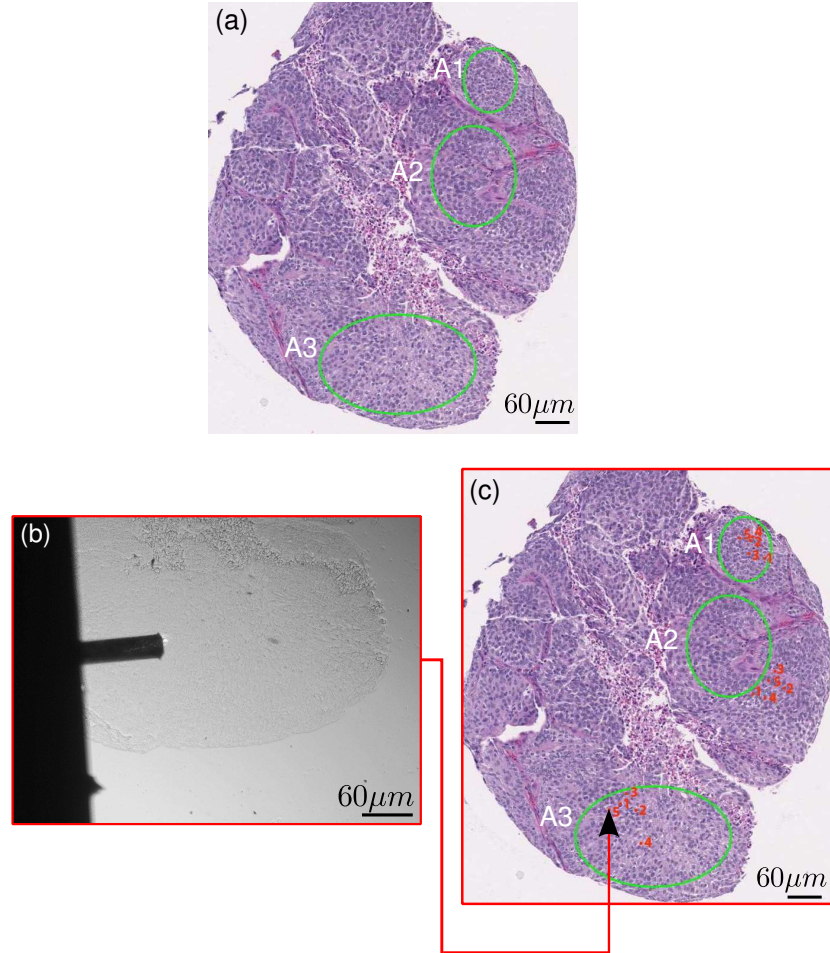


Figure 3.2: Manual registration between unstained and stained images. (a) Stained TMA core image annotated by the pathologist as regions A1, A2 and A3. (b) Brightfield image while performing AFM indentation on a point in annotation A3 after manually registering the stained image (c) Stained TMA core image overlaid with the points probed during AFM experiments on the unstained slide. Observe that annotation A2 has been incorrectly sampled by the AFM.

scale of the TMA cores ( $\sim 600 \mu\text{m}$  in diameter) implies that the whole tissue core is not visible at high magnifications under the optical microscope. Therefore it becomes necessary to zoom in on a ROI to locate annotations desired to be phenotyped and then revert back to a coarse magnification to get a larger perspective of the alignment of the ROI and the AFM probe (see Fig. 3.1). Furthermore, the image of the tissue specimen acquired by the optical microscope has to be registered with the stained and annotated image to ensure the AFM probing is restricted to the annotated regions on the stained image. Poor image contrast in the unstained slide leads to difficulty in manual registration of the stained and unstained images and as seen in the results in chapter 2, it might lead the AFM operator to conduct probing outside the regions annotated by the pathologist (see Fig. 3.2).

**Hypothesis:** Positioning and registration automation can overcome several of the aforementioned shortcomings of using manual AFM probe-tissue alignment prior to tissue indentation.

The following solutions are proposed to improve the AFM experimental protocol for tissue characterization using AFM:

- *Raster scanning for generating elastic maps:* By acquiring a set of force curves from points at precise spatial intervals on a tissue region of interest (ROI), a two-dimensional map of the tissue elasticity can be constructed. Each force curve can be processed and assigned a definite pixel of a topographic image, where the pixel value corresponds to the elastic modulus of force curve acquired

at the pixel location. This resulting image is typically called an “elastic map” [31] or a “force-volume” [18].

Elastic maps are proposed as a technique to quantify the spatial distribution of tissue specimen’s elastic modulus. The AFM X-Y stage, which is typically employed for imaging applications, can be used for positioning the tissue specimen at pre-specified spatial intervals.

Table 3.1: X-Y travel range of automated AFM scanners, arranged in increasing order of their travel range.

AFM Vendor	(X-Y) Stage Vendor	Travel Range ( $\mu m$ )
Asylum Research Inc.	Asylum Research, Inc.	90
Agilent 5420	Agilent	90
JPK Instruments, Inc.	Tip Assisted Optics (TAO) stage from Physik Instrumente, Germany	100
Bruker, AXS	Bruker, AXS	150

- *Large scanning operations with improved registration:* While the commercial AFM X-Y stages are capable of closed-loop accurate position control, they are limited by their range of travel ( $\sim 90 - 150 \mu m$ ) range for closed-loop positioning (see Table 3.1). For acquiring elastic maps on small tissue ROIs, the AFM X-Y stage might be sufficient, however, it would not be possible to scan regions beyond a  $90\mu m \times 90\mu m$  ROI. Moreover, the AFM X-Y stage still does not resolve the registration problem.

To account for large ROI scanning operations and repeated manual registration, a semi-automated *image-guided positioning system* (IGPS) is proposed. Essentially, this system uses a micromanipulator with a large X-Y travel range

to align the tissue specimens with the AFM probe prior to AFM indentation using closed-loop image feedback from the camera mounted to the inverted microscope. As described later in section 3.5, this system also addresses key manual registration challenges.

In the subsequent sections 3.3, 3.4 and 3.5, details of the design and implementation of the IGPS system are discussed.

### 3.3 AFM experimental setup with the IGPS

In the modified AFM system, an additional motorized MP-285 micromanipulator (manufactured by Sutter Instruments, Novato, CA) is used for translating the tissue slide, which is situated at the base of the microscope on the vibration isolation table. Attached to the MP-285 is a custom-made end-effector to which the tissue slide is mounted. The slide is placed between the AFM X-Y stage and AFM probe. The MP-285 has a step resolution of 40 nm and a range of 2.54 cm on both X and Y axes, and this enhanced X-Y travel range makes it possible to scan ROIs much larger than  $90\mu m \times 90\mu m$ .

Since the forces measured during AFM indentation experiments are in the nm-range, chatter in the end-effector or the slide can lead to incorrect mechanical property estimation and can potentially damage the AFM probe and the tissue sample. To eliminate vibrations in the slide, the end-effector was fabricated using Aluminum and the slide was clamped to the end-effector using a clamping screw (Fig. 3.3 inset). Additionally, an adhesive tape was used to firmly attach the slide

to the end-effector. It was observed that using this arrangement, there were no perceptible vibrations in the slide/end-effector, as mentioned in section 3.5.

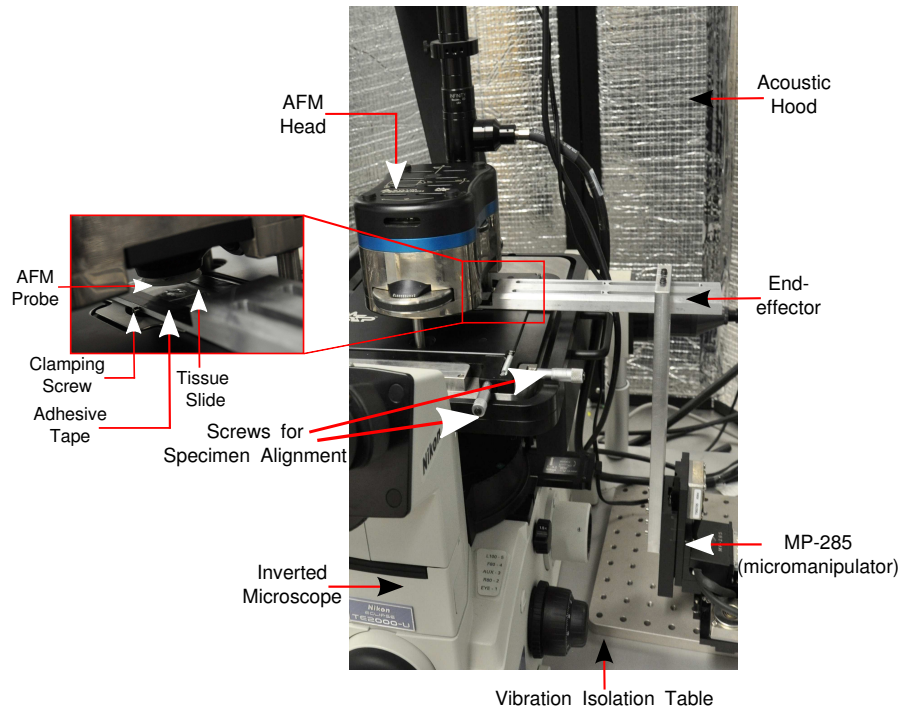


Figure 3.3: AFM Experimental Setup with the MP-285 micromanipulator ©2013 IEEE.

## 3.4 Image-Guided Navigation

### 3.4.1 Tracking of the ROI

The presence of vision in the loop allows the AFM operator to select a certain ROI and place the ROI underneath the AFM probe tip in an automated manner. Some of the popular tracking algorithms are gradient-based methods like the Kanade-Lucas-Tomasi (KLT) feature tracker [32] and the Scale-Invariant Feature Transform (SIFT) [33]. However, as seen in Figs. 2.2(d) and 2.2(e) in chapter 2,

the unstained tissue images are characterized by low contrast and therefore unique feature vectors are difficult to compute. In many cases, features of high contrast (extracted from the images) have been external particles in the fluid environment, which tend to move around randomly during the motion of the tissue slide underneath the AFM probe (see Fig. 3.4).

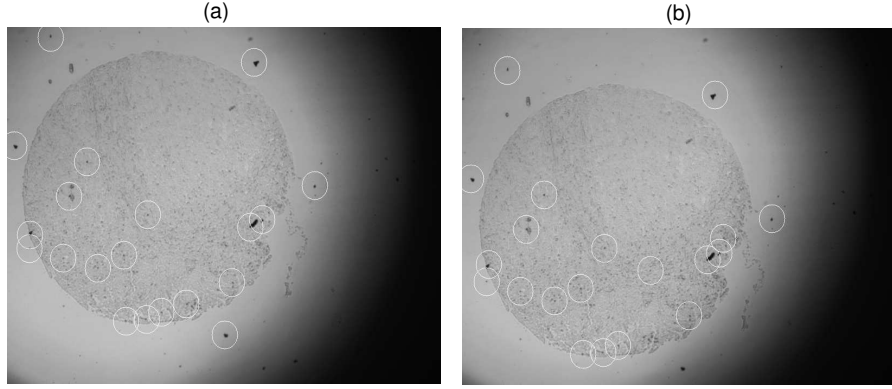


Figure 3.4: Extracted features with strong intensity gradients. Observe that prominent features are impurities floating in the liquid environment of the sample.

As a result, normalized cross-correlation based template matching algorithm [34] is used to ensure robust tracking of the ROI during the motion of the slide (see Fig. 3.5). Though the applicability of such methods are conditional upon uniform scene lighting and in-plane translation without rotation, these conditions could be enforced by: (1) manually adjusting the external lighting and (2) ensuring that there is no relative motion in the various interconnected parts of the end-effector.

The implementation of the tracking algorithm is given as follows:

For an image,  $I_t = \{I(p_x, p_y, t) | 0 \leq p_x \leq R, 0 \leq p_y \leq C\}$ , and a ROI,  $T = \{T(p_x, p_y, t) | 0 \leq p_x \leq r, 0 \leq p_y \leq c\}$ , where  $I_t$  and  $T$  are the image and the ROI respectively at the  $t^{th}$  frame, the estimated position of the ROI at the  $t + 1^{th}$



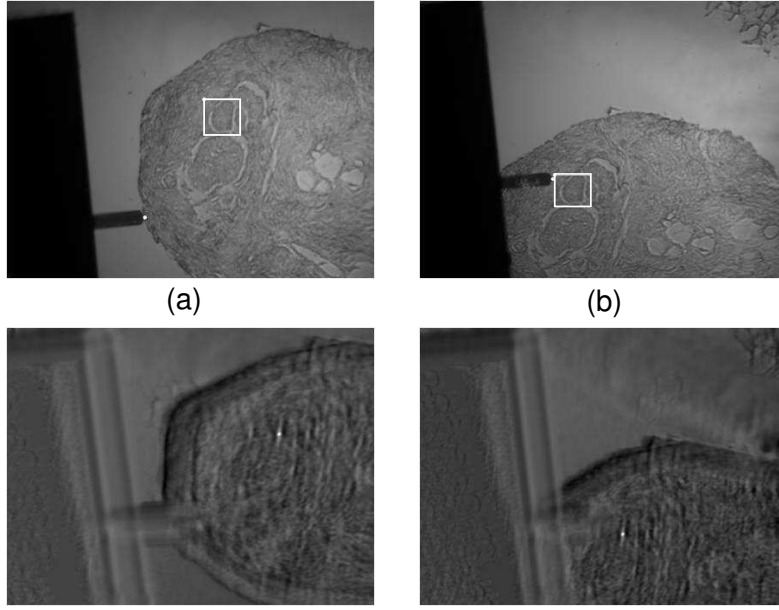


Figure 3.5: Normalized cross correlation algorithm used for tracking at two time instants (a) and (b). The top images correspond to  $I_t = I(p_x, p_y, t)$  with the ROI marked with a white box, while the bottom ones are the result images  $R$ , where with the estimated ROI position  $(\hat{p}_{x,t+1}, \hat{p}_{y,t+1})$  appear as spots of high intensity.

frame is given by [34]:

$$(\hat{p}_{x,t+1}, \hat{p}_{y,t+1}) = \arg \max_{p_x, p_y} R \quad (3.1)$$

where  $R$ , the result image is given by:

$$R = \frac{\sum_{p'_x, p'_y} [T(p'_x, p'_y) I_{t+1}(p_x + p'_x, p_y + p'_y)]}{\sqrt{\sum_{p'_x, p'_y} T(p'_x, p'_y)^2 \sum_{p'_x, p'_y} I_{t+1}(p_x + p'_x, p_y + p'_y)^2}} \quad (3.2)$$

The numerator of the expression in Eqn.(3.2) indicates the correlation of the image and the ROI, while the denominator is the normalizing term to ensure that general lighting differences in both the image and the ROI do not affect the tracking algorithm significantly. The tracking algorithm was implemented in Visual C++ using

OpenCV libraries [35].

### 3.4.2 Control Scheme

The control law in discrete state space form is given by:

$$\mathbf{X}(k+1) = \mathbf{X}(k) + \mathbf{u}(k) \quad (3.3)$$

$$\mathbf{Y}(k) = S\mathbf{R}\mathbf{X}(k) \quad (3.4)$$

where

$$S = \begin{bmatrix} s_x & 0 \\ 0 & s_y \end{bmatrix}; \quad R = \begin{bmatrix} \cos(\theta_0) & -\sin(\theta_0) \\ \sin(\theta_0) & \cos(\theta_0) \end{bmatrix} \quad (3.5)$$

$\mathbf{Y} = \begin{bmatrix} p_x & p_y \end{bmatrix}^T$  and  $\mathbf{X} = \begin{bmatrix} x & y \end{bmatrix}^T$  represent the image and manipulator frame coordinates respectively.  $R$  is the rotation matrix between the manipulator and the image frame while  $S$  is a scaling matrix relating the two frames. The parameters of  $R$  and  $S$  are estimated in a pre-experiment calibration step using a cover-slip with uniform grids marked at  $100 \mu\text{m}$  separation, as shown in Fig. 3.6.  $\mathbf{u}(k)$  is the control input in the manipulator frame.

To estimate the control input, a gradient-descent based approach [36] is used, where the control input  $\mathbf{u}(k)$  is based on the gradient of the function:

$$F[\mathbf{X}(k)] = [\mathbf{X}(k) - \mathbf{X}_{tip}]^T [\mathbf{X}(k) - \mathbf{X}_{tip}] \quad (3.6)$$

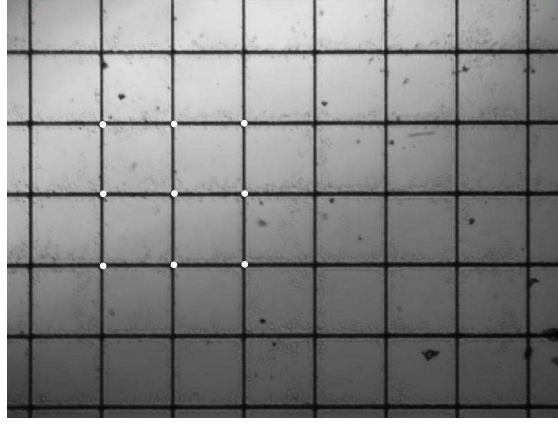


Figure 3.6: Calibration of the scaling matrix  $S$  using a cover-slip with uniform grids at  $100\ \mu m$ .

The control input  $\mathbf{u}(k)$  is therefore given as:

$$\mathbf{u}(k) = -\gamma(k)\nabla F[\mathbf{X}(k)] = -2\gamma(k)[\mathbf{X}(k) - \mathbf{X}_{tip}] \quad (3.7)$$

where the step size  $\gamma(k)$  is given by:

$$\gamma(k) = \begin{cases} \frac{\gamma_0}{2\|\mathbf{X}(k) - \mathbf{X}_{tip}\|}, & \text{if } \|\mathbf{X}(k) - \mathbf{X}_{tip}\| > \epsilon \\ 0, & \text{if } \|\mathbf{X}(k) - \mathbf{X}_{tip}\| \leq \epsilon. \end{cases} \quad (3.8)$$

$\gamma_0$  is a constant that determines the magnitude of the incremental travel of the ROI towards the probe tip  $\mathbf{X}_{tip}$ . The positioning is terminated once the ROI is within a radius of  $\epsilon$  from the probe tip, where  $\epsilon$  is a preset parameter.

It is vital to ensure that parts of the tracked ROI are not occluded by the AFM probe during positioning since the template matching algorithm requires the entire ROI to be visible in the image space. As a result, the estimated position of

the slide in image coordinates,  $\mathbf{Y}$ , is selected to lie on the upper-corner of leading edge of the ROI, as shown in Fig. 3.7(b).

### 3.5 ROI positioning protocol

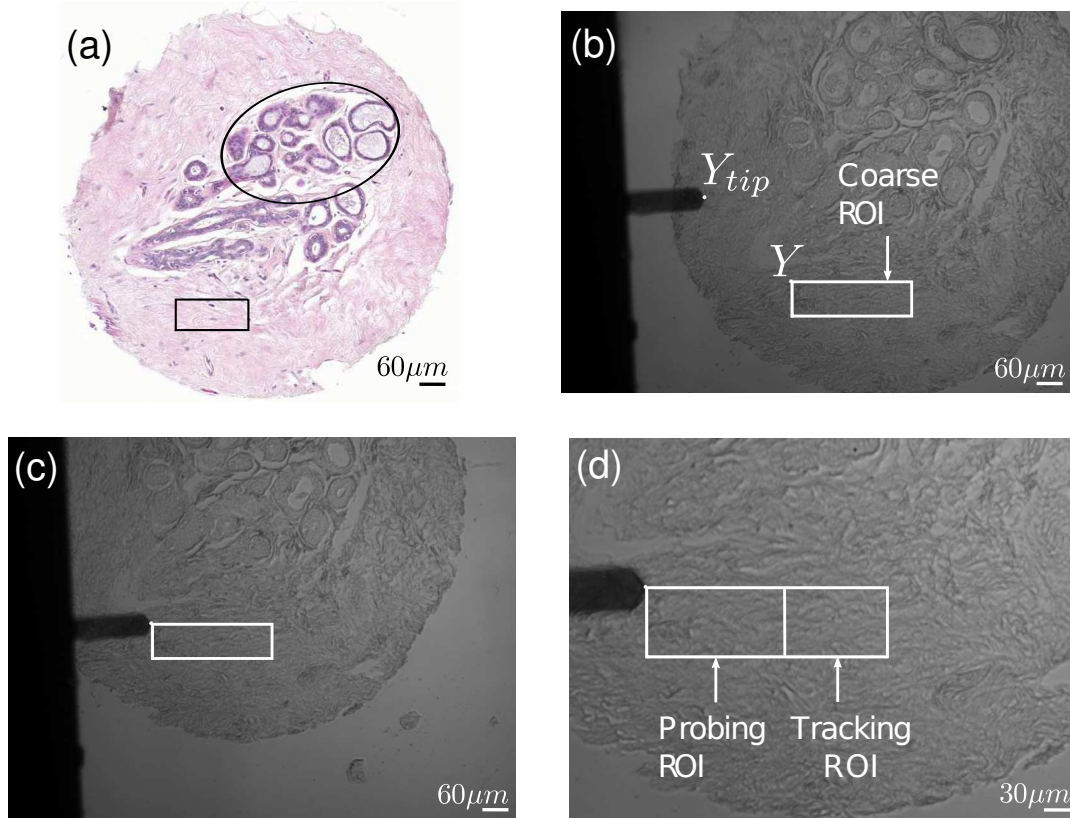


Figure 3.7: Tracking protocol for probe-ROI alignment at 10X and 20X. (a) Stained image of tissue core annotated by the pathologist at low resolution (10X). (b) Bright-field image from the AFM-optical microscope. A coarse ROI is selected to match one of the annotated regions in (a). (c) Positioning at 10X. (d) Registration of the coarse ROI at 20X ©2013 IEEE.

Using the tracking algorithm and the control law described in section 3.4, the following protocol is implemented for alignment of the tissue ROI and the AFM probe tip (see Fig. 3.7).

- A coarse ROI is selected at low magnification ( $m_1 = 10\times$ ), after visually correlating the annotated regions from the stained image [Fig. 3.7(a)] and the brightfield image from the AFM-optical microscope [Fig. 3.7(b)]. The AFM probe tip is also selected visually at the same magnification [Fig. 3.7(b)].
- Based on the tracking algorithm and control law discussed, the ROI is positioned within an error of  $\epsilon$ , chosen to be  $2\ \mu m$  [Fig. 3.7(c)].
- The objectives, lighting and focusing are altered manually at higher magnification ( $m_2 = 20\times$ ) to ensure that the probe tip and the ROI is in focus and the scene is uniformly lit. The AFM tip is then selected visually by the user at high magnification,  $m_2$ . Since the probe tip is stationary, it serves as a reference for the coarse ROI, which is recreated at a distance  $m_2\epsilon/m_1$  from the tip at  $m_2$  magnification [Fig. 3.7(d)]. *This allows registration of the same ROI across multiple magnifications.* At  $m_2$  magnification, finer details are visible to the user and a part of the recreated ROI is selected, called the probing ROI, which is probed by the AFM. The remaining part of the recreated ROI serves as the tracking ROI. The probing ROI is then sampled in a raster fashion, while the tracking ROI is used to provide image feedback [Fig. 3.7(d)].

In the IGPS, the user has to visually register the stained and unstained images only twice during the course of the experiment: first, during the selection of the Coarse ROI at low magnification and second, during the selection of the probing ROI at higher magnifications (see Fig. 3.8). This is a marked improvement over manual registration procedures, where the AFM user has to visually register the

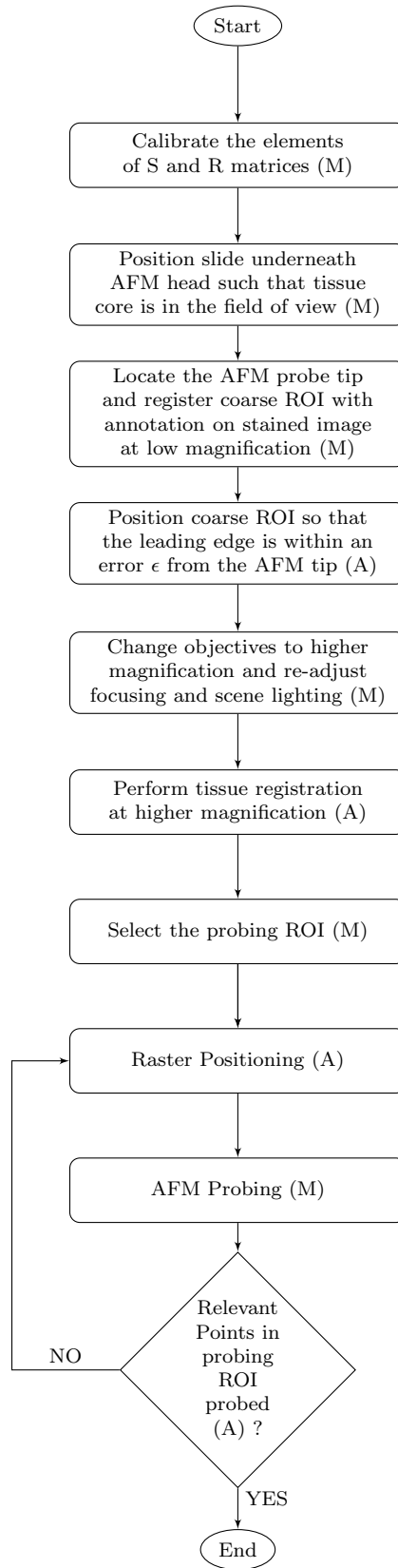


Figure 3.8: Flowchart describing AFM indentation experiments using the image-guided positioning system (IGPS). (M) = Manual, (A) = Automated.

annotated ROI on the unstained image periodically to ensure that the AFM probings are carried out within the specified annotations (see Fig. 3.1).

A representative AFM force curve obtained from samples mounted on the IGPS is shown in Fig. 3.9(a) and Fig. 3.9(b). Minimal fluctuations in the deflection data is indicative of negligible vibrations introduced due to the end-effector design.

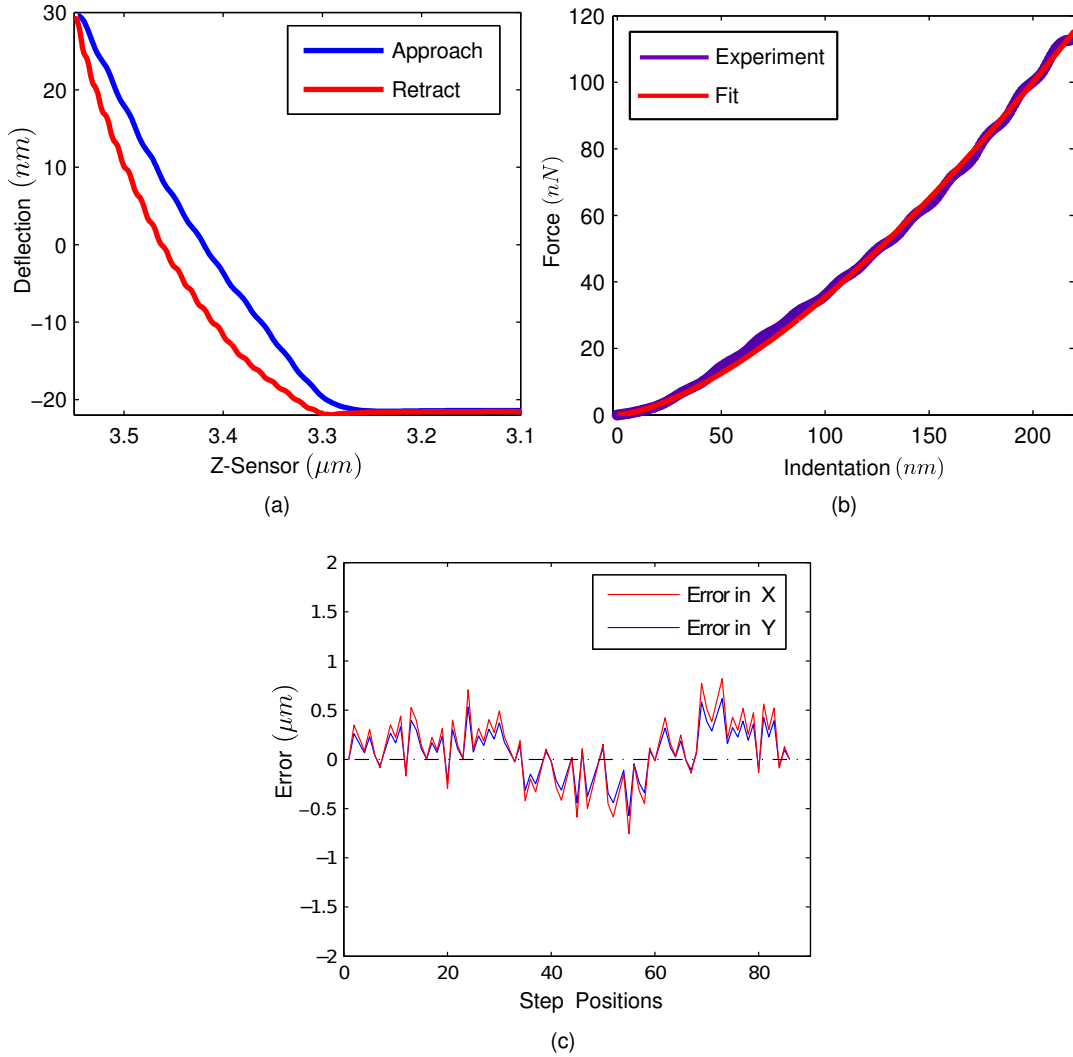


Figure 3.9: (a) Representative AFM force curve on a tissue sample mounted on the end-effector. (b) Corresponding force-indentation curve overlaid with the Hertzian fit and (c) Tracking Performance ©2013 IEEE.

The positioning accuracy is demonstrated in Fig. 3.9(c), where the slide is translated from its original position (262,226) to  $\mathbf{Y}_{tip} = (163, 362)$  in the image space. The positioning errors at the completion of alignment at 10x and 20x were 1.6  $\mu\text{m}$  and 0.8  $\mu\text{m}$  respectively, which are acceptable alignments errors.

## 3.6 Results and Discussion

A combination of the AFM X-Y stage and the IGPS was used to obtain elastic maps from the tissue specimens. In the case of the AFM X-Y stage, the annotations on the stained slide were manually registered with the unstained slide and a  $60\mu\text{m} \times 60\mu\text{m}$  ROI inside the annotation was raster-scanned. In the case of the IGPS, the protocol given in section 3.5 was followed to define the probing ROI on which raster-scanning was performed.

Due to the relative ease of the force-controlled mode, this mode was used to acquire the force curves and a deflection setpoint of 50 nm was used. Using the contact point estimation scheme [24] and the Hertz contact model [26] described in chapter 2 to fit the experimental data, the AFM force curves were post-processed to obtain the elastic maps.

### 3.6.1 Characterization of Epithelium-Stroma boundary

Due to the sharp differences in elasticity in the epithelial and stromal tissue regions in both normal and cancer specimens, the boundaries of these two tissue types were identified and raster-scanned.



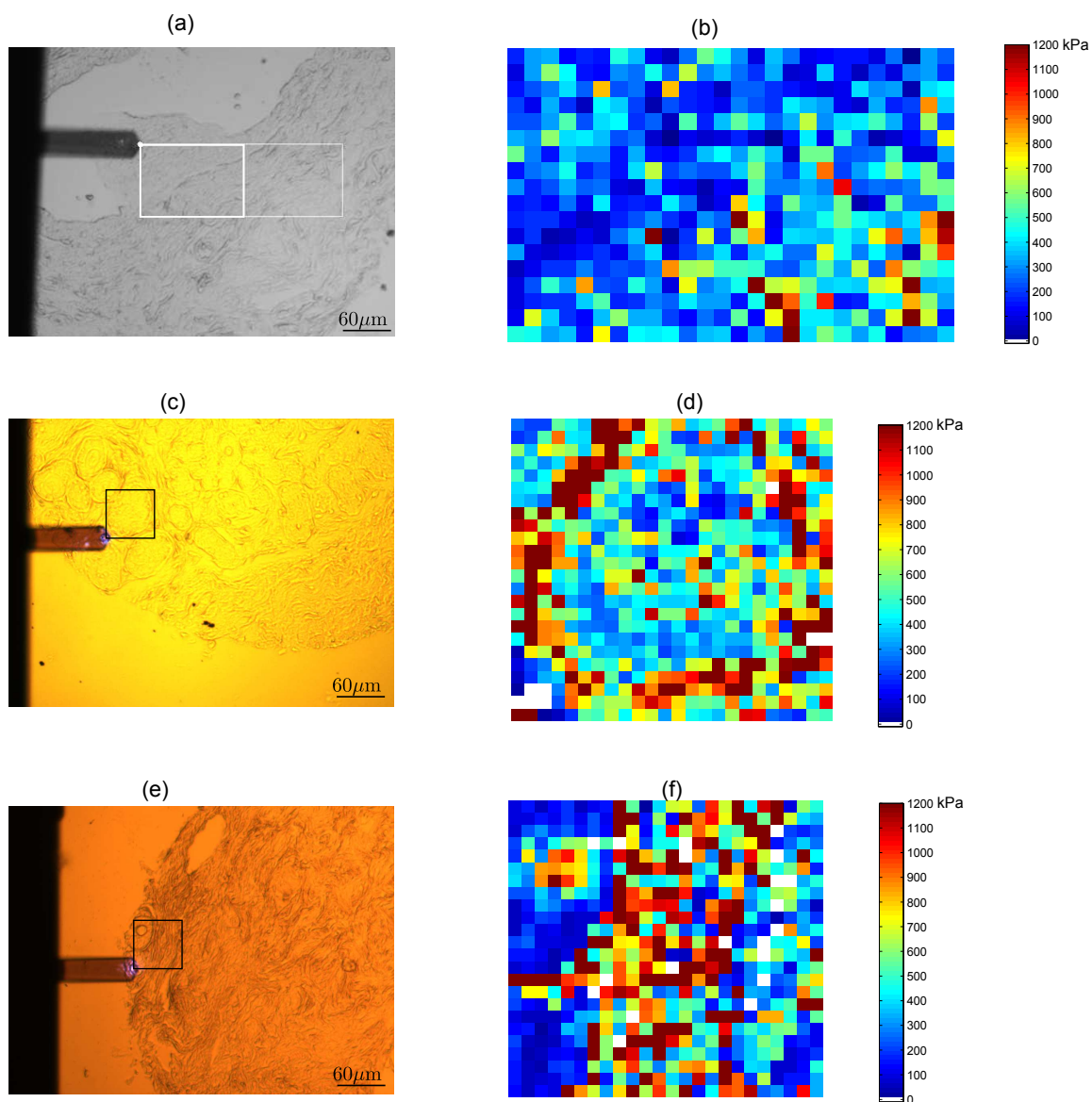


Figure 3.10: Elastic maps on normal tissue cores along with their corresponding brightfield images.

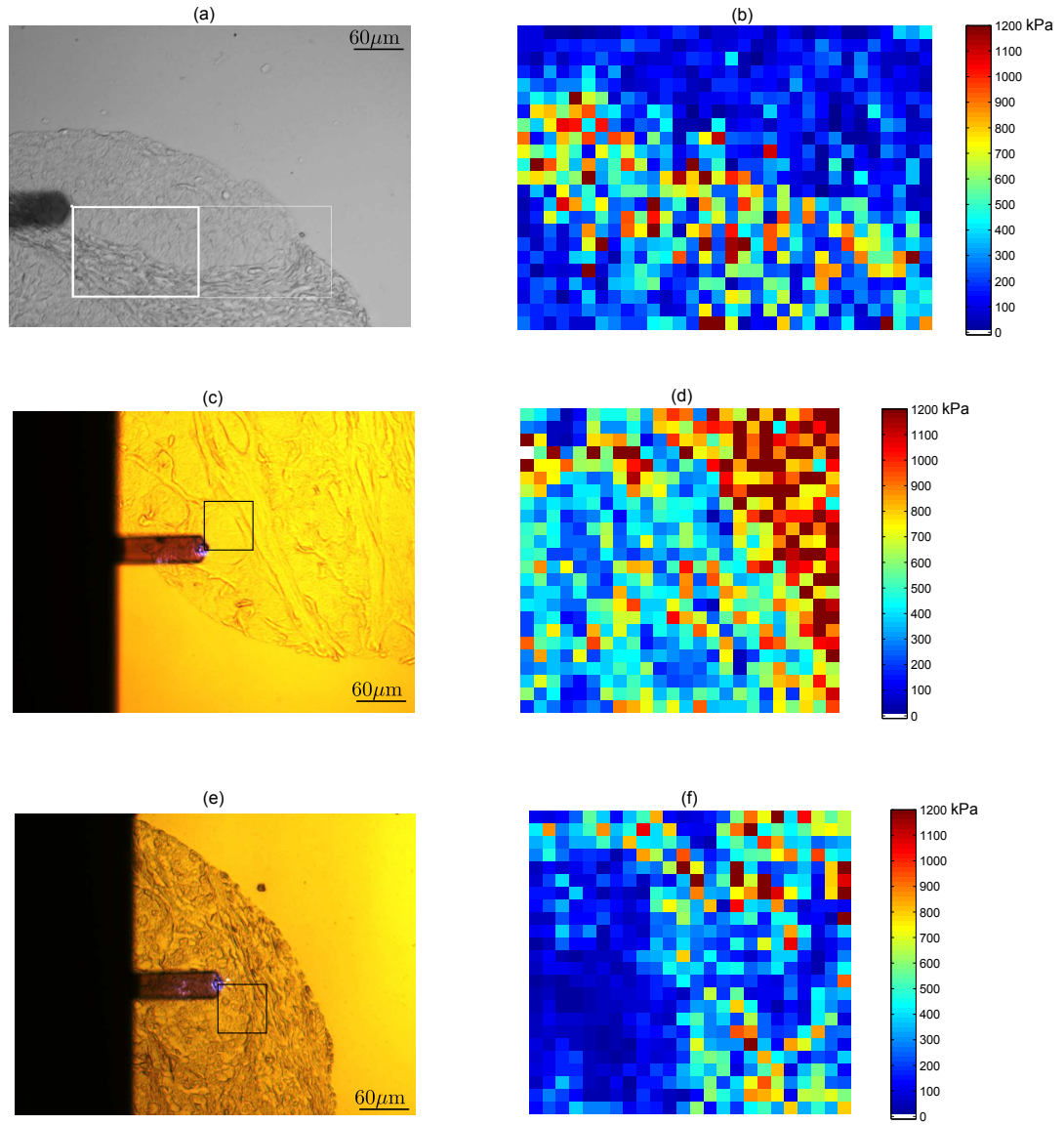


Figure 3.11: Elastic maps on cancer tissue cores along with their corresponding brightfield images.

Raster-scanning results on the epithelium-stromal tissue boundaries on normal and cancer specimens are shown in Figs. 3.10 and 3.11 respectively. The first column in Figs. 3.10 and 3.11 correspond to the brightfield image of the probed region on the tissue core, while the second column represents the corresponding elastic map. The first row images in Figs. 3.10 and 3.11 correspond to elastic maps on probing ROIs ( $115\mu m \times 160\mu m$ ) and ( $90\mu m \times 130\mu m$ ) on a normal and cancer core respectively, acquired by the IGPS and sampled at  $5\mu m$  spatial intervals. The second and third row images in Fig. 3.10 and Fig. 3.11 correspond to AFM X-Y stage acquired  $60\mu m \times 60\mu m$  elastic maps sampled at  $2.5\mu m$  spatial intervals.

In all the elastic maps, a clear delineation between the two tissue regions is clearly observed: the softer regions correspond to epithelial tissue, while the stiffer regions are the stroma. These results validate the observations in chapter 2, where epithelial tissue in both normal and cancerous specimens were more deformable compared to stromal tissue.

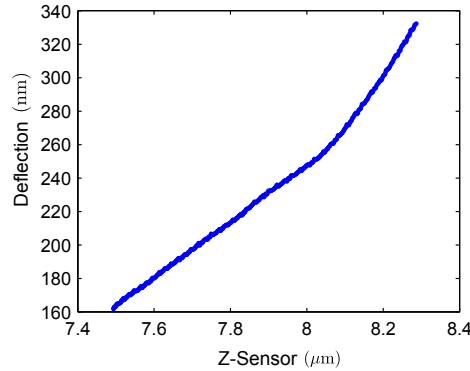


Figure 3.12: Uninterpretable force curve with no prominent non-contact regime.

It should be noted that during the raster-scanning, some force curves were

acquired where no defined contact point existed, as shown in Fig. 3.12. These types of force curves are typically acquired when the tissue specimen has started translating before the probe has completely retracted from the specimen surface [37]. These uninterpretable force curves were not considered in constructing the elastic map, and pixels corresponding to these force curves were replaced by blank white spaces, as seen in Figs. 3.10(d), Fig. 3.10(f) and Fig. 3.11(d).

### 3.6.2 Characterization of patient specific tissue specimens

The preliminary characterization experiments in chapter 2 were conducted on normal and cancer tissue cores compiled from multiple patients. In this section, patient-specific tissue characterization results are reported, primarily to investigate if there was any tendency of the tissue response depending on the patient from whom the cores were extracted.

Table 3.2: AFM experimental setting parameters.

Set	Patients	Calibrated Spring Constant	Theoretical Spring Constant
1	A,B,C	0.596 N/m	0.95 N/m
2	D,F,G,H	0.589 N/m	0.95 N/m

Two sets of experiment were conducted to investigate the tissue response from 7 patients (details in Table 3.2). Patient-specific results are tabulated in Table 3.3. On observation, it can be seen that that stromal tissue is stiffer compared to epithelial tissue, as observed previously during raster scans at the epithelium-stroma interface.

Table 3.3: Summary of AFM raster-scanning results on patient specific tissue specimens. Results expressed as mean  $\pm$  standard deviation.

		Epithelial		Stromal	
		Normal	Cancerous	Normal	Cancerous
Patient A	Sampled Points	$\times$	2285	$\times$	537
	Elastic Modulus (kPa)	$\times$	$419.65 \pm 312.41$	$\times$	$1149.10 \pm 675.10$
Patient B	Sampled Points	$\times$	1144	$\times$	$\times$
	Elastic Modulus (kPa)	$\times$	$461.86 \pm 264.09$	$\times$	$\times$
Patient C	Sampled Points	576	$\times$	565	$\times$
	Elastic Modulus (kPa)	$512.34 \pm 251.53$	$\times$	$902.73 \pm 524.86$	$\times$
Patient D	Sampled Points	$\times$	1152	$\times$	$\times$
	Elastic Modulus (kPa)	$\times$	$359.49 \pm 236.16$	$\times$	$\times$
Patient E	Sampled Points	$\times$	2304	$\times$	$\times$
	Elastic Modulus (kPa)	$\times$	$152.20 \pm 111.46$	$\times$	$\times$
Patient F	Sampled Points	$\times$	$\times$	576	$\times$
	Elastic Modulus (kPa)	$\times$	$\times$	$714.82 \pm 348.07$	$\times$
Patient G	Sampled Points	3452	$\times$	$\times$	$\times$
	Elastic Modulus (kPa)	$240.61 \pm 144.15$	$\times$	$\times$	$\times$

It was also observed that cancer epithelial and normal epithelial tissue response was not uniform across patients. While patients A and B show similar mean elastic modulus in cancer epithelial regions, patients D and E show vastly dissimilar elastic modulus values. Cancer epithelial regions in Patient E showed significantly lower tissue response compared to normal epithelial regions in Patient G, however, when the cancer epithelial response from Patient D was included (conducted in the same experimental setting), the hypothesis of reduction in elastic modulus with cancer progression could no longer be considered valid.

These results clearly indicate that normal and cancer tissue extracted from the same patients are necessary to draw meaningful conclusions about tissue property alterations with cancer progression. Due to time constraints and unavailability of paired tissue specimens from the same patient, tissue response from the same patient could not be investigated, and this remains a subject of future work.

### 3.7 Conclusions

In this chapter, several improvements to the original AFM experimental protocol was proposed. The major contributions in this chapter are as follows:

1. *Improved Sample Size:* Using a combination of the AFM X-Y stage and an image-guided positioning system (IGPS), sample size (upto two orders in magnitude) could be significantly increased, thus confirming the research hypothesis of this chapter. The AFM X-Y stage is employed to perform small scans, while the IGPS allows scans on much larger ROIs. This is especially relevant to

the study of relatively large histopathological breast tissue microarrays, where malignancies of interest are not easily isolated within a small tissue region.

2. *Improved Registration:* The use of the image-guided positioning system allows significant reduction in manual registration of the stained and unstained images. The user requires to perform manual registration only twice during the course of the AFM experiments, as opposed to reviewing the position of the ROI on the unstained image with respect to the annotated image periodically in manual positioning operations.

There are, however, certain limitations with the IGPS, which are elaborated as follows:

1. *User interventions in microscope operations required:* Though manual positioning operations could be significantly reduced, the AFM user is still required to shift objectives, alter the objective focal length and adjust the scene lighting manually. It is possible to automate these tasks, however, these automated options are not currently available in the inverted microscope (Nikon TE2000U).
2. *Absence of automated registration between the stained and unstained images:* Further user intervention could be reduced by performing automated registration between the annotated regions in the stained and the unstained tissue images. This would require performing multimodal registration since the two images are acquired by different scanning systems in dissimilar lighting environments.

Larger datasets implied that stronger conclusions could be drawn from the AFM measurements. While delineations at the boundaries of epithelium and stroma tissue could be clearly seen, it was also observed that the tissue properties also depend on the patient from whom the tissue cores were extracted. It is therefore proposed that normal and cancerous tissue pairs from the same patient be extracted and characterized by the AFM.



## Chapter 4

### Probabilistic Estimation of the Elastic Modulus

#### 4.1 Overview

In chapter 3, it was demonstrated that by using an image-guided positioning system with a range much larger than commercial AFM stages, considerable human intervention could be reduced in AFM tissue characterization experiments. In addition to reducing the time taken to conduct the experiments, large-scale AFM indentation data acquisition was shown possible. To exploit the full potential of the image-guided automated positioning system, it is necessary to develop robust computational methods to automate the mechanical property extraction from large-scale raw AFM force curves.

As discussed in chapter 2, an accurate material characterization procedure from the AFM experimental data entails unequivocal determination of the following experimental parameters: the contact point on the AFM force curve and the spring constant of the AFM probe. A derivative-based algorithm was used to determine the contact point [24], and the thermal method was used to calibrate the AFM probe spring constant [25] to obtain the results in chapter 2. The challenges in accurate determination of the contact point and the probe spring constant were briefly alluded to at the conclusion of chapter 2.

In this chapter, the sensitivity of the estimated mechanical property to uncer-

tainties in these two experimental parameters are discussed in detail. A probabilistic mathematical model based on Bayesian analysis is proposed to estimate the mechanical property after accounting for observed uncertainties in the contact point and the probe spring constant. In section 4.2, causes for uncertainty in the experimental parameters are reviewed. In section 4.3, the details of the mathematical model are described. In section 4.4, results of implementation of the model on simulated and experimental AFM force curves are shown. This chapter closes with discussions of the proposed model with its merits and demerits in section 4.5.

## 4.2 Problem Statement and Proposed Solution

### 4.2.1 Uncertainty in the contact Point

The determination of the contact point is a vital component of the mechanical property extraction process because it determines the amount of indentation caused due to the vertical travel of the AFM probe. A representative AFM force curve on a fixed mouse Embryonic Stem Cell (mESC), is shown in Fig. 4.1. It is evident from Fig. 4.1 that the force curve displays a smooth transition from the non-contact regime to the contact regime. This is typical of compliant biological samples like cells and tissue, and this smooth nature of the transition leads to considerably difficulty in ascertaining the contact point. On stiff substrates in air, the AFM force curve while approaching the sample shows a prominent attractive region (primarily contributed by the van der Waal's forces and capillary forces [38]), which causes the first derivative of the force curve to change sign when the contact forces take

over [39]. However, this approach is invalidated for compliant specimens like cells and tissue in liquid environments. As seen in the Fig. 4.1, there is no perceptible attractive region in the approach curve while indenting biological specimens.

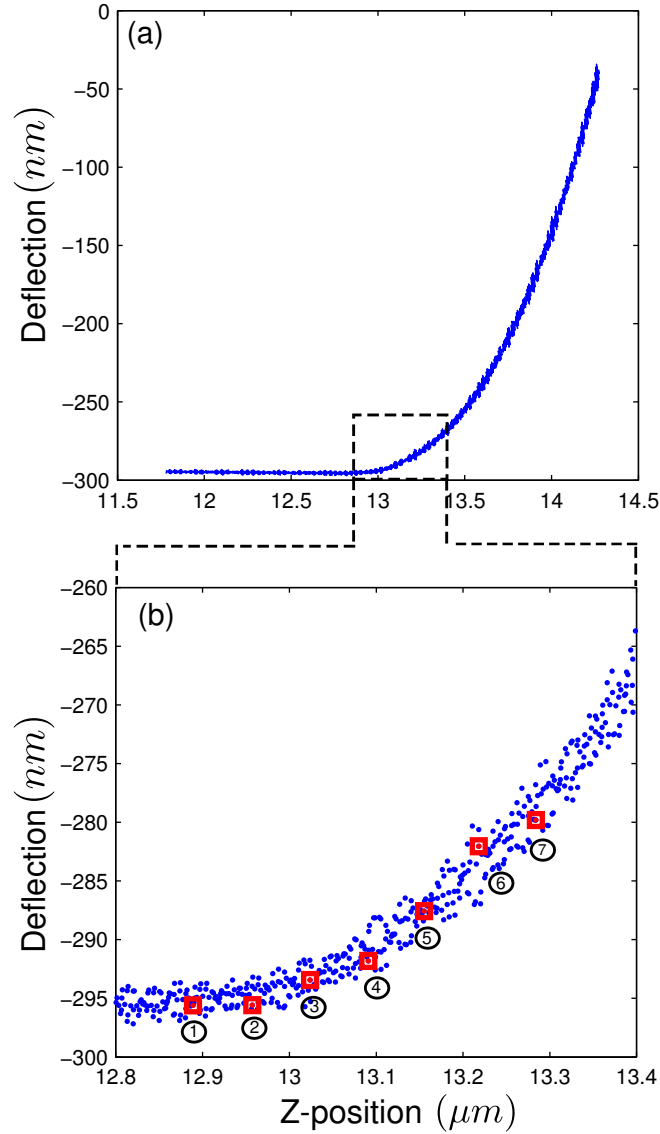


Figure 4.1: Representative AFM force curve on mESC, with candidate contact points shown in red blocks: (a) Whole AFM force curve and (b) transition region from non-contact to contact regime.

The effect of uncertainty in the contact point on the elastic modulus computed

using a Hertzian fit [24] is shown in Table 4.1. Over a wide range of candidate contact points, the elastic modulus varies by a factor of 42% [expressed as (min - max)/ave ].

Table 4.1: Variation of elastic modulus with change in contact point.

Contact Point	1	2	3	4	5	6	7
Elastic Modulus (kPa)	13.28	14.29	15.35	16.50	17.72	19.03	20.52

Over the years, researchers have proposed various strategies to estimate the point of contact in AFM force curves. Most contact estimation algorithms can be broadly divided into three categories : purely fit-based, purely derivative based and a combination of fit and derivative based algorithms. Following is a brief description of the existing algorithms in literature, together with their strengths and weaknesses.

- Purely Derivative-based Approaches

- Pillarisetti *et al.* [24] and Nyland and Maughan [40] assumed contact when the first derivative of the deflection with respect to the Z-position exceeded a threshold.
- Radermacher [41] detected the contact point as the point of discontinuity in the first derivative of the raw force curve.
- *Advantages:* These methods are independent of the contact-model used to extract the material properties.
- *Disadvantages:* Computing derivatives in the presence of noisy data could lead to incorrect estimates. Moreover, smoothness of the transition re-

gion might preclude any prominent changes in the first derivative of the deflection. In addition, selection of the threshold parameter to detect the change in the deflection derivative [24],[40] is largely subjective and is prone to noise in the non-contact regime.

- Derivative and fit-based Approaches

- Jaasma *et al.* [39] used a piecewise quadratic function to fit the deflection data in the force curve, and estimated the contact point as the point where the extrapolated first derivative of the fitting function exhibited zero-crossings.
- Charras *et al.* [42] and Radermacher *et al.* [43] solved for the contact point and the elastic modulus simultaneously by taking two points on the force curve, whose existence in the contact regime was beyond doubt.
- Dimitriadis *et al.* [44] performed a unconstrained sequential search for the contact point by fitting the force curve to a modified Hertz contact model, and selected the point that led to the best fit as the contact point.
- Lin *et al.* [29] used high-order derivatives to obtain a truncated dataset where linear elasticity theory was valid. Following this, a sequential search for the contact point was performed by fitting all the points to the right of the candidate contact point. The datapoint that led to the best fit was chosen as the contact point. Crick and Yin [45] used a secant method to truncate the AFM force datasets to ensure applicability of linear elasticity theory, following which a fitting protocol similar to [29]

was used to estimate the contact location.

- *Advantages:* These methods, when used on smoothed datasets, are independent of noise in the deflection data.
  - *Disadvantages:* Fitting (truncated) datasets to pre-established contact models makes implicit assumptions on the nature of material being indented. In many cases, the contact model is not beforehand.
- Purely fit-based Approaches
    - Costa *et al.* [1] used a bi-domain polynomial (BDP) fit (linear pre-contact and Hertzian contact regime) for the whole dataset. The estimated contact point was the point that resulted in the best fit for both regimes.
    - Polyakov *et al.* [46] performed segmentation of the AFM force curve into electrostatic and contact regions using a least-squares optimization approach.
    - *Advantages:* These methods do not require truncation of the datasets, which is often a subjective exercise. Also, absence of derivative computations eliminates the need of smoothing the raw datasets.
    - *Disadvantages:* Fitting datasets to pre-established contact models makes implicit assumptions on the nature of material being indented. In many cases, the contact model is not beforehand.

Research has also been directed towards developing methods that obviate the need to accurately determine the contact point. Al-Hassan *et al.* [47] developed an

approach termed as Force Integration to Equal Limits (FIEL) to obtain qualitative maps of relative elasticity in a biological sample. Briefly, the FIEL approach involves integrating the raw AFM force curves to the same limits (i.e. maximum deflection). The authors reported that varying the contact point by a few datapoints resulted in very small changes in the computed integral. The stiffness at different spatial locations was then expressed as a non-dimensional parameter, normalized by the integral at a given spatial location.

A relatively new approach to estimate the contact point was recently proposed by Rudoy *et al.* [48], which involves a Bayesian Change point model to obtain posterior distributions of the contact point along with the elastic modulus. As opposed to the other approaches stated before which are primarily point-based, a Bayesian formulation generates distributions that makes it possible to investigate the variability in the elastic modulus caused due to the contact uncertainty. The Bayesian formulation proposed in [48] can be looked upon as a probabilistic extension to the bi-domain polynomial (BDP) fitting approach proposed by Costa *et al.* in [1], which is a maximum-likelihood based approach to estimate the contact point.

#### 4.2.2 Uncertainty in AFM Probe Calibration

As stated previously in chapter 2, the deflection data,  $d$ , is related to the elastic modulus using the Hertz model as shown below:

$$F = k_c(d_n - d_k) = \frac{4E\sqrt{R}}{3(1 - \nu^2)}\Delta^{1.5} \quad (4.1)$$

where  $k$  is the contact point index in a dataset of  $n$  datapoints,  $k_c$  is the AFM spring constant,  $E$  is the elastic modulus and  $\nu$  is the Poisson's ratio of the material being indented. Since the elastic modulus  $E$  scales with the spring constant  $k_c$ , any uncertainty in  $k_c$  leads to a proportional change in  $E$ .

Due to potential inaccuracies during microfabrication, AFM probes are typically calibrated prior to their use. Various calibration methods have been proposed by researchers. Some of the most prominent ones are:

1. *Sader's Method* [27]: This method uses the probe dimensions, fundamental resonance frequency and the quality factor of the noise spectrum of a cantilever vibrating due to the thermal energy of the surroundings to calibrate the spring constant of the probe.
2. *Thermal Method* [25]: Similar to Sader's Method, the thermal method utilizes equipartition theorem to estimate the probe spring constant of a cantilever vibrating due to the thermal energy of the surroundings.
3. *Cleveland Method* [49]: The Cleveland method determines the probe spring constant from the decrease in resonant frequency resulting from the attachment of known masses to the probe.
4. *Reference cantilever based methods* [50]: This method involves deforming a probe of unknown spring constant against a known (reference) probe, and then measuring the deformations to estimate the spring constant of the unknown probe.



Of the aforementioned calibration protocols, the first three are most commonly used to estimate the spring constant. Of these, the thermal method [25] has emerged as a preferred choice of many researchers over (a) the Sader method [27] because it requires no prior knowledge of accurate dimensions of the probe and (b) the Cleveland method [49] because of its relative ease of use, as opposed to the cumbersome procedure of mounting masses on AFM probes [49]. Consequently, the thermal method is used to calibrate the AFM probe spring constant using Asylum Research software (IGOR Pro, Wavemetrics, Inc.)

The thermal method involves determination of (1) the sensitivity of the photodiode, commercially called Inverse Optical Lever Sensitivity (InvOLS) [nm/v] and (2) fundamental resonant frequency of the probe. Following is a step-by-step process to obtain the spring constant:

- An AFM force curve is obtained on a tissue-free hard glass surface of the microscope slide [Fig 4.2(a)].
- The slope of the approach force curve is computed.
- The InvOLS is computed from the slope of the force curve, after incorporating correction factors that accounts for the approximation of AFM probes as ideal springs and finite laser spot size on the probe end [51].
- The probe is withdrawn from the surface of the microscope slide and is made to vibrate in response to the thermal noise in the fluid surroundings.
- A Lorentzian function is then fitted to the thermal spectrum after visually

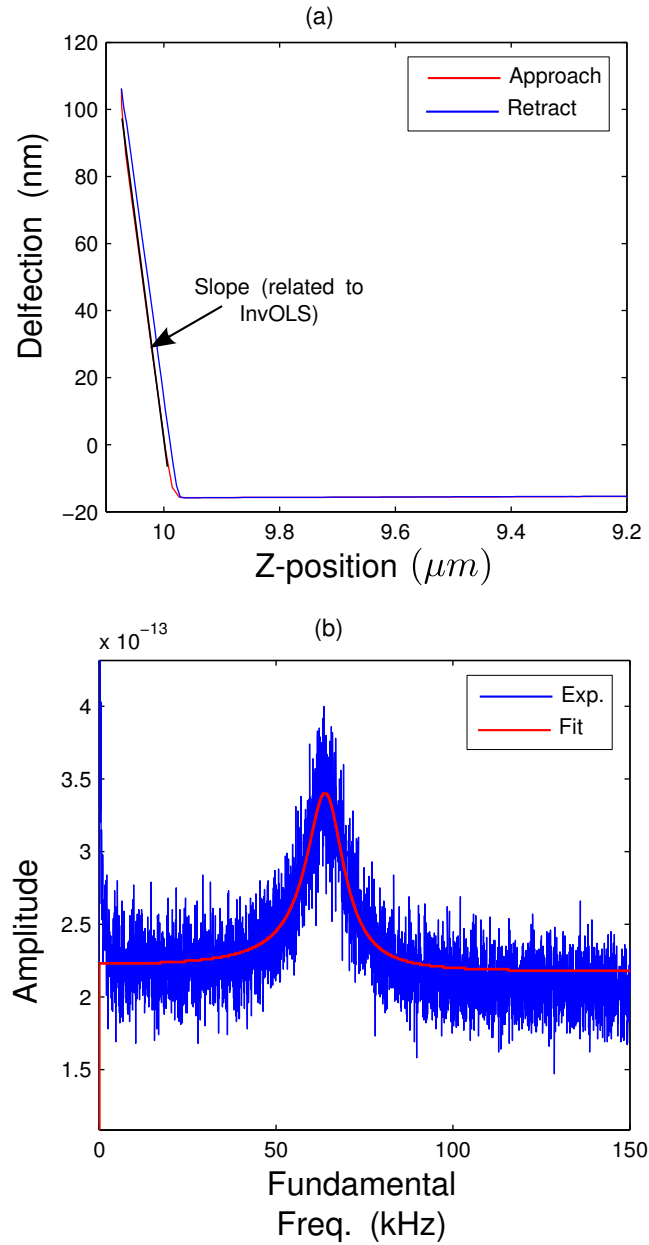


Figure 4.2: AFM Probe Calibration using the thermal method. (a) An AFM force curve on a tissue-free hard glass surface and (b) thermal spectrum of the probe in PBS solution. The rectangular probe of Table 4.2 (rated compliance of 0.222 m/N) was used to generate these results ©2014 IEEE.

locating the position of the fundamental frequency [Fig 4.2(b)]. The integral of the Lorentzian,  $P$ , is then computed.

- The spring constant is finally computed as:

$$k_c = \frac{k_B T}{P(InvOLS)^2} \quad (4.2)$$

While the calibration protocol discussed is fairly straightforward, interpreting the calibration results is a challenging exercise. Most calibration schemes report variability between 5-17% [52]. Carrying out calibration experiments in liquid environments add to further complexity in accurate determination of the probe's spring constant. Calibrated spring constants have shown large variations depending on the viscosity of the liquid medium. Pirzer and Hugel [53] reported an error of 25% in 4M phosphate solutions and upto 100% in highly viscous solutions. It was observed that improving the thermal spectrum fitting function to estimate the spring constants led to reduced errors in the calibrated stiffnesses.

A relatively new technique of AFM probe calibration is the use of laser doppler vibrometry (LDV) based interferometric methods [54] to measure the actual vertical displacement of the probe tip, as opposed to the optical detection methods used in standard AFMs that measure the angular deflection of the tip end. LDV-integrated AFMs have recently gained a lot of popularity for dynamic AFM methods in liquids [55]. Gates et al [28] recently reported calibration errors within 2%, compared to around 5% at best for the thermal method of calibrating AFM probes; however,

Table 4.2: Summary of AFM probe calibration results using the thermal method. Results expressed as mean  $\pm$  standard deviation.

Probe Geometry	Rated Compliance (m/N)	InvOLS (nm/V)	Fundamental Freq. (kHz)	Calibrated Compliance (m/N)
V-Shaped (Probe 1)	16.67	$87.72 \pm 3.66$	$3.77 \pm 0.13$	$16.38 \pm 1.63$
Rectangular (Probe 2)	0.222	$178.36 \pm 1.88$	$62.68 \pm 2.75$	$0.328 \pm 0.032$

LDV-integrated AFMs have yet to be commercialized, and the thermal method is used for calibrating the AFM probes in this dissertation.

It is worth mentioning here that henceforth, **the probe spring constant is referred to by its inverse, i.e. probe compliance**,  $s = 1/k_c$ . Such a transformation is a necessary step for expressing the uncertainty in the AFM probe calibrations as an error-in-variables (EIV) regression problem, as seen later in this chapter.

A summary of 20 calibration experiments using the thermal method for two probes in PBS solution prior to and after the completion of the AFM experiment are shown in Table 4.2. As seen from the thermal noise spectrum in [Fig 4.2(b)], the location of the fundamental frequency is not sharp due to the low Q-factor of the surrounding fluid. As a result, proper fitting of the noise spectrum to a Lorentzian is challenging. From Table 4.2, it can be observed that the probe compliance shows 10% errors, which are in good agreement with previously reported variability with the thermal method [52].

The aforementioned factors of uncertainty clearly pose a serious hindrance in obtaining accurate estimates of the mechanical properties of specimens subject to

AFM indentation. This need is further underscored in light of fact that mechanical characterization results on biomaterials such as breast tissue specimens are quite often followed by statistical hypothesis testing for inference purposes, for example, t-tests [10]. Pointwise estimation of the mechanical properties without accounting for the underlying uncertainty can lead to erroneous conclusions, especially when the computed p-values for the chosen hypothesis test are close to the level of significance,  $\alpha$ . Indeed, hypothesis testing methods that incorporate interval uncertainty [56] reduce the possibility of inference errors compared to conventional hypothesis testing techniques which assume that the exact values of the estimates are known. An accurate inference test, however, has to be preceded by an approach that quantifies the elastic modulus with its associated interval uncertainty in a robust manner [57].

Error quantification in AFM studies has been recently shown by [58], where studies were conducted in air to measure the elastic modulus of relatively stiff substrates like cellulose nanocrystals. However, the effect of contact uncertainty was not investigated, which is considerably lesser in air compared to liquid.

**Hypothesis:** Accuracy of the estimated elastic modulus can be significantly improved by developing robust uncertainty quantification techniques using Bayesian methods.

In this chapter, a rigorous statistical approach using an integrated error-in-variables (EIV) based Bayesian Changepoint formulation is proposed to estimate the elastic modulus of biological samples as a function of both the contact point and the AFM probe compliance variability. The probe compliance variability is modeled using the EIV formulation, which is typically used in cases where the in-

dependent variables in a regression model are observed with errors. Use of Markov Chain Monte Carlo (MCMC) methods makes it possible to factorize the joint posterior distribution and obtain samples from the marginal posterior distributions. The proposed algorithm is validated on simulated data and implemented on AFM datasets obtained from indentation studies on breast tissue specimens. Finally, a sensitivity analysis is carried out to monitor the performance of the algorithm to a wide range of probe compliance values.

### 4.3 Bayesian Analysis

#### 4.3.1 Transformation of raw data

The AFM raw data comprises the probe deflection ( $d$ ) and z-position ( $z$ ), which are processed offline to estimate the properties of the specimen being studied. Using the same notation used in section 2.2.3 of chapter 2, the contact point is given as  $(z_k, d_k)$ , where  $k \in (1, n)$  is the unknown index in the dataset which indicates the transition from non-contact to the contact regime.

The following transformation is used:

$$\delta_i = z_i - d_i \tag{4.3}$$

Physically,  $\delta$  represents the tip-sample distance prior to contact and the specimen indentation post-contact. Using Eqn. (2.1), the indentation in the sample can

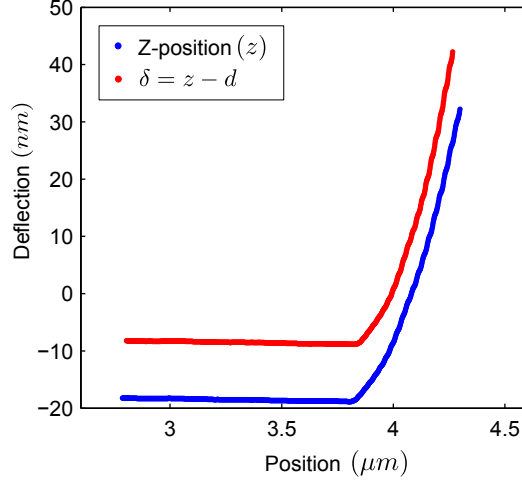


Figure 4.3: Representative AFM force curve of  $d$  v/s  $z$  and  $d$  v/s  $\delta$ . Please note that the  $d$  v/s  $\delta$  curve is displaced 10nm on the deflection axis for ease of visualization ©2014 IEEE.

be written as:

$$\Delta = \delta_n - \delta_k \quad (4.4)$$

The experimental data can now be related to an explicit force-indentation relationship by the following expression:

$$k_c(d_i - d_k) = \mathbf{f}(E, \nu, \delta_i - \delta_k) \quad (4.5)$$

where  $k_c$  is the probe spring constant,  $k + 1 \leq i \leq n$ ,  $\mathbf{f}(E, \nu, \delta_i - \delta_k)$  is the contact model,  $E$  is the elastic modulus and  $\nu$  is the Poisson's ratio.

Two contact models are used in the EIV-Bayesian Changepoint analysis and are given as follows:

1. Hertz contact model [26], as discussed in chapter 2.

2. Long's contact model [59], for finite indentations on a thin hyperelastic specimen following a neo-Hookean constitutive material model.

Assuming incompressibility in the biological specimens,  $\nu$  can be set to 0.5. Both Hertz and Long's contact models are linear in the elastic modulus,  $E$ , and can be written as:

$$k_c(d_i - d_k) = \frac{16E\sqrt{R}}{9}f_i \quad (4.6)$$

where

$$f_i = \begin{cases} (\delta_i - \delta_k)^{1.5} & \text{for } \mathbf{f} \equiv \text{Hertz} \\ \left[ (\delta_i - \delta_k)^{1.5} + 1.15\sqrt{\gamma}(\delta_i - \delta_k)^2 + \alpha_1\gamma\sqrt{\gamma}(\delta_i - \delta_k)^3 \right. \\ \quad \left. + \alpha_2\gamma^3(\delta_i - \delta_k)^{4.5} \right] / \left[ 1 + 2.3\gamma\sqrt{\gamma}(\delta_i - \delta_k)^{1.5} \right] & \text{for } \mathbf{f} \equiv \text{Long's Model} \end{cases} \quad (4.7)$$

The constants  $\alpha_1, \alpha_2$  and  $\gamma$  are given by:

$$\alpha_1 = 10.05 - 0.63\sqrt{h/R}(3.10 + h^2/R^2) \quad (4.8a)$$

$$\alpha_2 = 4.80 - 4.23h^2/R^2 \quad (4.8b)$$

$$\gamma = R/h^2 \quad (4.8c)$$

where  $k + 1 \leq i \leq n$ .  $R$  is the radius of the spherical bead ( $= 2.5 \mu m$ ) and  $h$  is the thickness of the tissue sample. Long's force-indentation relationship is valid in the regime  $\Delta/h \leq \min(0.6, R/h)$  and  $0.3 \leq R/h \leq 12.7$ . The expressions in Eqns. (4.8a) and (4.8b) assume frictionless contact between the AFM probe and the



specimen, which is a reasonable assumption since the tissue specimens are hydrated by PBS solution during the AFM experiments.

While using the Hertz model to study cells of radius  $R_{cell}$ ,  $R$  refers to the effective radius, given by:

$$R = \sqrt{\frac{R_{bead}R_{cell}}{R_{bead} + R_{cell}}} \quad (4.9)$$

An alternate form of Eqn. (4.6) is obtained by using the compliance of the probe,  $s = 1/k_c$ , in the right-hand-side of the Eqn. (4.6). Therefore, one can write:

$$(d_i - d_k) = \frac{16E\sqrt{R}}{9}sf_i \quad (4.10)$$

Such a transformation allows us to relate the deflection,  $d$ , to the transformed variable  $\delta$ , and to incorporate the probe compliance,  $s$ , into the EIV model, as shown later in this section.

In the non-contact regime, the deflection,  $d$ , can be modeled as a linear function of  $z$  [1], i.e.  $d = az + b$ , where  $a$  and  $b$  are arbitrary constants. However, using a simple rearrangement of the coefficients  $a$  and  $b$ , it can be readily shown that  $d$  also varies linearly with the transformed variable  $\delta$  in the non-contact regime:

$$d = \frac{a}{1-a}\delta + \frac{b}{1-a} \quad (4.11)$$

The two regime regression model relating the deflection  $d$  to  $\delta$  can therefore

be written as:

$$d_i = \begin{cases} \begin{bmatrix} 1 & \delta_i \end{bmatrix} \boldsymbol{\beta}_1 + \epsilon_1 & \text{if } i \leq k \\ \begin{bmatrix} 1 & sf_i \end{bmatrix} \boldsymbol{\beta}_2 + \epsilon_2 & \text{if } k+1 \leq i \leq n \end{cases} \quad (4.12)$$

where  $\epsilon_j \sim N(0, \sigma_j^2)$ ;  $j = 1, 2$  are independent and identically distributed (i.i.d) normal random variables and  $f_i$  is given by Eqn. (4.7). In general,  $\sigma_1^2 \neq \sigma_2^2$ , since  $\sigma_1^2$  results from the viscous interactions between the probe and the liquid medium, while  $\sigma_2^2$  depends primarily on the probe-sample frictional forces [48].  $\boldsymbol{\beta}_j = \begin{bmatrix} \beta_{j1} & \beta_{j2} \end{bmatrix}^T$ ;  $j = 1, 2$  are the regression coefficients in the non-contact and contact regime respectively, and  $\beta_{22}$  encapsulates the elastic modulus  $E$ .

### 4.3.2 Classical Error-In-Variables Model

In a standard linear regression model with a single independent covariate  $\xi$ , the data comprises  $n$  observations of the response variable  $y$  and  $\xi$ . These are related by the **data error model**, and is given by:

$$y_i = \beta_0 + \beta_1 \xi_i + \epsilon_i \quad ; \quad i = 1, 2, 3, \dots, n. \quad (4.13)$$

where the errors  $\epsilon_i$  are (i.i.d) and normally distributed with zero mean and constant variance  $\sigma_\epsilon^2$ , and  $\beta_0$  and  $\beta_1$  are unknown regression coefficients which are usually estimated using least-squares or other similar techniques.

The likelihood function in this case is given by the joint probability of the

data:

$$p(y_1, \dots, y_n | \beta_0, \beta_1, \sigma_\epsilon^2) \propto \left[ \frac{1}{\sigma_\epsilon^2} \right]^{\frac{n}{2}} \prod_{i=1}^n e^{\left[ -\frac{1}{2\sigma_\epsilon^2} (y_i - \beta_0 - \beta_1 \xi_i)^2 \right]} \quad (4.14)$$

However, there arises cases where the  $\xi_i$ 's are not directly observed. Instead,  $x_i$ 's are observed with a normally distributed additive error  $\nu_i$ , which are related by:

$$x_i = \xi_i + \nu_i \quad ; \quad i = 1, 2, 3, \dots, n. \quad (4.15)$$

The Equation (4.15) constitutes the **classical Error-In-Variable model**. Cheng and Ness [60] states three different sub-classifications of the classical EIV model based on the assumptions on  $\xi_i$ 's. These are given as follows:

1. *Functional Model*:  $\xi_i$ 's are assumed unknown constants.
2. *Structural Model*:  $\xi_i$ 's are (i.i.d) random variables and independent of the error  $\nu_i$ 's. In this case,

$$E(\xi_i) = \kappa; \quad var(\xi_i) = \sigma_\xi^2 \quad (4.16)$$

3. *Ultrastructural Model*: Similar to the structural model,  $\xi_i$ 's are independent random variables, but not identically distributed. This means that they have possibly dissimilar means,  $\kappa_i$ 's, and a common variance  $\sigma_\xi^2$ . If  $\kappa_1 = \kappa_2 = \dots \kappa_n$ , the ultrastructural model reduces to the structural one, whereas if  $\sigma_\xi^2 = 0$ , the ultrastructural model reduces to the functional model.

For considerations of simplicity the functional model is used for the rest of this work. To use the data error model together with the EIV model, certain assumptions are made about the errors  $\epsilon_i$  and  $\nu_i$  in Eqns. (4.13) and (4.15) respectively. These are:

$$E(\nu_i) = E(\epsilon_i) = 0 \quad (4.17a)$$

$$var(\nu_i) = \sigma_\nu^2, var(\epsilon_i) = \sigma_\epsilon^2 \quad \forall i \quad (4.17b)$$

$$cov(\nu_i, \nu_j) = cov(\epsilon_i, \epsilon_j) = 0 \quad \forall i \neq j \quad (4.17c)$$

$$cov(\nu_i, \epsilon_j) = 0 \quad \forall i, j. \quad (4.17d)$$

The likelihood function is now the joint distribution of the  $x_i$ 's from Eqn. (4.15) and the response variables  $y_i$ 's from Eqn. (4.13), and is given by:

$$\begin{aligned} p(x_1, \dots, x_n, y_1, \dots, y_n | \beta_0, \beta_1, \sigma_\epsilon^2, \sigma_\nu^2, \xi_1, \dots, \xi_n) &\propto \prod_{i=1}^n \left[ \frac{1}{\sigma_\nu^2} \right]^{\frac{1}{2}} e^{\left[ -\frac{1}{2\sigma_\nu^2} (x_i - \xi_i)^2 \right]} \\ &\times \prod_{i=1}^n \left[ \frac{1}{\sigma_\epsilon^2} \right]^{\frac{1}{2}} e^{\left[ -\frac{1}{2\sigma_\epsilon^2} (y_i - \beta_0 - \beta_1 \xi_i)^2 \right]} \end{aligned} \quad (4.18)$$

### 4.3.3 EIV-based Changepoint Modeling: Likelihood

From Eqn. (4.12), it can be seen that in the non-contact regime, the covariates  $\xi_i = \delta_i$ ,  $i = 1, 2, \dots, k$  are fixed and observed; therefore implementation of the EIV model is not necessary.

The joint distribution in the non-contact regime is therefore given as:

$$p(d_1, \dots, d_k | \beta_1, \sigma_1^2, k) \propto \prod_{i=1}^k \left[ \frac{1}{\sigma_1^2} \right]^{\frac{1}{2}} e^{\left[ -\frac{1}{2\sigma_1^2} (d_i - \beta_{11} - \beta_{12}\delta_i)^2 \right]} \quad (4.19)$$

where the response variables are the deflection data  $d_1, \dots, d_k$ .

In the contact regime, it one can write, using Eqn. (4.12):

$$\begin{aligned} \xi_{k+1} &= sf_{k+1} \\ &\vdots \\ \xi_n &= sf_n \end{aligned} \quad (4.20)$$

The covariates  $\xi_{k+1}, \dots, \xi_n$  in Eqn. (4.20) are multiples of the probe compliance  $s$ . When  $s$  is observed without errors, the estimation approach proposed in this work reduces to the regular Bayesian Changepoint model [48],[61], since  $\xi_1, \dots, \xi_n$  are fixed and observed. However, variations in the probe calibration measurements as evidenced by the results in Table 4.2 indicate that incorporation of some notion of randomness on the nature of  $s$  is necessary.

The variable  $s$  is modeled as an *unobserved variable* which needs to be estimated. Instead of observing  $s$ , the random variable  $s_d$  is observed with an additive Gaussian error  $\psi \sim N(0, \sigma_{s_d}^2)$ , which is given by:

$$s_d = s + \psi; \quad \psi \sim N(0, \sigma_{s_d}^2) \quad (4.21)$$

Using the observed probe compliance  $s_d$ , one can write:

$$\begin{aligned} x_{k+1} &= s_d f_{k+1} \\ &\vdots \\ x_n &= s_d f_n \end{aligned} \tag{4.22}$$

where  $x_{k+1}, \dots, x_n$  are the observed covariates analogous to the observed  $x_i$ 's in Eqn. (4.15).

At this point, it would seem natural to define a joint distribution of the data  $(x_i, d_i)$  similar to Eqn. (4.18). However, from Eqn. (4.22) it is clear that  $x_{k+1}, \dots, x_n$  are not independent; instead, they are multiples of  $s_d$ . Likewise, the unobserved  $\xi_{k+1}, \dots, \xi_n$  are all multiples of  $s$ . Moreover, it is important to note that the independence condition from Eqn. (4.17c) is violated, since:

$$\begin{aligned} cov(\nu_i, \nu_j) &= cov(x_i, x_j) = f_i f_j cov(s_d, s_d) \\ &\neq 0 \quad \forall \quad i \neq j \end{aligned} \tag{4.23}$$

The direct implication of the violation of the independence condition of Eqn. (4.17c) is that the covariate distribution can simply be expressed in  $s_d$  and  $s$ , instead of the covariates  $x_{k+1}, \dots, x_n$  and  $\xi_{k+1}, \dots, \xi_n$ . **The EIV model in the contact regime therefore can be reduced to:**

$$\boxed{p(s_d | s, \sigma_{s_d}^2) \propto \left[ \frac{1}{\sigma_{s_d}^2} \right]^{\frac{1}{2}} e^{\left[ \frac{-(s_d - s)^2}{2\sigma_{s_d}^2} \right]}} \tag{4.24}$$

This leads to considerable reduction in the complexity of the joint distribution of the contact-regime data. The joint distribution of the EIV model and the deflection data in the contact regime now can be written as:

$$\begin{aligned}
p(s_d, d_{k+1}, \dots, d_n | \beta_2, \sigma_2^2, k, s) &= p(s_d) \prod_{i=k+1}^n p(d_i) \\
&\propto \left[ \frac{1}{\sigma_{s_d}^2} \right]^{\frac{1}{2}} e^{\left[ \frac{-(s_d - s)^2}{2\sigma_{s_d}^2} \right]} \prod_{i=k+1}^n \left[ \frac{1}{\sigma_2^2} \right]^{\frac{1}{2}} e^{\left[ -\frac{1}{2\sigma_2^2} (d_i - \beta_{21} - s\beta_{22}f_i)^2 \right]}
\end{aligned} \tag{4.25}$$

Combining the joint distribution in the non-contact regime [Eqn. (4.19)] with the distribution of  $s_d$  in the contact regime [Eqn (4.25)], the data likelihood for the whole dataset is given by:

$$\begin{aligned}
p(s_d, d_1, d_2, \dots, d_n | \beta_1, \beta_2, \sigma_1^2, \sigma_2^2, k, s) &= p(s_d) \prod_{i=1}^n p(d_i) \\
&\propto \left[ \frac{1}{\sigma_{s_d}^2} \right]^{\frac{1}{2}} e^{\left[ \frac{-(s_d - s)^2}{2\sigma_{s_d}^2} \right]} \prod_{i=1}^k \left[ \frac{1}{\sigma_1^2} \right]^{\frac{1}{2}} e^{\left[ -\frac{1}{2\sigma_1^2} (d_i - \beta_{11} - \beta_{12}\delta_i)^2 \right]} \prod_{i=k+1}^n \left[ \frac{1}{\sigma_2^2} \right]^{\frac{1}{2}} e^{\left[ -\frac{1}{2\sigma_2^2} (d_i - \beta_{21} - s\beta_{22}f_i)^2 \right]}
\end{aligned} \tag{4.26}$$

Based on the candidate contact point  $k$ , the deflection data can be re-written in a compact vector form, as,  $\mathbf{d}_1 = [d_1 \quad d_2 \quad \dots \quad d_k]^T$ ,  $\mathbf{d}_2 = [d_{k+1} \quad d_{k+2} \quad \dots \quad d_n]^T$  and  $\mathbf{d} = [\mathbf{d}_1 \quad \mathbf{d}_2]$ . The right hand side of [Eqn. (4.12)] form the design matrices given by:

$$\mathbf{X}_1 = \begin{bmatrix} 1 & 1 & \dots & 1 \\ \delta_1 & \delta_2 & \dots & \delta_k \end{bmatrix}^T$$

$$\mathbf{X}_2 = \begin{bmatrix} 1 & 1 & \dots & 1 \\ sf_{k+1} & sf_{k+2} & \dots & sf_n \end{bmatrix}^T \quad (4.27)$$

Using the notations in Eqn. (4.27), the data likelihood of  $(s_d, \mathbf{d})$  can be re-written as:

$$p(s_d, \mathbf{d} | \boldsymbol{\beta}_1, \boldsymbol{\beta}_2, \sigma_1^2, \sigma_2^2, k, s) \propto \left[ \frac{1}{\sigma_{s_d}^2} \right]^{\frac{1}{2}} e^{\left[ -\frac{1}{2\sigma_{s_d}^2} (s_d - s)^2 \right]} \times \left[ \frac{1}{\sigma_1^2} \right]^{\frac{k}{2}} e^{\left[ -\frac{1}{2\sigma_1^2} \|\mathbf{d}_1 - \mathbf{X}_1 \boldsymbol{\beta}_1\|^2 \right]} \times \left[ \frac{1}{\sigma_2^2} \right]^{\frac{n-k}{2}} e^{\left[ -\frac{1}{2\sigma_2^2} \|\mathbf{d}_2 - \mathbf{X}_2 \boldsymbol{\beta}_2\|^2 \right]} \quad (4.28)$$

#### 4.3.4 EIV-based Changepoint Modeling: Posterior

Table 4.3: Conjugate Prior Distributions

Model Parameter	Distribution Family	Hyperparameters
$k$	Uniform	$\sim U(1, n)$
$\boldsymbol{\beta}_1, \boldsymbol{\beta}_2$	Normal	$\sim N(\bar{\boldsymbol{\beta}}_1, \bar{\boldsymbol{\Lambda}}_1^{-1})$ , $\sim N(\bar{\boldsymbol{\beta}}_2, \bar{\boldsymbol{\Lambda}}_2^{-1})$
$\sigma_1^2, \sigma_2^2$	Inverse Gamma	$\sim IG(a_0, b_0)$ , $\sim IG(a_0, b_0)$
$s$	Normal	$\sim N(\mu_{s_p}, \sigma_{s_p}^2)$

The posterior distribution, expressed as *posterior distribution*  $\propto$  *data likelihood*  $\times$  *prior distribution*, and can be written as:

$$p(\boldsymbol{\beta}_1, \boldsymbol{\beta}_2, \sigma_1^2, \sigma_2^2, k, s | s_d, \mathbf{d}, \sigma_{s_d}^2) \propto p(\mathbf{d}, s_d | \boldsymbol{\beta}_1, \boldsymbol{\beta}_2, \sigma_1^2, \sigma_2^2, k, s) \times \pi(\boldsymbol{\beta}_1) \times \pi(\boldsymbol{\beta}_2) \times \pi(\sigma_1^2) \times \pi(\sigma_2^2) \times \pi(k) \times \pi(s) \quad (4.29)$$

where  $\pi(\cdot)$  indicates the prior distribution of the variable in parenthesis. Conjugate



priors (Table 4.3) are used to ensure that the posterior distribution is separable [61].

Combining the distribution of the data with the priors, the posterior can be written

as:

$$\begin{aligned}
p(\boldsymbol{\beta}_1, \boldsymbol{\beta}_2, \sigma_1^2, \sigma_2^2, k, s | s_d, \mathbf{d}, \sigma_{s_d}^2) &\propto \left[ \frac{1}{\sigma_1^2} \right]^{\frac{k}{2}} \left[ \frac{1}{\sigma_2^2} \right]^{\frac{n-k}{2}} \left[ \frac{1}{\sigma_{s_d}^2} \right]^{\frac{1}{2}} e^{\left[ -\frac{1}{2\sigma_1^2} \|\mathbf{d}_1 - \mathbf{X}_1 \boldsymbol{\beta}_1\|^2 \right]} e^{\left[ -\frac{1}{2\sigma_2^2} \|\mathbf{d}_2 - \mathbf{X}_2 \boldsymbol{\beta}_2\|^2 \right]} \\
&\quad e^{\left[ -\frac{1}{2\sigma_{s_d}^2} (s_d - s)^2 \right]} e^{\left[ -\frac{1}{2} (\boldsymbol{\beta}_1 - \bar{\boldsymbol{\beta}}_1)^T \bar{\mathbf{\Lambda}}_1 (\boldsymbol{\beta}_1 - \bar{\boldsymbol{\beta}}_1) \right]} e^{\left[ -\frac{1}{2} (\boldsymbol{\beta}_2 - \bar{\boldsymbol{\beta}}_2)^T \bar{\mathbf{\Lambda}}_2 (\boldsymbol{\beta}_2 - \bar{\boldsymbol{\beta}}_2) \right]} \\
&\quad (\sigma_1^2)^{-a_0-1} e^{\left[ -\frac{b_0}{\sigma_1^2} \right]} (\sigma_2^2)^{-a_0-1} e^{\left[ -\frac{b_0}{\sigma_2^2} \right]} \left[ \frac{1}{\sigma_{s_p}^2} \right]^{\frac{1}{2}} e^{\left[ -\frac{1}{2\sigma_{s_p}^2} (s - \mu_{s_p})^2 \right]}
\end{aligned} \tag{4.30}$$

A schematic of the EIV-Bayesian Changepoint algorithm is given in Fig. 4.4.

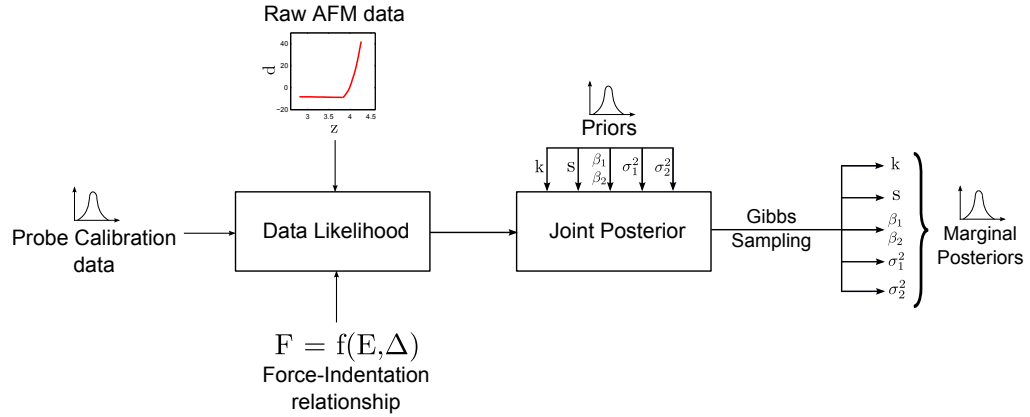


Figure 4.4: Schematic of the EIV-Bayesian Changepoint algorithm ©2014 IEEE.

#### 4.3.5 EIV-based Changepoint Modeling: Gibbs Sampling

The marginal posteriors are obtained from the joint posterior distribution of Eqn. (4.30) using Gibbs Sampling, which is a Markov Chain Monte Carlo (MCMC) sampling technique wherein the marginal posterior in each parameter of the joint

posterior is derived by separating out the terms in the joint posterior corresponding to each parameter and conditional upon the rest. The posterior is sampled iteratively for the parameters  $(s, \beta_1, \beta_2, \sigma_1^2, \sigma_s^2, k)$ .

While sampling for  $s^{(i+1)}$  given  $i$  previous iteratively sampled steps, it can be observed that  $s$  appears in the data likelihood and the prior for  $s$ . The terms in the posterior distribution containing  $s$  are given by:

$$\begin{aligned}
p(s) &\propto e^{\left[-\frac{1}{2\sigma_2^2}\|d_2 - X_2\beta_2\|^2\right]} e^{\left[-\frac{1}{2\sigma_{s_d}^2}(s_d - s)^2\right]} e^{\left[-\frac{1}{2\sigma_{s_p}^2}(s - \mu_{s_p})^2\right]} \\
&\propto e^{\left[-\frac{1}{2\sigma_2^2}\sum_{j=k+1}^n \{d_i - \beta_{21} - \beta_{22}s f_j\}^2\right]} e^{\left[-\frac{1}{2\sigma_{s_d}^2}(s_d - s)^2\right]} e^{\left[-\frac{1}{2\sigma_{s_p}^2}(s - \mu_{s_p})^2\right]} \quad (4.31a)
\end{aligned}$$

The coefficients of  $s^2$  and  $s$  can be combined to complete the square in  $s$  by a simple rearrangement of terms in Eqn. (4.31a). Since the constant term in the square in  $s$  is not dependent on  $s$ , it can be ignored without altering the Gibbs Sampling step. Therefore:

$$\begin{aligned}
s^{(i+1)} &\sim p(s|\beta_1^{(i)}, \beta_2^{(i)}, \sigma_1^{2(i)}, \sigma_2^{2(i)}, k^{(i)}) \\
&\sim N(\tilde{\mu}_s, \tilde{\sigma}_s^2)
\end{aligned}$$

where :

$$\tilde{\mu}_s = \left[ \left( \frac{\sigma_{s_p}^2 s_d + \sigma_{s_d}^2 \mu_{s_p}}{\sigma_{s_p}^2 + \sigma_{s_d}^2} \right) \frac{\sigma_2^2}{\beta_{22}^2 \sum_{j=k+1}^n f_j^2} + \left( \frac{\sum_{j=k+1}^n (d_j - \beta_{21}) f_j}{\beta_{22} \sum_{j=k+1}^n f_j^2} \right) \left( \frac{\sigma_{s_p}^2 \sigma_{s_d}^2}{\sigma_{s_p}^2 + \sigma_{s_d}^2} \right) \right] \left[ \frac{\sigma_2^2}{\beta_{22}^2 \sum_{j=k+1}^n f_j^2} + \left( \frac{\sigma_{s_p}^2 \sigma_{s_d}^2}{\sigma_{s_p}^2 + \sigma_{s_d}^2} \right) \right]^{-1} \quad (4.31b)$$

$$\tilde{\sigma}_s^2 = \left[ \frac{\beta_{22}^2}{\sigma_2^2} \sum_{j=k+1}^n f_j^2 + \frac{1}{\sigma_{s_d}^2} + \frac{1}{\sigma_{s_p}^2} \right]^{-1} \quad (4.31c)$$

Likewise, the regression parameters  $\beta_1$  and  $\beta_2$  appear in multivariate normal form in the data likelihood and the priors for  $\beta_1$  and  $\beta_2$  respectively, and the same strategy is employed to complete the square and factor it out of the posterior. The terms in the posterior distribution containing the regression parameters are given by:

$$\begin{aligned} p(\beta_m) &\propto e^{\left[ -\frac{1}{2\sigma_m^2} \|\mathbf{d}_m - \mathbf{X}_m \beta_m\|^2 \right]} e^{\left[ -\frac{1}{2} (\beta_m - \bar{\beta}_m)^T \bar{\Lambda}_m (\beta_m - \bar{\beta}_m) \right]} \\ &\propto e^{\left[ -\frac{1}{2\sigma_m^2} \{ \|\mathbf{d}_m - \mathbf{X}_m \hat{\beta}_m\|^2 + (\beta_m - \hat{\beta}_m)^T \mathbf{X}_m^T \mathbf{X}_m (\beta_m - \hat{\beta}_m) \} \right]} e^{\left[ -\frac{1}{2} (\beta_m - \bar{\beta}_m)^T \bar{\Lambda}_m (\beta_m - \bar{\beta}_m) \right]} \end{aligned} \quad (4.32a)$$

where  $m = 1, 2$  for the non-contact and the contact regimes respectively and  $\hat{\beta}_m = (\mathbf{X}_m^T \mathbf{X}_m)^{-1} \mathbf{X}_m^T \mathbf{d}_m$  is the least-squares solution.

The following identity is used to complete the square in the multivariate case

[62]:

$$\sum_{p=1}^2 (\boldsymbol{\alpha} - \boldsymbol{\alpha}_p)^T \boldsymbol{\Sigma}_p (\boldsymbol{\alpha} - \boldsymbol{\alpha}_p) = (\boldsymbol{\alpha} - \tilde{\boldsymbol{\alpha}})^T \boldsymbol{\Gamma} (\boldsymbol{\alpha} - \tilde{\boldsymbol{\alpha}}) + f(\boldsymbol{\alpha}_p, \boldsymbol{\Sigma}_p) \quad (4.32b)$$

where  $\boldsymbol{\Sigma}_1, \boldsymbol{\Sigma}_2$  are positive semi-definite symmetric matrices,  $\tilde{\boldsymbol{\alpha}} = (\boldsymbol{\Sigma}_1 + \boldsymbol{\Sigma}_2)^{-1}(\boldsymbol{\Sigma}_1 \boldsymbol{\alpha}_1 + \boldsymbol{\Sigma}_2 \boldsymbol{\alpha}_2)$  and  $\boldsymbol{\Gamma} = \boldsymbol{\Sigma}_1 + \boldsymbol{\Sigma}_2$ .

Using Eqn. (4.32b), one arrives at the following expression:

$$\begin{aligned} \boldsymbol{\beta}_1^{(i+1)} &\sim p(\boldsymbol{\beta}_1 | s^{(i+1)}, \boldsymbol{\beta}_2^{(i)}, \sigma_1^{2(i)}, \sigma_2^{2(i)}, k^{(i)}) \\ &\sim N(\tilde{\boldsymbol{\beta}}_1, \tilde{\boldsymbol{\Sigma}}_1) \end{aligned} \quad (4.32c)$$

$$\begin{aligned} \boldsymbol{\beta}_2^{(i+1)} &\sim p(\boldsymbol{\beta}_2 | s^{(i+1)}, \boldsymbol{\beta}_1^{(i+1)}, \sigma_1^{2(i)}, \sigma_2^{2(i)}, k^{(i)}) \\ &\sim N(\tilde{\boldsymbol{\beta}}_2, \tilde{\boldsymbol{\Sigma}}_2) \end{aligned} \quad (4.32d)$$

where

$$\tilde{\boldsymbol{\beta}}_m = (\sigma_m^{-2} \mathbf{X}_m^T \mathbf{X}_m + \bar{\boldsymbol{\Lambda}}_m)^{-1} (\sigma_m^{-2} \mathbf{X}_m^T \mathbf{d}_m + \bar{\boldsymbol{\Lambda}}_m \bar{\boldsymbol{\beta}}_m) \quad (4.32e)$$

$$\tilde{\boldsymbol{\Sigma}}_m = (\sigma_m^{-2} \mathbf{X}_m^T \mathbf{X}_m + \bar{\boldsymbol{\Lambda}}_m)^{-1} \quad (4.32f)$$

for  $m = 1, 2$ .

The variances  $\sigma_1^2$  and  $\sigma_2^2$  appear in the data likelihood and the priors for the variances. Likewise, the posterior can be factorized to contain terms only in  $\sigma_1^2$  and

$\sigma_2^2$  and the following expression results:

$$\begin{aligned}
p(\sigma_1^2) &\propto \left[ \frac{1}{\sigma_1^2} \right]^{\frac{k}{2}} e^{\left[ -\frac{1}{2\sigma_1^2} \|\mathbf{d}_1 - \mathbf{X}_1 \boldsymbol{\beta}_1\|^2 \right]} \left[ \frac{1}{\sigma_1^2} \right]^{a_0+1} e^{\left[ -\frac{b_0}{\sigma_1^2} \right]} \\
&\propto \left[ \frac{1}{\sigma_1^2} \right]^{\frac{k}{2}+a_0+1} e^{\left[ -\frac{1}{\sigma_1^2} \left( 0.5 \|\mathbf{d}_1 - \mathbf{X}_1 \boldsymbol{\beta}_m\|^2 + b_0 \right) \right]}
\end{aligned} \tag{4.33a}$$

and

$$\begin{aligned}
p(\sigma_2^2) &\propto \left[ \frac{1}{\sigma_2^2} \right]^{\frac{n-k}{2}} e^{\left[ -\frac{1}{2\sigma_2^2} \|\mathbf{d}_2 - \mathbf{X}_2 \boldsymbol{\beta}_2\|^2 \right]} \left[ \frac{1}{\sigma_2^2} \right]^{a_0+1} e^{\left[ -\frac{b_0}{\sigma_2^2} \right]} \\
&\propto \left[ \frac{1}{\sigma_2^2} \right]^{\frac{n-k}{2}+a_0+1} e^{\left[ -\frac{1}{\sigma_2^2} \left( 0.5 \|\mathbf{d}_2 - \mathbf{X}_2 \boldsymbol{\beta}_2\|^2 + b_0 \right) \right]}
\end{aligned} \tag{4.33b}$$

Hence, one can write:

$$\begin{aligned}
\sigma_1^{2,(i+1)} &\sim p(\sigma_1^2 | s^{(i+1)}, \boldsymbol{\beta}_1^{(i+1)}, \boldsymbol{\beta}_2^{(i+1)}, \sigma_2^{2(i)}, k^{(i)}) \\
&\sim IG(\tilde{a}_1, \tilde{b}_1)
\end{aligned} \tag{4.33c}$$

$$\begin{aligned}
\sigma_2^{2,(i+1)} &\sim p(\sigma_2^2 | s^{(i+1)}, \boldsymbol{\beta}_1^{(i+1)}, \boldsymbol{\beta}_2^{(i+1)}, \sigma_1^{2,(i+1)}, k^{(i)}) \\
&\sim IG(\tilde{a}_2, \tilde{b}_2)
\end{aligned} \tag{4.33d}$$

where

$$\tilde{a}_1 = a_0 + k/2 \tag{4.33e}$$

$$\tilde{a}_2 = a_0 + (n - k)/2 \tag{4.33f}$$

$$\tilde{b}_m = b_0 + 0.5(\|\mathbf{d}_m - \mathbf{X}_m \boldsymbol{\beta}_m\|)^2 \tag{4.33g}$$

for  $m = 1, 2$ .

In the case of the contact point index, a flat uninformative prior  $[\pi(k) = 1]$  is used to avoid biasing the posterior. The posterior in  $k$  is therefore the discrete distribution function obtained by varying  $k$  over the data likelihood, and is given by:

$$\begin{aligned} k^{(i+1)} &\propto p(k|s^{(i+1)}, \boldsymbol{\beta}_1^{(i+1)}, \boldsymbol{\beta}_2^{(i+1)}, \sigma_1^{2,(i+1)}, \sigma_2^{2,(i+1)}) \\ &\propto \left[ \frac{1}{\sigma_1^2} \right]^{\frac{k}{2}} e^{\left[ -\frac{1}{2\sigma_1^2} \|\mathbf{d}_1 - \mathbf{X}_1 \boldsymbol{\beta}_1\|^2 \right]} \left[ \frac{1}{\sigma_2^2} \right]^{\frac{n-k}{2}} e^{\left[ -\frac{1}{2\sigma_2^2} \|\mathbf{d}_2 - \mathbf{X}_2 \boldsymbol{\beta}_2\|^2 \right]} \end{aligned} \quad (4.34)$$

## 4.4 Results and Discussions

### 4.4.1 Implementation of the Gibbs Sampler

Excepting the contact point index  $k$ , all the other marginal posteriors can be directly sampled from their respective family of parametric probability distributions due to the use of conjugate priors. Rejection sampling [63] is used to sample for  $k$  [Eqn. (4.34)] to complete the Gibbs Sampling step.

The initial 3000 iteration results of the Gibbs Sampler are rejected, which constitutes the *burn-in* period. Sampling is terminated when increasing the number of iterations do not alter the nature of the marginal posteriors. Typically, sampling is terminated after 200,000 iterations. With respect to the probe compliance,  $s_d$  is set to a pre-experiment calibration value ( $= 16.1 \text{ m/N}$  for Probe 1 and  $0.339 \text{ m/N}$  for Probe 2). The hyperparameter values of the probe compliance are set to those obtained in Table 4.2, i.e.  $\mu_{s_p} = 16.38 \text{ m/N}$ ,  $\sigma_{s_p}^2 = 1.63^2 \text{ m}^2/\text{N}^2$  for Probe 1 and

Table 4.4: Hyperparameter Values

Hyperparameters	Values
$\bar{\beta}_1, \bar{\beta}_2$	$[0 \ 0]^T$
$\bar{\Lambda}_1, \bar{\Lambda}_2$	$\begin{bmatrix} 10^{-15} & 0 \\ 0 & 10^{-15} \end{bmatrix}$
$(a_0, b_0)$	(1, 2) (Hertz Model)
	(1, 0.002) (Long's Model)
$(\mu_{s_p}, \sigma_{s_p}^2)$	(16.38, 1.63 <sup>2</sup> ) (for Probe 1)
	(0.328, 0.032 <sup>2</sup> ) (for Probe 2)

$\mu_{s_p} = 0.328 \text{ m/N}$ ,  $\sigma_{s_p}^2 = 0.032^2 \text{ m}^2/\text{N}^2$  for Probe 2. Using such an informative prior based on Table 4.2 makes it possible to incorporate prior knowledge of multiple probe calibrations. The prior and data variances of the probe compliance are also assumed to be equal i.e.  $\sigma_{s_p}^2 = \sigma_{s_d}^2$ . This allows us to give equal weightage to the prior and data values. Setting the data and prior variances equal also avoids estimation problems, which are typical when the data variance is unknown [64]. With respect to the other parameters, no useful information is available beforehand, consequently, uninformative priors are assigned to them. The contact point  $k$  is assigned a uniform distribution,  $U(1, n)$ , while  $\beta_1, \beta_2, \sigma_1^2$  and  $\sigma_2^2$  are assigned disperse prior distributions. The hyperparameter values used during sampling is given in Table 4.4.

#### 4.4.2 Simulated Data

Owing to lack of robust experimental methods to determine the contact point from AFM force curves, the EIV-Bayesian Changepoint algorithm is first validated

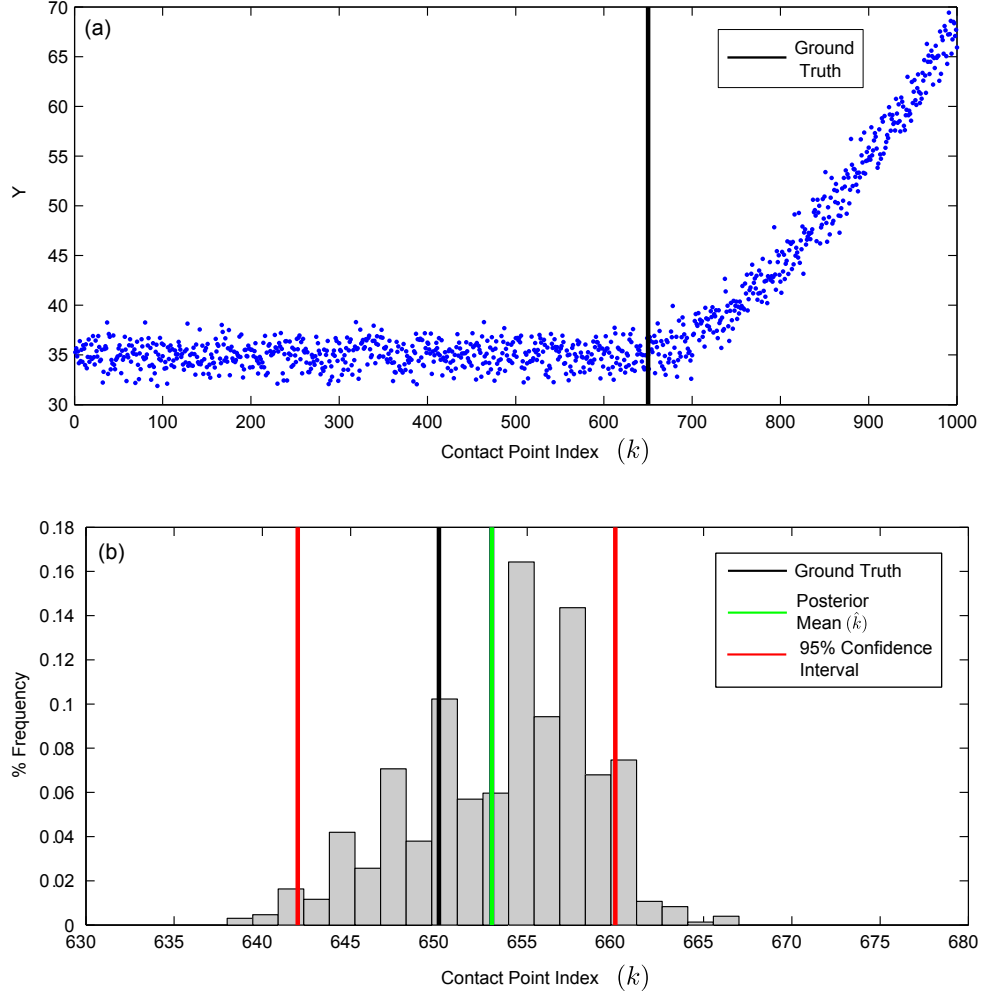


Figure 4.5: Results of the EIV-Bayesian Changepoint algorithm on simulated data with  $n = 1000$  datapoints. (a) Simulated AFM force curve with contact occurring at datapoint  $k = 650$  and (b) marginal posterior of the contact point index  $k$ , along with the posterior mean  $[\hat{k}] = 653$  and the 95% confidence intervals  $[642, 660]$ .



on a simulated AFM force curve with a known contact point. The Hertz model (with power law 1.5) is used as the force-indentation relationship, and the calibration results for Probe 1 are used to specify the probe compliance data and hyperparameter values. The following parameters were used to generate the entire data:

- Datapoints  $n = 1000$ . Contact Point Index  $k = 650$ .
- Pre-contact regime standard deviation  $\sigma_1 = 1.20$ . Contact regime standard deviation  $\sigma_2 = 1.50$ .
- Pre-contact regime regression parameters  $\beta_1 = [\beta_{11} \quad \beta_{12}]^T = [35 \quad 0.001]^T$ .
- Contact regime regression parameters  $\beta_2 = [\beta_{j1} \quad \beta_{j2}]^T = [35.01 \quad 0.3]^T$ .
- Observed probe compliance  $s_d = 16.10$ . Observed probe compliance variance  $\sigma_{s_d}^2 = 1.63^2$ .

The simulated AFM curve is shown in Fig. 4.5(a). The noise parameters  $\sigma_1$  and  $\sigma_2$ , were selected to mimic experimental AFM force curves obtained on extremely compliant live cells, where the contact uncertainty is more severe than other biological specimens.

The result of sampling the marginal posterior in the contact point index  $k$  according to Eqn. (4.34) is shown in Fig. 4.5(b). The true contact point is at datapoint 650, while the posterior mean of the contact point is given by  $[\hat{k}] = 653$ , a very negligible error given the noisy nature of the transition. Moreover, it is significant to note that the 95% confidence interval (C.I.) given by  $[642, 660]$ , contains the true contact point. This is one of the advantages of using an interval based

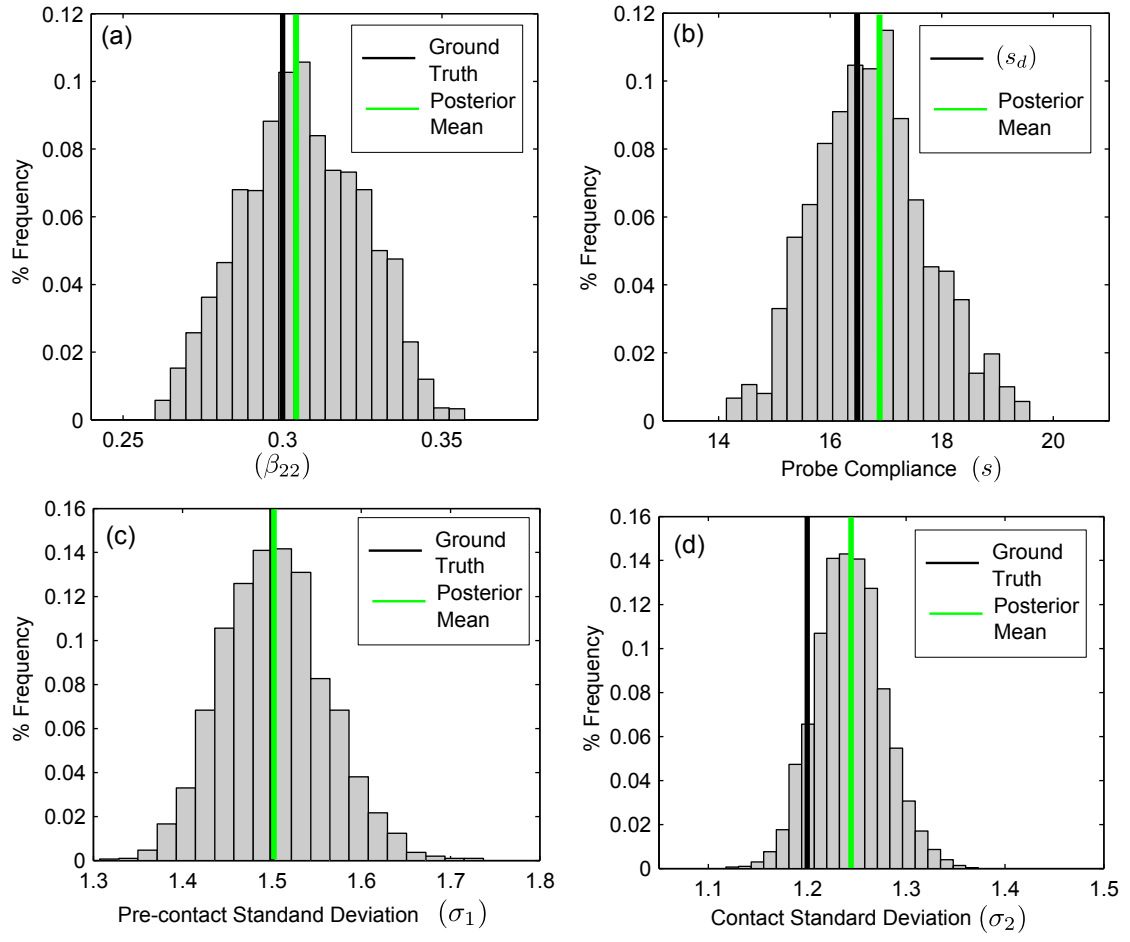


Figure 4.6: Marginal posterior distributions in (a)  $\beta_{22}$  (b)  $s$  (c)  $\sigma_1$  and (d)  $\sigma_2$ .

Table 4.5: Model performance on simulated data

	Ground Truth	Posterior Means
$k$	650	653
$\beta_{22}$	0.3	0.306
$\sigma_1$	1.20	1.24
$\sigma_2$	1.50	1.50
$(s_d, \mu_{s_p})$	(16.10, 16.38)	16.74 ( $\hat{s}$ )

method over point based methods in estimating the contact-point and the mechanical properties: even though the true contact point was missed by 3 datapoints, the 95% C.I contained the true contact point. It is also evident from Figs. 4.5(a) and 4.5(b) that integration of the EIV model into a standard Changepoint model does not adversely affect Changepoint model’s ability to estimate the contact point.

The marginal posteriors in  $s, \beta_{22}, \sigma_1^2, \sigma_2^2$  are given in Fig. 4.6, and the posterior means are given in Table 4.5. From the results, it can be seen that the EIV-Bayesian Changepoint model performs quite satisfactorily on simulated data. The estimation error in the regression coefficient of interest,  $\beta_{22}$  is 2%, which is quite reasonable given the noisy nature of the simulated AFM force curve. The posterior means of  $\sigma_1$  and  $\sigma_2$  are also within 3.5 % of the ground truth values. The probe compliance  $s$  shows a posterior mean ( $\hat{s} = 16.74$ ) with a dispersed distribution due to the variability introduced by the variance terms  $\sigma_{s_d}^2$  and  $\sigma_{s_p}^2$ .

#### 4.4.3 AFM studies on histological breast tissue

This section deals with the implementation of the algorithm on AFM indentation datasets obtained from histological breast tissue samples. The AFM indenta-

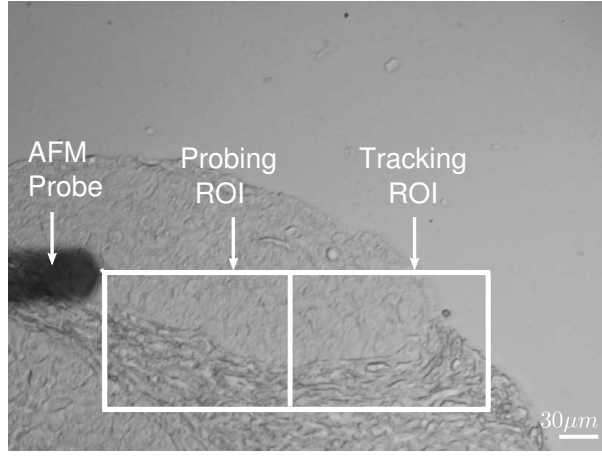


Figure 4.7: Image of tissue region where probing was conducted to obtain the results in this section. AFM indentation experiments on breast tissue were conducted in the probing ROI ©2014 IEEE.

tion data was generated from raster scanning of the probing ROI shown in Fig. 4.7. Probe 2 was used for the AFM experiments, and Long’s contact model [59] was used as force-indentation relationship.

Due to the absence of existing algorithms that quantify the elastic modulus estimation errors due to both contact uncertainty and probe calibration variability, it is difficult to compare the efficacy of the algorithm in reflecting the variability in the estimated elastic modulus due to these two sources of uncertainty. To overcome this, the following steps are implemented:

1. The 95% bounds from multiple calibration experiments in Table 4.2, i.e.  $\bar{s}_{2.5\%} = 0.328 - 2(0.032) \text{ m/N}$  and  $\bar{s}_{97.5\%} = 0.328 + 2(0.032) \text{ m/N}$  are used to set deterministic bounds of the probe compliance variability from the probe compliance.
2. The posterior mean of the contact point,  $\hat{k}$ , is obtained through a standard

Bayesian Changepoint approach [48] (without any variations in the probe compliance).

3. Using  $\bar{s}_{2.5\%}$  and  $\bar{s}_{97.5\%}$  and the contact point posterior mean from step (2), the bounds of the elastic modulus,  $\bar{E}_{2.5\%}$  and  $\bar{E}_{97.5\%}$ , are estimated using least-squares fitting to the Long's model. These bounds are then compared to the 95% confidence intervals of the marginal posterior in the elastic modulus obtained from the EIV-Bayesian Changepoint approach.

The results of the EIV-Bayesian Changepoint algorithm applied on a representative AFM force curve on tissue specimens are presented in Figs. 4.8 and 4.9. The AFM deflection data together with the posterior mean of the contact point ( $\lfloor \hat{k} \rfloor = 433$ ) is shown in Fig. 4.8(a), and the marginal posterior in  $k$  is shown in Fig. 4.8(b).

The marginal posterior in  $s$  is shown in Fig. 4.9(a). The marginal posterior in  $\beta_{22}$  [Fig. 4.9(b)] is easily transformed into the elastic modulus,  $E$ , due to the linear relationship between them [Eqn. (4.10)]. The posterior mean of the elastic modulus,  $\hat{E} = 119.01$  kPa compares favorably with previously reported values on histological breast tissue [65].

Also displayed in the Figs. 4.9(a) and (b) are the bounds ( $\bar{s}_{2.5\%}, \bar{s}_{97.5\%}$ ) and ( $\bar{E}_{2.5\%}, \bar{E}_{97.5\%}$ ) respectively. It is evident that the 95% confidence intervals of the elastic modulus are well bounded by  $\bar{E}_{2.5\%}$  and  $\bar{E}_{97.5\%}$ . Indeed, this is one of the advantages of using an integrated EIV-Bayesian Changepoint approach: lower variability in the estimated elastic modulus compared to using bounds on the calibration

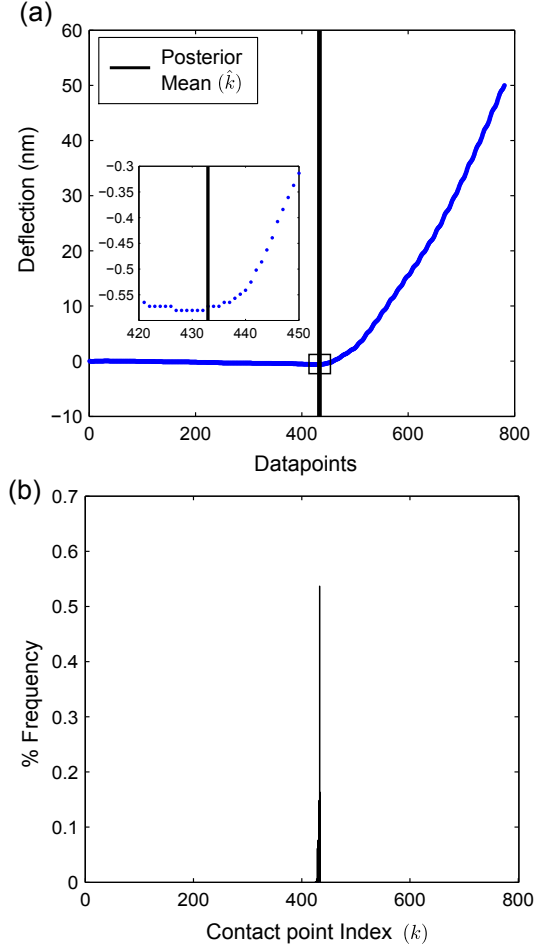


Figure 4.8: Results of the EIV-Bayesian Changepoint algorithm on a representative AFM force curve on breast tissue with  $n = 783$  datapoints. (a) AFM force curve with the posterior mean of the contact point index at  $\lfloor \hat{k} \rfloor = 433$ . (b) Marginal posterior of  $k$ .

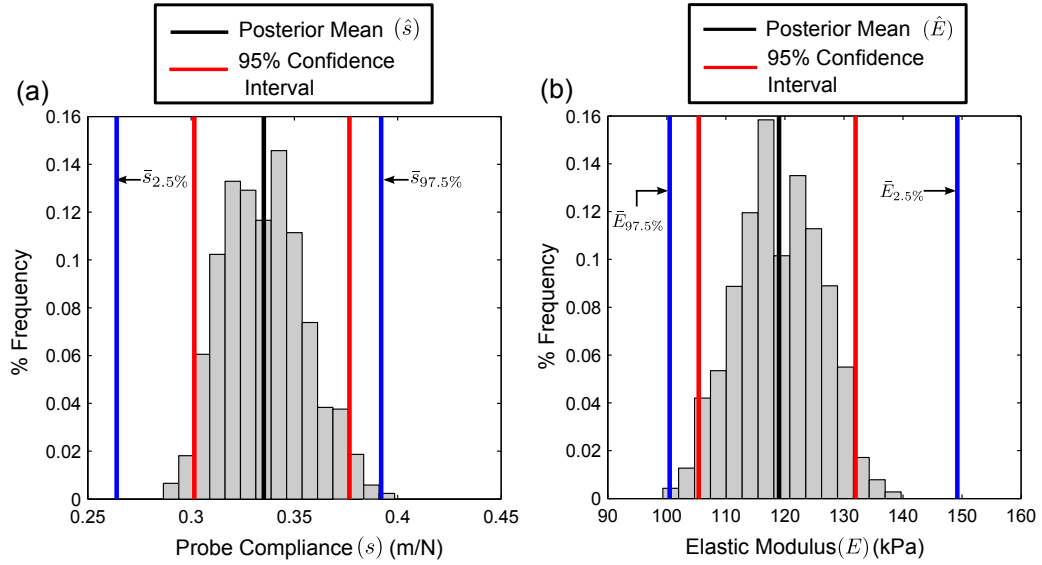


Figure 4.9: (a) Marginal posterior in  $s$  and (b) marginal Posterior of  $E$ .

data and point estimates of the contact point to compute the elastic modulus.

#### 4.4.4 Sensitivity Analysis

The dispersed nature of the marginal posterior in the elastic modulus in Fig. 4.9(b) raises an interesting question - what are the individual contributions of the contact point uncertainty and the probe compliance variability in the marginal posterior distribution in  $E$ ? More importantly, does the marginal posterior in  $E$  reflect changes in the hyperparameter values of the probe compliance, given that an informative prior was used for it?

##### 4.4.4.1 Varying $\sigma_{s_p}$

The effect of using hypothetical values of  $\sigma_{s_p}$  on the marginal posteriors is illustrated in Fig. 4.10. The dispersion of the marginal posterior in  $E$  increases

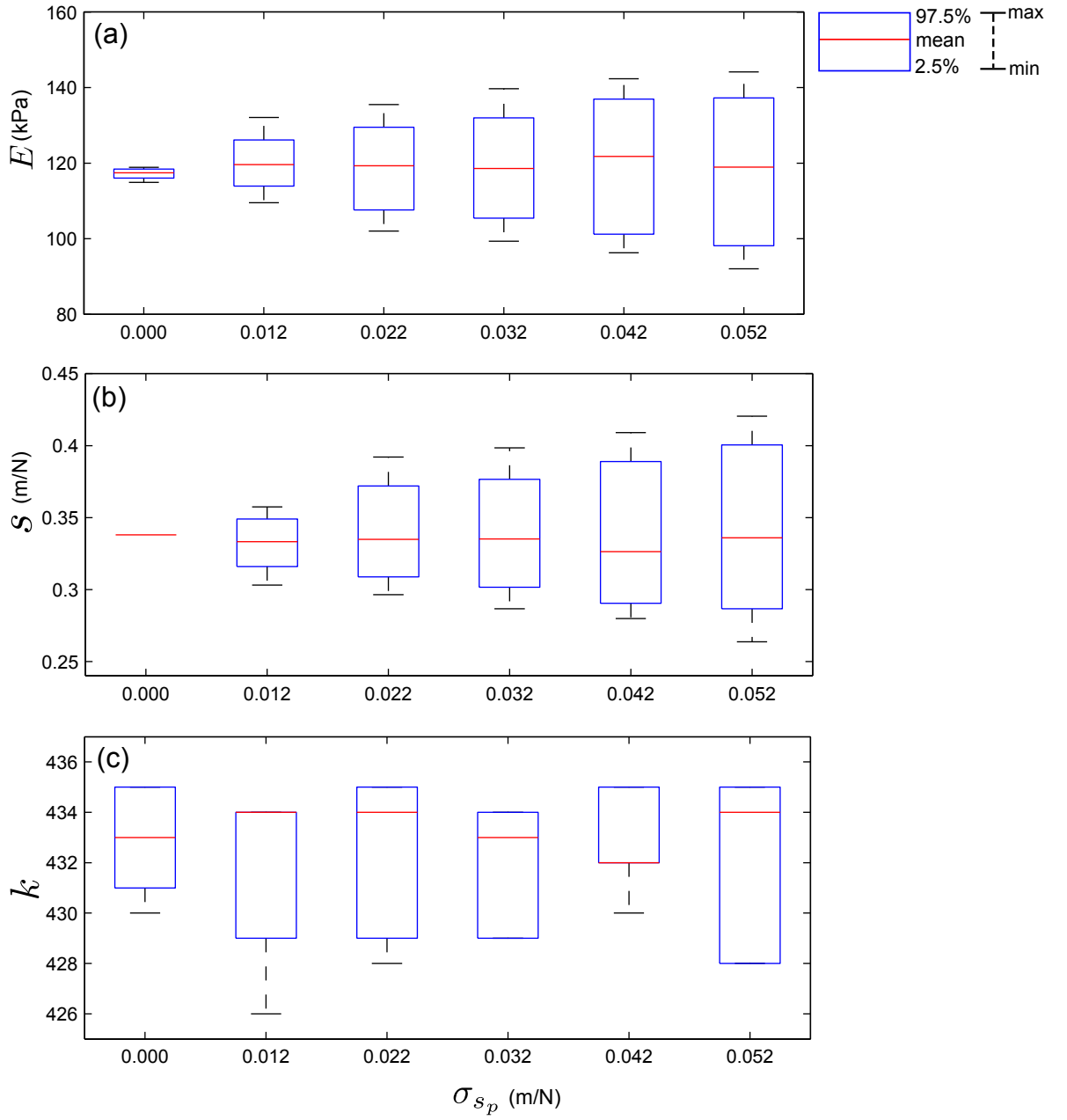


Figure 4.10: Boxplots of the marginal posterior distributions (a) in  $E$ , (b) in  $s$  and (c)  $k_c$ . Please note that the  $\sigma_{s_d}$  has been assumed to be equal to  $\sigma_{s_p}$ . The fourth boxplot ( $\sigma_{s_p} = 0.032$ ) corresponds to the experimental probe compliance variance as obtained in Table 4.2 ©2014 IEEE.



with  $\sigma_{s_p}$ , as shown in Fig. 4.10(a). This is an expected observation, since larger variations in the calibrated probe compliance would lead to greater uncertainty in the elastic modulus of the probed regions. The individual contribution of contact point uncertainty on marginal posterior in  $E$  is given in the first boxplot of Fig. 4.10(a) (corresponding to  $\sigma_{s_p} = 0.000$ ).

Likewise, increase in  $\sigma_{s_p}$  leads to greater dispersion in the marginal posteriors in  $s$  [Fig. 4.10(b)]. It is worth noting that changes in  $\sigma_{s_p}$  does not cause any substantial change to the posterior means of  $E$  or  $s$ .

The boxplots of Fig. 4.10(c) shows the effect of  $\sigma_{s_p}$  on the marginal posterior in  $k$ . It can be observed that changes in  $\sigma_{s_p}$  has no significant effect on the posterior in  $k$  - the 95% confidence intervals varies between the 428<sup>th</sup> and 435<sup>th</sup> datapoints. This is an important observation, since uncertainties in the probe compliance and the contact point are physically unrelated - probe compliance variations are the result of calibration errors, while contact point uncertainty occurs because of the soft nature of biological tissues and the absence of a perceptible attractive region in the AFM force curve in liquid.

#### 4.4.4.2 Varying $\mu_{s_p}$

The effect of varying the hyperparameter  $\mu_{s_p}$  on the marginal posteriors in  $E$  and  $s$  are shown in Figs. 4.11(a) and 4.11(b) respectively. The previous values of  $s_d (= 0.339)$  m/N and  $\sigma_{s_d} (= 0.032)$  m/N and the assumption that  $\sigma_{s_d}^2 = \sigma_{s_p}^2$  are retained. The first boxplot shows the marginal posteriors when  $\mu_{s_p}$  is set to

0.222 m/N, the probe manufacturer’s rated compliance. This is often useful when the AFM user performs a single probe calibration experiment, and wishes to see the result of using the rated compliance instead of repeating the calibration experiments. The second boxplot uses  $\mu_{s_p} = 0.328$  m/N, obtained from Table 4.2.

Reducing the hyperparameter  $\mu_{s_p}$  from 0.328 m/N to 0.222 m/N leads to an increasing trend in the marginal posterior in  $E$  [Fig. 4.11(a)] and a corresponding decreasing trend in the marginal posterior in  $s$  [Fig. 4.11(b)]. This is understandable, given the inverse relationship between  $s$  and  $E$  [see Eqn. (4.10)]. This inverse relationship is also responsible for the increased dispersion in the first boxplot of Fig. 4.11(a) compared to the second; in contrast both boxplots in Fig. 4.11(b) show largely similar dispersed behavior.

It is also evident from Fig. 4.11(b) that the probe compliance posterior means ( $\hat{s}$ ) lie approximately midway between the compliance data  $s_d$  and the hyperparameter  $\mu_{s_p}$  ( $\hat{s} = 0.283$  m/N for  $\mu_{s_p} = 0.222$  m/N and  $\hat{s} = 0.333$  m/N for  $\mu_{s_p} = 0.328$  m/N). This is a direct consequence of using equal weightage to the data and prior variances of the probe compliance, i.e. ( $\sigma_{s_d}^2 = \sigma_{s_p}^2$ ).

## 4.5 Conclusions

This chapter outlines the formulation of an integrated EIV based-Bayesian Changepoint algorithm used to obtain robust estimates of the elastic modulus of biological specimens from AFM force curves in the presence of variability in the contact point and probe spring constant. The major highlights of this chapter are

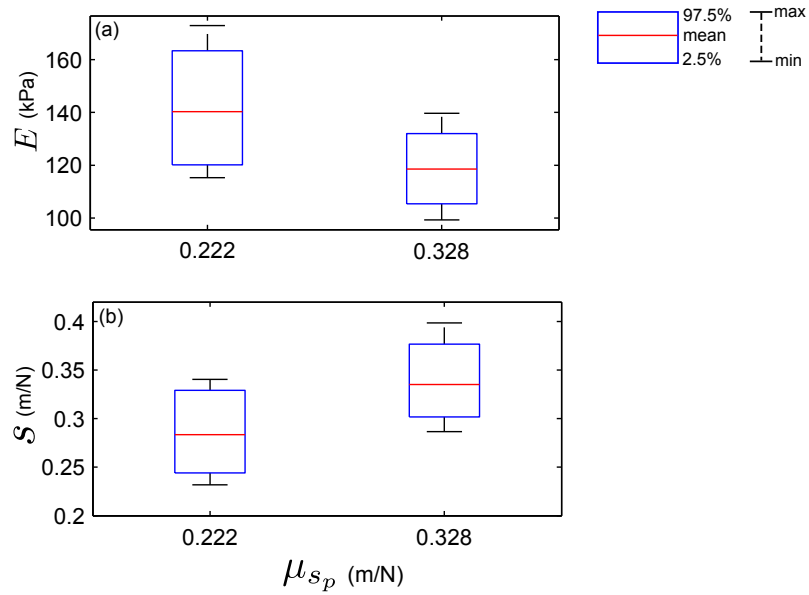


Figure 4.11: Boxplots indicating the effect of varying  $\mu_{s_p}$  on the marginal posteriors (a) in  $E$  and (b) in  $s$  ©2014 IEEE.

enumerated as follows:

1. Transforming the probe spring constant to the equivalent probe compliance, a standard Bayesian Changepoint problem [48] could be set up to accommodate variability in the probe spring constant. This allowed the application of error-in-variables based methods to be applied to the Bayesian Changepoint algorithm. Multiple probe calibration experiments were conducted to obtain the variability in the probe compliance using the thermal calibration method. These results were used to specify the hyperparameters of the prior distribution of the probe compliance.
2. The proposed algorithm performed satisfactorily on simulated AFM data, and the estimation errors were within 4%. Also, the ground truth was contained within 95% confidence intervals of the marginal posteriors.

3. On implementing the algorithm on AFM datasets obtained from breast tissue specimens, it was observed that using an integrated approach, the variability in the estimates of the elastic modulus could be reduced, as opposed to point-based approaches to estimate the elastic modulus by treating each source of variability piecemeal.
4. A sensitivity analysis on the parameters of the posterior distribution showed that the proposed algorithm model responded satisfactorily to a wide range of hyperparameter values in the probe compliance.

Accurate estimation of the contact point shown in Fig. 4.5 and the sensitivity plots shown in Figs. 4.10 and 4.11 confirm the research hypothesis of this chapter that EIV-Changepoint algorithm successfully estimates the elastic modulus due to the aforementioned sources of uncertainty.

One of the appealing aspects of using the EIV-Bayesian Changepoint formulation is that it makes it possible to automate data analysis of AFM force curves, since the contact point from the AFM force curves can be determined fairly accurately without subjective user input. As mentioned previously in chapters 2 and 3, AFM indentation studies on breast tissue for histopathological inference necessitates very large scale AFM indentation data acquisition and processing. A robust and computationally efficient approach can significantly improve throughput of AFM based characterization of biomaterials by allowing batch-processing of AFM curves.

The proposed approach also obviates the need to truncate AFM force curve datasets to ensure applicability of linear elastic theory. The use of Long’s contact

model [59] accounts for geometric and material nonlinearities and therefore the whole AFM force curve can be processed to estimate material properties.

However there are certain limitations of this work that require elaboration. These are stated as follows:

1. The EIV-Bayesian Changepoint algorithm assumes that the force-indentation contact relationship appropriately fits the post-contact AFM deflection data. As a result, the algorithm has been implemented only on those AFM datasets where the post-contact deflection data could be well described by the contact model in question, i.e., Hertz or Long's contact model. For force curves that display sharp nonlinearity, Long's contact model is not likely to be an appropriate contact model since it only accounts for neo-Hookean hyperelastic behavior - which is a first order approximation of higher order hyperelastic material models. The effect of contact estimation on force curves with pronounced nonlinear effects are dealt with separately in Chapter 5.
2. Errors in the observed probe compliance have been assumed to follow a Gaussian distribution - this assumption has not been experimentally validated. The assumption of normality in the observed probe compliance and in the prior distributions of the probe compliance was primarily aimed at simplifying the sampling of the joint posterior using standard MCMC methods like Gibbs Sampling. Indeed, large scale probe calibration experiments are necessary to ascertain the nature of the distribution to which the calibrated probe compliance errors belong.

3. In the two regime regression model (Eqn. 4.12) used for the EIV-Bayesian Change point analysis, continuity was not assumed at the contact point. This did not impact the performance of the EIV-Bayesian Change point algorithm, primarily because the algorithm was only implemented with force curves that could be described well by the contact model chosen in the analysis (Hertz or Long's [59] contact model). For force curves that cannot be adequately described by the contact model, the contact point estimates are likely to be erroneous. These issues are dealt with in detail in chapter 5.

## Chapter 5

# Constitutive material modeling of the tissue specimens under AFM indentation

### 5.1 Overview

In chapters 2 and 3, the Hertzian contact model was used to extract the tissue elastic modulus, which relies on the theory of linear elasticity and infinitesimal strains, to estimate the elastic modulus of the tissue specimens. This was on account of its computational ease and also because the primary objective was to investigate any elasticity differences between normal and cancerous specimens, not so much to assess the appropriateness of the contact model for any given force curve. In chapter 4, Long’s contact model [59] was implemented in the EIV-Bayesian Changepoint estimation algorithm, which relaxes the assumptions of linear elasticity in the material by accounting for neo-Hookean hyperelasticity. However, the algorithm was only implemented on those force curves that could be adequately described by Long’s contact relationship.

In this chapter, greater emphasis is placed on the choice of the contact model to describe AFM force curves with varying levels on nonlinear elasticity and numerical approaches are explored that might be better suited for elastic modulus estimation from the tissue specimens. The coupled problem of contact estimation from highly

nonlinear force curves is also investigated, and a modification to the contact estimation algorithm from chapter 4 is proposed, which can be used in conjunction with numerical techniques for tissue mechanical property estimation.

It should be mentioned here that in this chapter, the probe spring constant (or compliance) is assumed to be observed without errors and no consider variability in the probe's spring constant is considered in the work outlined in this chapter.

## 5.2 Experimental Challenges in enforcing Hertzian assumptions

The applicability of the Hertz contact model for analyzing AFM indentation data on biomaterials has critically studied in the past [1],[66] - nevertheless, a critical assessment of each of the assumptions in Hertzian theory in the context of prevailing experimental conditions during AFM indentation on breast tissue specimens is presented in the following discussion.

It may be recalled from chapter 2 that the assumptions in Hertzian contact model for spherical indentation of tissue specimen are:

(H1) The contact between the indenter and the specimen is considered frictionless.

(H2) There is no adhesion between the sphere and the indenter.

(H3) The displacements and strains in the specimen are assumed to be small so that a linearized continuum theory can be used.

(H4) The specimen is assumed to be an infinite half-space.

(H5) The specimen is linearly elastic.



(H6) The specimen is homogeneous and isotropic.

The assumption (H1) of frictionless contact implies that shear tractions at the contact interface are zero. Since AFM indentation on tissue specimens are primarily conducted in PBS medium, this is a reasonable assumption to make in the present study.

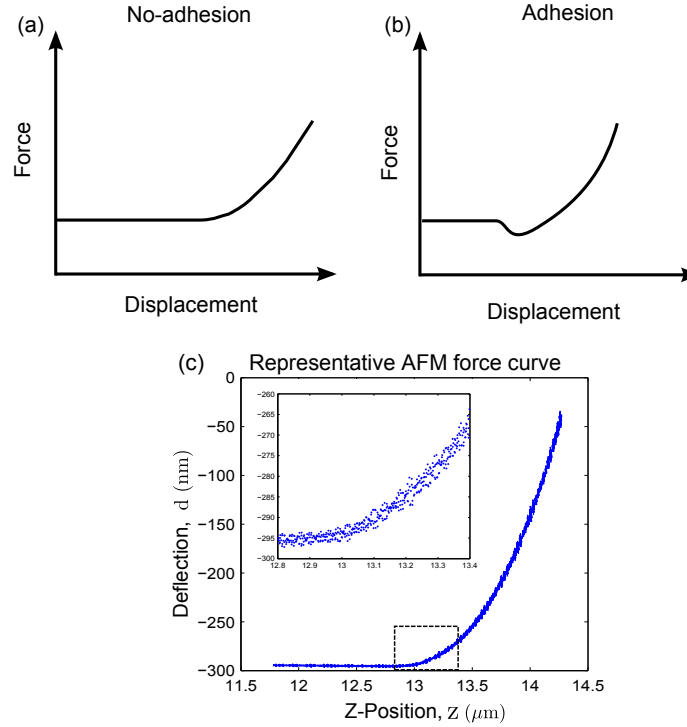


Figure 5.1: Schematic of force-displacement behavior for (a) adhesion-free indentation, (b) indentation with adhesion and (c) representative AFM force curve on breast tissue specimens showing absence of prominent adhesive region.

The assumption (H2) of adhesion between the tissue and the indenter is not a trivial one. Live mouse fibroblasts [67] and polyvinyl alcohol gels [68] have previously shown adhesive behavior when subjected to AFM indentation, which causes the AFM probe to deflect toward the sample surface resulting in attractive (negative force) regime in the AFM force curve [see Fig. 5.1(a) and Fig. 5.1(b)]. However, as

seen in chapters 2, 3 and 4, no adhesion was observed in the force curves on the tissue specimens [Fig. 5.1(c)], consequently, modeling adhesion is not a significant concern in this study.

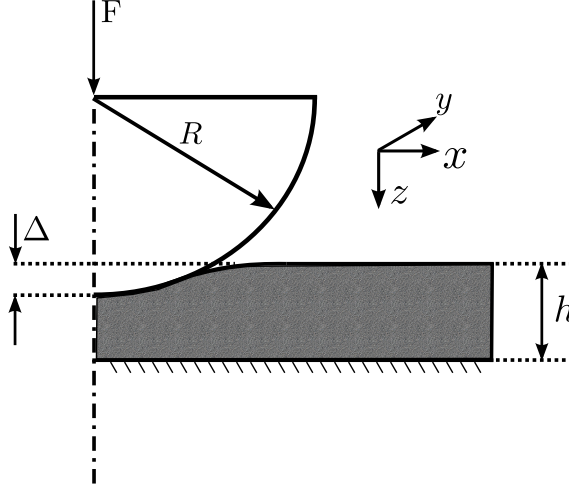


Figure 5.2: Finite-indentation of a thin specimen by a rigid hemispherical indenter.

Assumptions (H3) and (H4) constitute two of the most critical assumptions that are often violated during AFM indentation studies on tissue specimens. The infinitesimal assumptions in (H3) and (H4) imply the following:

$$\Delta \ll R \tag{5.1a}$$

$$\Delta \ll h \tag{5.1b}$$

$$R \ll h \tag{5.1c}$$

$$h \rightarrow \infty \tag{5.1d}$$

In order to ensure applicability of Eqns. (5.1a) and (5.1b), AFM force curves need to be acquired in indentation-controlled mode to restrict the sample indentation to the Hertzian regime. However, conducting AFM experiments in indentation-controlled

mode is significantly harder compared to force-controlled mode due to the challenges in online contact estimation, as stated previously in chapter 2. Coupled with the need to perform raster-scans on the tissue specimens for large-scale AFM force curve acquisition, indentation-controlled mode becomes a far less attractive mode compared to force-controlled mode for high throughput purposes. The drawback associated with force-controlled AFM experiments, however, is that highly compliant regions in the tissue register very large indentations, which violate assumptions (5.1a) and (5.1b).

Applicability of Eqns. (5.1c and 5.1d) can be achieved by adjusting the bead size with respect to the specimen thickness. However, as observed previously in [24], probe tips with low radius (for example, pyramidal tips with nm-range radius) can cause permanent damage to the tissue samples [69]. Even worse, sharp tips possess the undesirable tendency of including contributions from the substrate [70], leading to inaccurate material characterization. An optimum range of  $R \sim 5 - 10 \mu\text{m}$  ensures low stress concentration in the tissue specimens, and also aids on averaging out local tissue heterogeneity. Tissue specimen thickness also can be varied from  $h = 4 \mu\text{m}$  to  $h = 10 \mu\text{m}$ , however, thick tissue specimens also lead to loss of continuity in the tissue architecture across consecutive tissue slices. Even in the most optimistic case of  $(R, h) = (5, 10) \mu\text{m}$ ,  $R/h = 0.5$ , which is clearly too large to enforce infinitesimal assumptions.

As observed in chapters 2 and 3, the tissue specimens studied in this dissertation consists of complex three-dimensional architecture with functional breast epithelial cells that are enclosed by collagen-rich stromal tissue - which violates

isotropic and homogeneity assumptions [Assumption (H6)]. Moreover, macroscale breast tissue specimens have previously shown nonlinear elasticity [Assumption (H5)] [71].

The combined effect of violations in assumptions (H3-H6) is well-illustrated in Fig. 5.3, which illustrates the spatial distribution of the tissue stiffness [Fig. 5.3(a)] and the corresponding goodness of fit [Fig. 5.3(b)] on a tissue ROI. It can be observed that while the tissue stiffness shows clear delineation from the upper left to the lower right end of the elasticity map, no such patterns can be observed in the  $R^2$  distribution. Figs. 5.3(c) and 5.3(d) show the force-indentation plots of two neighboring sampled points with similar stiffness, but with vastly dissimilar nature of the Hertzian fit. These results underscore the need to have specific material constitutive laws to extract accurate elasticity measures from AFM indentation data. In the following section, prior work in the development of contact models that overcome the limitations of the Hertz contact model are critically reviewed.

### 5.3 Related Work

Previous research addressing non-Hertzian behavior in biomaterials undergoing AFM indentation can be classified by the individual Hertzian assumptions (H1-H6) that are targeted and corrected. Since the scope of this research is primarily directed towards addressing violations in assumptions (H3-H6), a description of some of the approaches proposed in literature that focus on these assumptions only is presented in the following discussion. Readers are requested to look elsewhere for

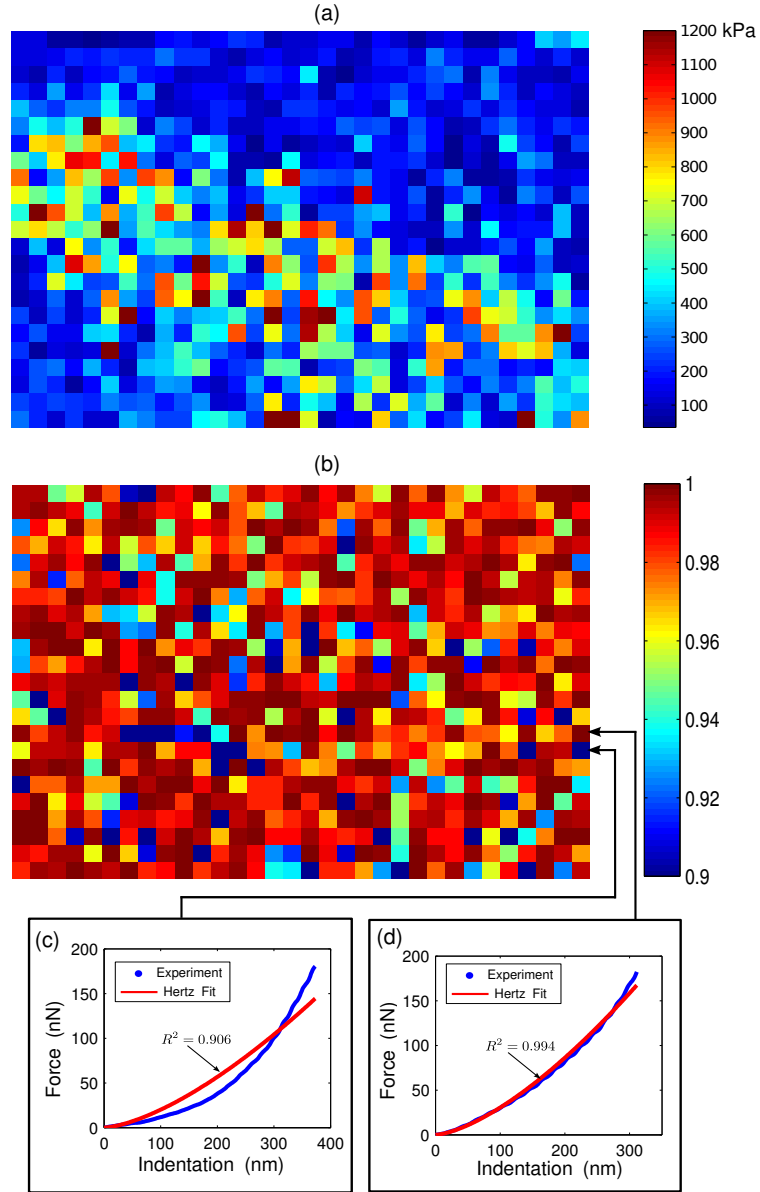


Figure 5.3: Effect of heterogeneity in the spatial stiffness distribution. (a) An elasticity map in the cancer core [from Fig. 3.11(b)], (b) corresponding 2-D representation of the R-square of Hertzian fits and (c,d) representative force-indentation plots showing the inadequacy of the Hertz model to describe the entire ROI's constituent behavior.

corrections to violations in (H1) [72] and (H2) [67].

- *Finite Indentation (H3,H4)*: Improvements to the Hertz contact model to account for thin specimen indentation was primarily motivated by AFM indentation studies on thin polymer gels, wherein it was observed that the Hertz contact model significantly overestimated the elastic modulus due to the effect of the underlying stiff substrate [70]. The most seminal contribution in this regard points to the work of Dimitriadis and his co-workers [44]. Dimitriadis *et al.* [44] appended correction terms to the Hertz contact model that led to an analytical force-indentation relationship as given below<sup>1</sup>:

$$F = \frac{4E\sqrt{R}\Delta^{1.5}}{3(1-\nu^2)} \left[ 1 - \frac{2\alpha_0}{\pi}\kappa + \frac{4\alpha_0^2}{\pi^2}\kappa^2 - \frac{8}{\pi^3} \left( \alpha_0^3 + \frac{4\pi^2}{15}\beta_0 \right) \kappa^3 + \frac{16\alpha_0}{\pi^4} \left( \alpha_0^3 + \frac{3\pi^2}{5}\beta_0 \right) \kappa^4 \right] \quad (5.2)$$

where  $E, R, \Delta, \nu$  have their usual meanings,  $\kappa = R\Delta/h^2$  and  $\alpha_0, \beta_0$  are constants that depend on the Poisson's ratio  $\nu$ .

In the limit  $\kappa \rightarrow 0$ , Eqn. (5.2) reduces to the classical Hertz contact model. It is noteworthy here that for this to happen, it is not sufficient to restrict the indentation depth  $\Delta$  for a given specimen thickness  $h$  only (presumably using indentation-controlled AFM indentation experiments). Even for moderately low  $\Delta$  values, a large bead radius  $R$  could possible make  $\kappa$  non-zero, thereby invalidating Hertzian assumptions of infinitesimal strains. In the recent past, Santos *et al.* [73] have investigated the influence of probe geometry (with pyramidal/conical indenters of nm-range radius) on the elastic modulus from

---

<sup>1</sup>Validation of the Dimitriadis model using finite element analysis is given in Appendix A.

thin specimens using numerical methods.

- *Nonlinear Elasticity (H5)*: To account for nonlinear elasticity effects in biomaterials, Costa *et al.* [1] proposed a “pointwise modulus” approach to estimate the elastic modulus as a function of the indentation in the sample. For a purely Hertzian response, the “pointwise modulus” is constant during the entire indentation regime, whereas for violations in Hertzian assumptions, the “pointwise modulus” show distinct nonlinearity. While this approach successfully differentiates a Hertzian response from a non-Hertzian one, the effect of material and geometric nonlinearities (finite indentation) are coupled and there is no way to isolate these two violations in Hertzian assumptions using the “pointwise modulus” approach solely.

Drawing upon parallels between uniaxial compression and indentation, Lin *et al.* [74][75] proposed a reduction formulation to convert force-indentation datasets into “indentation stress” ( $\sigma^*$ ) v/s “indentation strain” ( $\epsilon^*$ ) plots. This was accomplished by dividing the contact force  $F$  by the contact area to obtain  $\sigma^*$ , and expressing  $\epsilon^*$  as a function of the contact area [76], as shown below [74]:

$$\sigma^* = \frac{F}{\pi a^2} \quad (5.3a)$$

$$\epsilon^* = 0.2 \frac{a}{R} \quad (5.3b)$$

$$a = R^{1/2} \Delta^{1/2} \quad (5.3c)$$

where  $a$  is the contact area. For a purely Hertzian response,  $\sigma^*$  -  $\epsilon^*$  are given by [74]:

$$\sigma^* = \frac{20E}{3\pi(1 - \nu^2)}\epsilon^* \quad (5.4)$$

It is noteworthy that  $\sigma^*$  varies linearly with  $\epsilon^*$  for Hertzian indentation (Eqn. 5.4), which is expected due to assumptions of material linearity in Hertzian theory. Lin [74] then demonstrated that force-indentation equations could be obtained for a wide range of hyperelastic materials by obtaining  $\sigma^*$  as a function of  $\epsilon^*$  from their strain energy densities and then recasting them into Eqns. (5.3a) and (5.3b).

While this approach is attractive due to its mathematical elegance in defining explicit force-indentation relations for hyperelastic materials, its fundamental shortcoming is that finite-indentation effects are not accounted for. This is well demonstrated in Fig. 5.4. In Fig. 5.4(a), the purple force-indentation plot corresponds to a simulated Hertzian response on a specimen of elastic modulus  $E = 400$  kPa, while the cyan plot represents the force response on a finite element (FE) model<sup>2</sup> of a linearly elastic specimen of thickness  $h = 4\mu\text{m}$  and same elastic modulus ( $E = 400$  kPa). As expected, the force response for the FE model is higher due to the underlying stiff substrate [44]. When these force-indentation plots are recast into  $\sigma^*$  -  $\epsilon^*$  plots using Eqn. 5.3(a-c), it becomes apparent that the FE solution shows significant deviation from the

---

<sup>2</sup>The details of the finite element (FE) model used to generate this plot are given in section 5.5.



Hertzian response [Fig. 5.4(b)], which is linear (from Eqn. 5.4). This nonlinearity occurs in the FE response not due to any hyperelasticity in the material, but due to the incorrect formulation in the indentation strain  $\epsilon^*$  in Eqn. 5.2(b) which does not account for specimen depth. In fact, research groups have also defined representative indentation strain as  $\Delta/t$  and  $\Delta/R$  [77]; however, there is no general consensus on this matter. Apart from the aforementioned works,

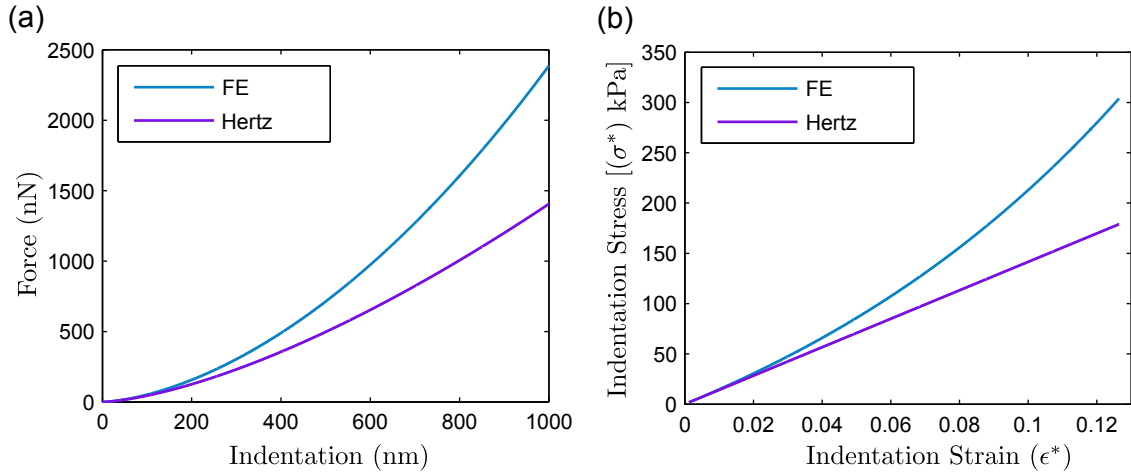


Figure 5.4: Effect of finite deformation on the force response during spherical indentation. (a) Simulated force response on a finite element model of a tissue specimen (cyan) and a Hertzian force response of the same elastic modulus (purple) and (b) corresponding indentation stress  $(\sigma^*)$  - indentation strain  $(\epsilon^*)$  using Eqns. (5.3a - c).

researchers have proposed inverse FE based methods to estimate hyperelastic material parameters from AFM force curves [78][79][80]. Most of these methods, however, do not consider the problem of finite-indentation.

- *Finite Indentation & Nonlinear Elasticity (H3,H4,H5)*: Amongst the first groups to study the coupled problem of finite indentation and material nonlinearity was that of Kosta and Yin [66]. Using finite element methods and the

“pointwise modulus” [1] approach, the authors studied the effects of indenter geometry, hyperelasticity and sample thickness for AFM based characterization studies. Likewise, Oommen and Val Vilet [77] studied the effects on indentation on thin hyperelastic polymeric films using FE methods. However, most of these approaches are primarily exploratory, and have little implications in estimating the elastic modulus from any given AFM force-curve.

In this context, the work of Long *et al.* [59] gains prominence: Long *et al.* extended Dimitriadis’ approach [44] of appending correction factors to the Hertz model, and both finite-indentation and material nonlinearity were accounted for in [59]. Using a judicious choice of exponents of  $\kappa$  ( $= R\Delta/h^2$ , see Eqn. 5.2) in the correction terms, Long *et al.* fitted FE force-indentation data from a neo-Hookean hyperelastic material to an analytical expression of force  $F$  as a function of  $R, \Delta, \kappa$  (see Eqn. 4.7 for full expression), and obtained critical bounds of  $R/h$  and  $\Delta/h$  in which the expression was valid. Since the force  $F$  could be explicitly related to  $\Delta$ , it was also possible to use Long’s contact model in the EIV-Bayesian Changepoint analysis for uncertainty quantification in chapter 4.

However, as seen later in section 5.4, even neo-Hookean hyperelasticity is not adequate to describe some of the force curves that are acquired during AFM raster scanning on breast tissue specimens.

- *Isotropic and Homogeneity (H6)* Mechanical anisotropy has been shown to exist in bone [81], skeletal muscle [82] and recently, vocal fold tissue [83]. In

[83], the authors carried out indentation studies on vocal fold tissue samples sectioned at different depths along mutually perpendicular axes and the ratio of their elastic modulus was used to quantify the degree of anisotropy.

Heterogeneity in the indentation direction has been addressed using numerical methods. Unnikrishnan *et al.* [84] modeled inhomogeneity in cellular cytoplasm by modeling the actin cortex as a hyperelastic material and inner cytoplasm as a fiber-reinforced composite.

## 5.4 Problem Statement and Proposed Solution

From the preceding discussion in section 5.3 and the results in Fig. 5.3, it becomes clear that accounting for violations (H3-H6) in AFM data analysis is critically important to ensure accurate mechanical characterization. In this context, Long’s analytical relationship [59] appears particularly attractive since it accounts for violations (H3 - H5), however, it must be emphasized that neo-Hookean hyperelasticity is a first-order approximation and it does not capture high degrees of nonlinearities at large indentations. As a result, it might not be capable of capturing the spatially heterogeneous tissue response as seen in Fig. 5.3.

This is well demonstrated in Figs. 5.5 and 5.6 where two experimental force curves E1 and E2 are analyzed by implementing Hertz, Dimitriadis’s and Long’s contact models in the EIV-Bayesian Changepoint algorithm described in chapter 4. In force curve E1 (Fig. 5.5), it is evident that all three contact models fit the

Table 5.1: Summary of implementation of the EIV-Bayesian Changepoint algorithm on two experimental force curves E1 and E2 (Figs. 5.5 and 5.6 respectively acquired on a tissue specimen.)

		Elastic Modulus (kPa)		Contact Point		Est. Indentation $\hat{\Delta} = \delta_n - \delta_{[\hat{k}]}$	$R^2$
		Mean	95% C.I.	Mean	95% C.I.		
Force Curve (E1) (Fig. 5.5)	Hertz	178.30	[153.19 205.98]	447	[446 449]	461.5 nm	0.999
	Dimitriadis	110.48	[95.15 122.98]	427	[425 428]	490.7 nm	0.999
	Long	119.01	[105.41 131.98]	433	[429 434]	481.8 nm	0.999
Force Curve (E2) (Fig. 5.6)	Hertz	151.83	[132.31 175.65]	141	[139, 143]	433.1 nm	0.908
	Dimitriadis	106.27	[92.78 122.92]	141	[139, 143]	433.1 nm	0.926
	Long	114.382	[99.76, 132.27]	141	[139, 143]	433.1 nm	0.917

deflection data well (overall  $R^2 > 0.999$ )<sup>3</sup>. The Hertzian elastic modulus is understandably higher compared to the other two due to infinitesimal assumptions. The estimated elastic modulus using both Dimitriadis’s and Long’s model are close to each other, which can be explained by observing that the Long’s model reproduces the result from Dimitriadis’s model for indentation regimes  $\Delta/h$  close to 0.1 [59] (The neo-Hookean model is “nearly” elastic for low deformation regimes).

Fig. 5.6 shows the implementation on force curve E2 acquired in the spatial neigh-

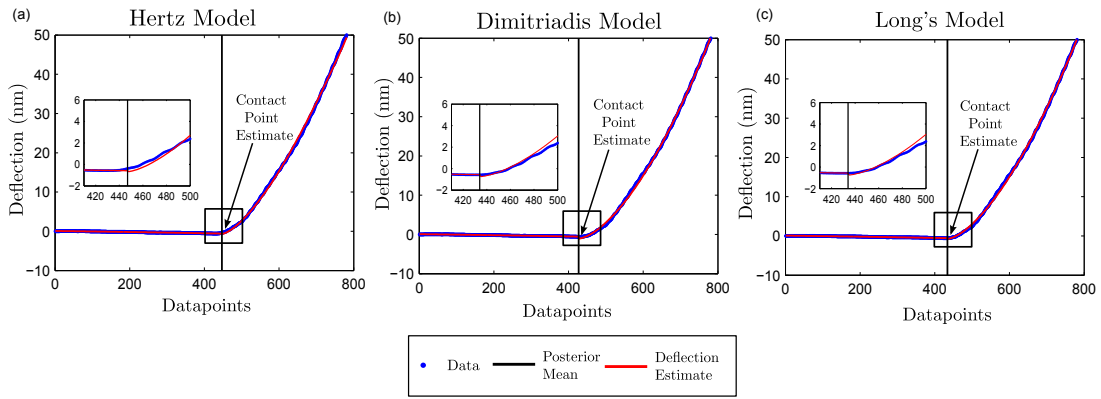


Figure 5.5: Results of Gibbs Sampling on the posterior distribution using (a) Hertz contact model, (b) Dimitriadis’s contact model and (c) Long’s contact model on force curve E1.

borhood of force curve E1. It can be observed that none of the aforementioned contact models produce a good fit (overall  $R^2 \sim 0.90 - 0.92$ ). Typically, such force curves are abundantly acquired during raster scans on tissue specimens, where a single contact model does not appropriately fit all force-curves acquired on a tissue region-of-interest. The poor fit quality indicates that even a neo-Hookean hyperelastic constitutive model is not sufficiently nonlinear enough to explain the sharp tissue response in force curves such as those shown in Fig. 5.6. Furthermore, it

<sup>3</sup>By the term “overall  $R^2$ ”, the fit quality for both non-contact and contact regimes are meant.

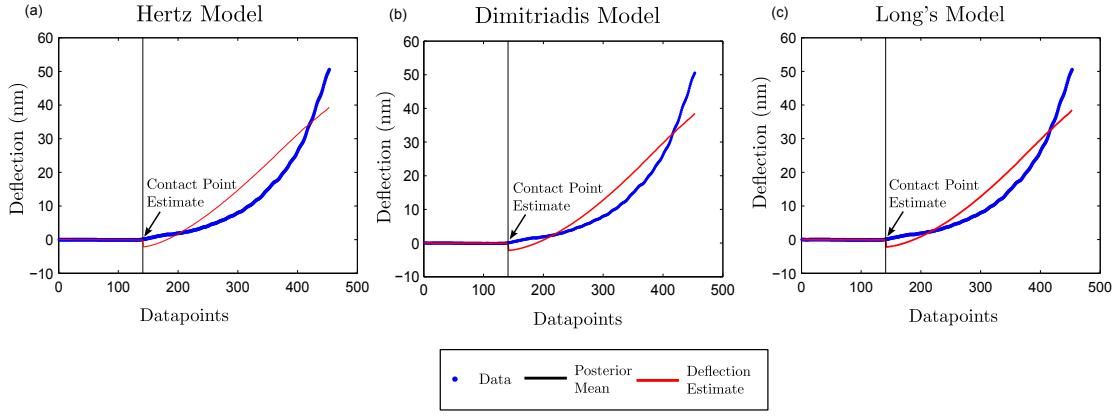


Figure 5.6: Results of Gibbs Sampling on the posterior distribution using (a) Hertz contact model, (b) Dimitriadis's contact model and (c) Long's contact model on force curve E2.

is worthwhile to note that both force curves registered similar indentation range ( $\hat{\Delta}/h \sim 0.115 - 0.122$  for force curve E1 and  $\hat{\Delta}/h \sim 0.108$  for curve E2 for a tissue specimen  $4 \mu\text{m}$  thick) though their fit quality were vastly different. This indicates that large indentation is not the only cause of the observed tissue response in Fig. 5.6, were it to be so, a 10% sample indentation in force curve E1 too would have shown a poor fit quality. This is indicative of the fact that the tissue specimen was inherently nonlinear beyond the neo-Hookean approximation in force curve E2. The immediate implication of this observation is that truncation of force-indentation data, as is often used to limit the fitting range to the linear elasticity regime [78], might still lead to inaccurate estimation of the elastic modulus if the underlying constitutive material model for the force curve is not established.

Up to this point, the effect of the contact point has not been discussed in estimating hyperelastic constitutive parameters from AFM force curves. In chapter 4, the EIV-Bayesian Changepoint algorithm that was used for contact estimation had one critical assumption: the contact model for an AFM force curve was known

beforehand. From the preceding discussion, it is clear that Long’s contact model (with neo-Hookean hyperelasticity) would not be able describe force curves such as the one shown in Fig. 5.6. Therefore, the contact estimation procedure would need to be re-validated for force curves that show high degree of material nonlinearity.

**Hypothesis:** By incorporating finite element modeling of spherical indentation of nonlinear hyperelastic tissue response in the mechanical characterization process, it is possible to improve accuracy and robustness in AFM indentation data analysis.

To address the problem of material nonlinearity beyond neo-Hookean approximation and its associated contact estimation problem, the following solution is proposed:

- *FE analysis of hyperelastic tissue specimens under AFM loading (Assumptions H3-H5:)* To our knowledge, there are no existing explicit contact models for capturing finite-indentation and material nonlinearity simultaneously beyond neo-Hookean hyperelasticity. This necessitates use of numerical techniques to accommodate data analysis for highly nonlinear force curves and to this end, 2D axisymmetric finite element models of tissue specimens with an exponential form of the strain energy density function have been developed that sufficiently captures the nonlinear response as evidenced by Fig. 5.6. The details of the FE modeling is described in section 5.5.
- *Contact Estimation:* A weighted least-squares based approach is proposed to estimate the contact point from force curves with high degrees of nonlinearity.

Details of the contact estimation algorithm are discussed in section 5.6.

It should be mentioned here that during AFM raster scanning on breast tissue specimens, force curves such as Fig. 5.7 were frequently encountered that indicated that the assumption of homogeneity in the indentation direction was violated [Hertzian assumption (H6)]. These force curves were excluded from the data analysis outlined in this chapter. Moreover, isotropic assumptions in the tissue for modeling and analysis were also retained in this chapter.

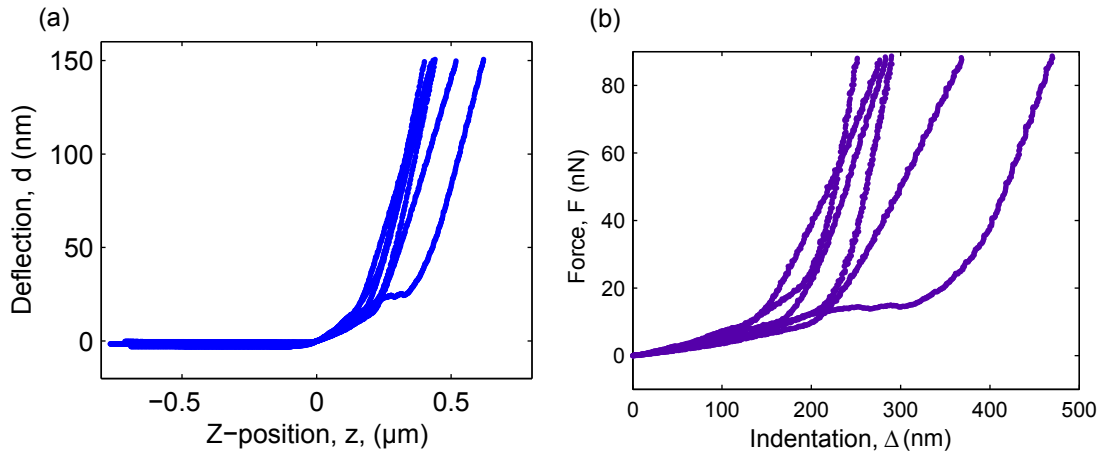


Figure 5.7: Evidence of lack of material homogeneity in the direction of indentation. (a) AFM force curves. Please note that the force curves have been displaced to have the same approximate contact point at (0,0). (b) Corresponding force-indentation curves. Note the change in the nature of the force-indentation curves at 200 nm and 300 nm indentation.

## 5.5 Finite Element Modeling

### 5.5.1 Discretization and Parameter Estimation

The FE analysis was carried out in ABAQUS v6.8 (Dassault Systemes, RI, USA). Taking advantage of the symmetry of the indentation process, a 2D axisym-



metric model of the indenter and the tissue specimen was used. The quarter of the spherical indenter in contact with the specimen was modeled as an axisymmetric rigid indenter.

The tissue specimen consists of 135 axisymmetric, quadrilateral hybrid elements (CAX4H) (15 radially, 9 axially). The length of the tissue model was 6  $\mu\text{m}$ . A fine mesh was used near the indentation region, with a coarser mesh away from it (see Fig. 5.8). No friction was assumed between the indenter and the tissue specimen model. The nodes at the interface of the specimen and the indenter were considered traction free, while the nodal displacements in the radial and axial directions were constrained. Nodes on the axis were constrained to move only along the direction of indentation. Quasistatic equilibrium solutions were acquired for incremental axial displacements of the indenter. In a mesh convergence study, it was verified that mesh size or the length of the tissue model did not have significant impact on the analysis results.

With any single or multi-parameter constitutive model whose explicit force-indentation relationship is unknown, estimating the material properties typically involves solution of an inverse-finite element problem where the simulated response is curve-fitted to experimental data. This is obtained by minimizing the squared norm of the error and is given by the following expression:

$$\arg \min_{\boldsymbol{\theta}} \sum ||F_{exp} - F_{FE}(\boldsymbol{\theta})||^2 \quad (5.5)$$

where  $F_{exp}$  and  $F_{FE}$  represent the experimental and simulated force response re-

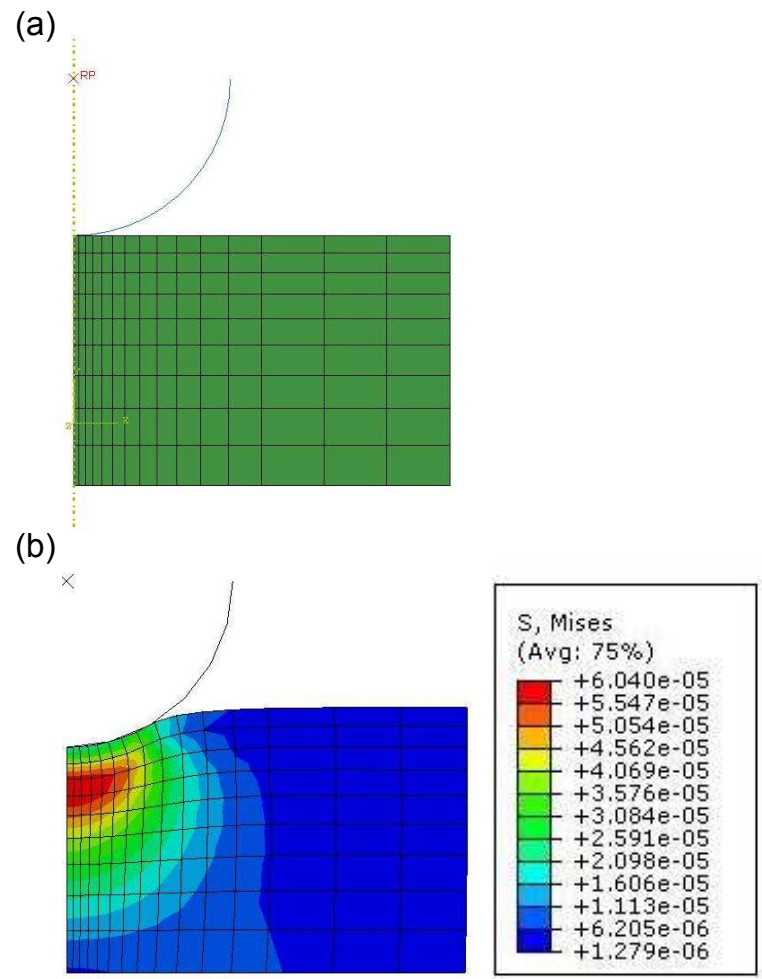


Figure 5.8: Finite element models: (a) undeformed mesh, (b) deformed mesh.

spectively, and  $\theta$  represents a vector of material parameters defined in the constitutive material model. The minimization problem was implemented in MATLAB (Mathworks, Inc) using the *fminsearch* routine which is a heuristic optimizer using the Nelder-Mead simplex algorithm [85]. The optimizer iterates from an arbitrary initial point towards the optimum solution until the incremental reduction in the objective function is lesser than a predefined tolerance. A flowchart indicating the steps of the inverse FE approach is shown in Fig. 5.9.

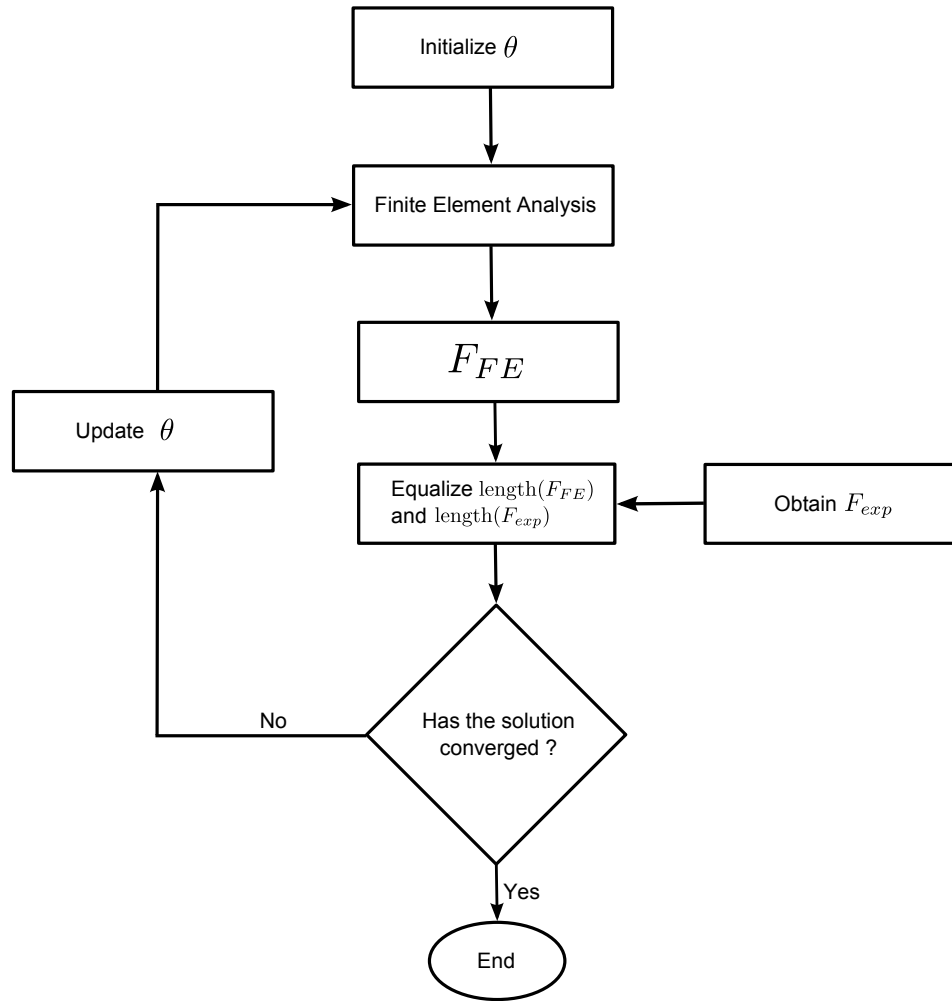


Figure 5.9: Flowchart of the algorithm used to obtain optimized material properties using the inverse FE approach.

Note that in Fig. 5.9, the block “contact estimation” has been included in the flowchart without explicitly describing a technique for it. The contact estimation procedure is discussed in section 5.6.

### 5.5.2 Constitutive Material Models

The tissue specimen is modeled as an isotropic, incompressible and hyperelastic material. Isotropic assumptions in the indentation direction were considered valid because datasets such as those in Fig. 5.7 were not included in this study. Additionally incompressibility conditions were assumed in the tissue specimens due to the hydrated nature of the tissue specimens in phosphate buffered saline (PBS) during AFM indentation experiments.

In order to model force curves like force curve E2 shown in Fig. 5.6, significant material nonlinearity needs to be considered in the constitutive material model. The force response for the following two incompressible hyperelastic materials characterized by the following strain energy functions were examined.

$$W_{YEOH} = C_1(I_1 - 3) + C_2(I_1 - 3)^2 + C_3(I_1 - 3)^3 \quad (5.6a)$$

$$W_{EXP} = \frac{C}{b}[e^{b(I_1-3)} - 1] \quad (5.6b)$$

where  $(C_1, C_2, C_3)$  and  $(C, b)$  are hyperelastic material parameters of the Yeoh and Fung hyperelastic models respectively and  $I_1$  is the first invariant of the Cauchy-Green deformation tensor, expressed in terms of the principal stretch ratio  $\lambda_1, \lambda_2, \lambda_3$

as:

$$I_1 = \lambda_1^2 + \lambda_2^2 + \lambda_3^2 \quad (5.7)$$

where  $\lambda_1\lambda_2\lambda_3 = 1$  Eqn. (5.6a) represents the Yeoh hyperelastic material [86] which can be viewed as a polynomial extension of the neo-Hookean model (with  $C_2, C_3 = 0$ ), and is commonly used to model rubber elasticity. Eqn. (5.6b) represents an exponential form proposed by Fung [87], which has been previously used to model biomaterials. The presence of higher orders coefficients such as  $(C_2, C_3)$  and  $b$  in the Yeoh and Fung models respectively makes these two models particularly attractive in describing highly nonlinear force curves such as Fig. 5.6. While the Yeoh material model was pre-defined in the ABAQUS material library, Fung's model was not. Consequently, the user subroutine **UHYPER** was employed to specify the strain energy function denoted by Eqn. (5.6b) for the FE analysis.

The hyperelastic coefficients can be related to the specimen's materials properties using the relation:

$$\mu_{0,YEOH} = 2 \frac{\partial W_{YEOH}}{\partial I_1} \Big|_{I_1=3} = 2C_1 \quad (5.8a)$$

$$\mu_{0,EXP} = 2 \frac{\partial W_{EXP}}{\partial I_1} \Big|_{I_1=3} = 2C \quad (5.8b)$$

where  $\mu_0$  is the initial shear modulus, which is related to the initial elastic modulus  $E_0$  by:

$$E_0 = 2(1 + \nu)\mu_0 \quad (5.9)$$

When incompressibility conditions ( $\nu = 0.499$ ) apply,  $E_0 = 6C_1$  and  $E_0 = 6C$  for

Yeoh and Fung material models respectively.

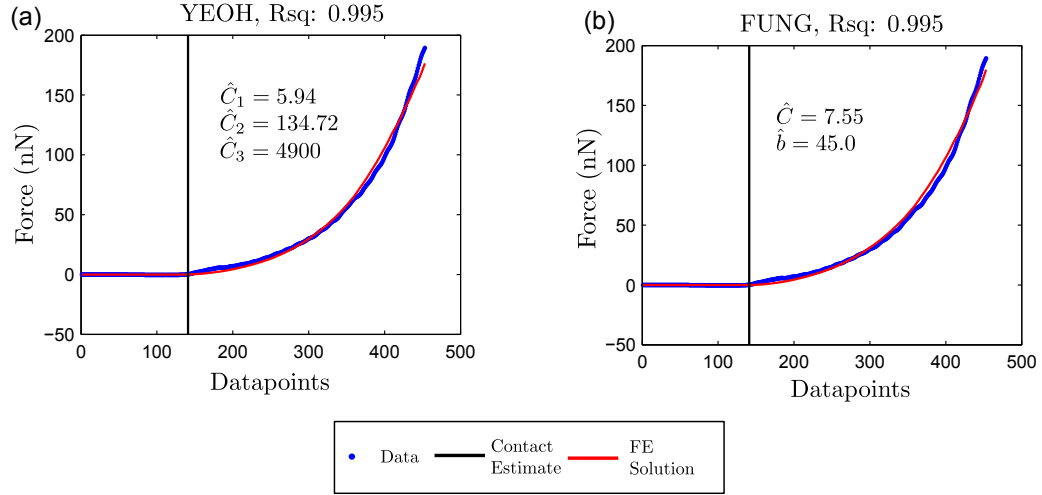


Figure 5.10: Performance of the (a) Yeoh and (b) Fung hyperelastic models in describing the force response for force curve shown in Fig. 5.6.

Fig. 5.10 shows the force curve E2 from Fig. 5.6 overlaid with FE simulation results of indentation on a Yeoh [Fig. 5.10(a)] and Fung hyperelastic material [Fig. 5.10(b)]. The contact point was assumed to be the  $[\hat{k}] = 141$ , as obtained from the EIV-Bayesian Changepoint algorithm, leading to an indentation of 433.1 nm (from Table 5.1) in the simulation. The results demonstrate the applicability of higher order hyperelastic material models to reproduce force curves with pronounced nonlinearity (overall  $R^2 > 0.99$ ). The estimated hyperelastic parameters using an inverse FE analysis were  $(C_1, C_2, C_3) = (5.94, 134.72, 4900)$  kPa and  $(C, b) = (7.55 \text{ kPa}, 45.0)$  for the Yeoh and Fung hyperelastic models respectively. Using Eqn. (5.8), the initial elastic modulus was computed to be  $E_0 = 35.68$  for Yeoh's model and  $E_0 = 45.33$  kPa for Fung's model.

Several conclusions can be drawn from the results in Fig. 5.10. Firstly, estimates of higher order coefficients in the Yeoh model ( $C_2, C_3$ ) are significantly greater

than  $C_1$ , thereby demonstrating that sharp material nonlinearity in the force curve can be successfully captured by  $(C_2, C_3)$ , while  $C_1$  quantifies only the initial tissue response to indentation. Compared to the case where only a single material parameter is extracted from the force curve, i.e. the case when  $C_2 = 0, C_3 = 0$ : a neo-Hookean hyperelastic model where force and indentation explicitly relates by Long's contact model [59], the elastic modulus is significantly overestimated (114.382 kPa, see table 5.1), the obvious implication being that more than one material parameter is necessary to describe the force curves such as the one in Fig. 5.10 completely.

Secondly, the quality of fit and the estimated initial elastic modulus being similar for both the Yeoh and Fung hyperelastic models, a pertinent question comes up: which hyperelastic model should be selected for modeling force curves shown in Fig. 5.10 ?

A parametric study is demonstrated in Fig. 5.11, where the hyperelastic parameters for the Yeoh and Fung models ([Fig. 5.11(a-c)] and [Fig. 5.11(d,e)] respectively) are varied individually, and their corresponding force-indentation curves are obtained. Both the Yeoh and Fung models utilize a single parameter,  $C_1$  and  $C$ , respectively to capture the initial tissue response. For increasing material nonlinearity, Yeoh's hyperelastic model uses two parameters,  $C_1$  and  $C_2$ , while Fung's model uses only one,  $b$ . In this context, the Fung model is appears particularly attractive because of one less hyperelastic parameter compared to the Yeoh model. From the perspective of solving an inverse-FE problem (typically for estimating material properties from an experimental AFM force curve), it is also likely that the Fung model would pose less existence and uniqueness problems compared to the Yeoh model,

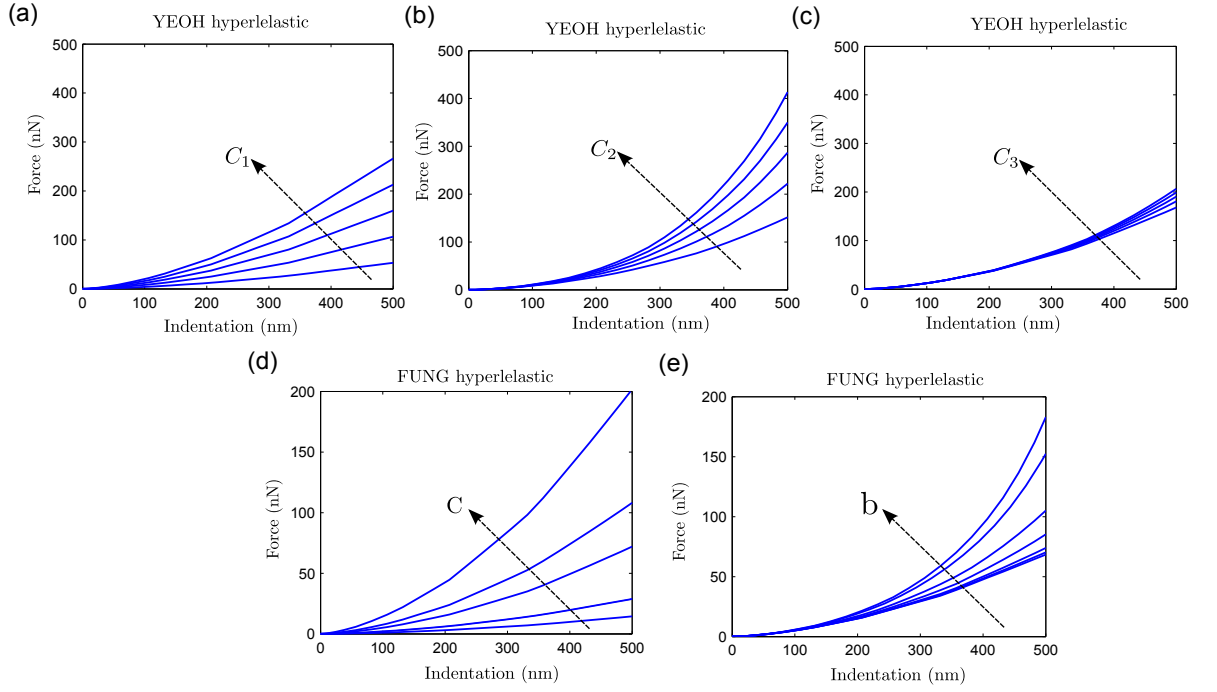


Figure 5.11: Effect of varying the hyperelastic parameters of the Yeoh (a,b,c) and Fung (d,e) hyperelastic models individually.

where material nonlinearity is coupled in between  $C_2$  and  $C_3$ . In contrast, Fung's model is fairly decoupled:  $C$  quantifies the initial elastic modulus, while  $b$  describes the degree of material nonlinearity. For these reasons, *the Fung hyperelastic model is used to describe the observed hyperelasticity in the AFM force curves.*

### 5.5.3 Sensitivity Analysis

Since the Fung model captures material nonlinearity in AFM force curves through the parameter  $b$ , it is instructive to examine the sensitivity of  $b$  to varying degrees of nonlinear elasticity in AFM force curves. The estimated value of  $b$  ( $= 45.0$ ) in Fig. 5.10 raises an interesting question: is there an existence of a lower bound of  $b$  which corresponds to a linear elastic response (the analytical analogue of



which is Dimitriadis's [44] model) ? If this is the case, then the parameter  $b$  could be used to potentially differentiate between linear and nonlinear elastic responses in the tissue specimen, which could serve as an additional mechanical signature for tissue health.

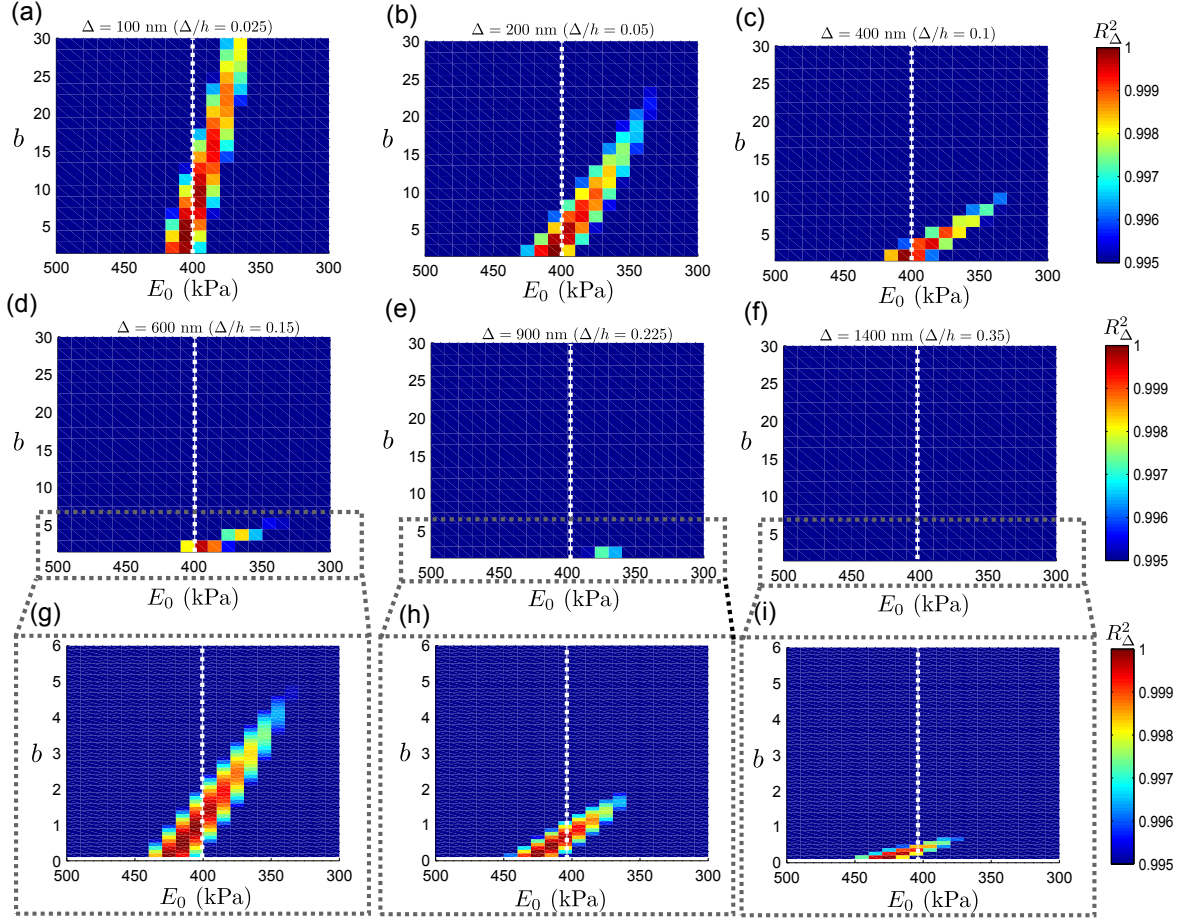


Figure 5.12: Sensitivity of the Fung model parameters at varying indentations. (a)  $\Delta = 100$  nm, (b)  $\Delta = 200$  nm, (c)  $\Delta = 400$  nm, (d)  $\Delta = 600$  nm, (e)  $\Delta = 900$  nm and (f)  $\Delta = 1400$  nm. Also shown in the third row (g-i) are enlarged figures of (d-f) where the range of  $b$  is reduced to 1 – 6. The white dotted line at  $400$  kPa indicates the elastic modulus of the linearly elastic material.

A sensitivity analysis was performed to examine values of  $E_0 (= 6C)$  and  $b$  that resulted in a good fit with a  $F - \Delta$  curve obtained from a linearly elastic material, and the results are shown in Fig. 5.12. The target  $F - \Delta$  curve was

obtained by varying the indentation from  $\Delta = 100$  nm ( $\Delta/h = 0.025$ ) to  $\Delta = 1400$  nm ( $\Delta/h = 0.35$ ) on a linearly elastic specimen of elastic modulus 400 kPa and 4  $\mu$ m thickness.

The ranges of  $E_0$  and  $b$  that fit well with the linearly elastic force response can be compactly expressed by the region  $S_{(\Delta, R_{FE,thresh}^2)} \in \mathbb{R}^2$  where  $S_{(\Delta, R_{FE,thresh}^2)} = \{(E_0, b) | R_{\Delta}^2(E_0, b) > R_{FE,thresh}^2\}$ , where  $R_{FE,thresh}^2$  indicates a pre-specified threshold  $R^2$  value. The term  $R_{FE,thresh}^2$  has implications for an inverse FE analysis during parameter estimation - it determines the termination criteria for an inverse FE solution. In Fig. 5.12,  $R_{FE,thresh}^2$  was chosen to be 0.995 (see colorbar in Fig. 5.12)<sup>4</sup>.

For low indentation regimes such as  $\Delta = 100$  nm, [Fig. 5.12(a)], moderately hyperelastic specimens ( $b \sim 25 - 30$ )<sup>5</sup> produce a linearly elastic response. With increasing  $\Delta$ , the domain of  $S_{(\Delta, R_{FE,thresh}^2)}$  progressively shrinks. The immediate implication of this observation is that parameter estimation using an inverse FE approach is likely to yield inaccurate estimates of  $b$  for shallow indentation regimes due to the relatively large domain of  $S_{(\Delta, R_{FE,thresh}^2)}$ , and it is unlikely that it would be possible to differentiate between linear and hyperelastic tissue response for these regimes. This effect can be avoided during AFM experiments by using a relatively stiff cantilever and specifying (1) a moderately large force setpoint in force-controlled mode, or (2) by setting a large indentation setpoint in indentation-controlled mode.

However, for larger indentations, the estimated values of  $b$  can be used for differentiating between linear and hyperelastic tissue response. This is evident by

---

<sup>4</sup>Minimizing the squared norm of the residuals is equivalent to maximizing the  $R^2$ .

<sup>5</sup>The peak  $b$  at  $\Delta = 100$  nm was 67.0 for  $R_{FE,thresh}^2 = 0.995$  (not shown).

observing that for an indentation of  $\Delta = 433$  nm in force curve E2 of Fig. 5.10 (see Table 5.1), the estimated  $b$  was 45.0, whereas the  $b$  is upper-bounded in  $S_{(400,0.995)}$  by a value of 10-10.5 [see Fig. 5.12(c)]. It now becomes possible to construct a classification curve (see Fig. 5.13), where the linearly elastic tissue response is bounded by  $b_{R_{FE,thresh}^2}^{max}(\Delta)$ , which is defined as:

$$b_{R_{FE,thresh}^2}^{max}(\Delta) := \max\{b | b \in S_{(\Delta, R_{FE,thresh}^2)}\} \quad (5.10)$$

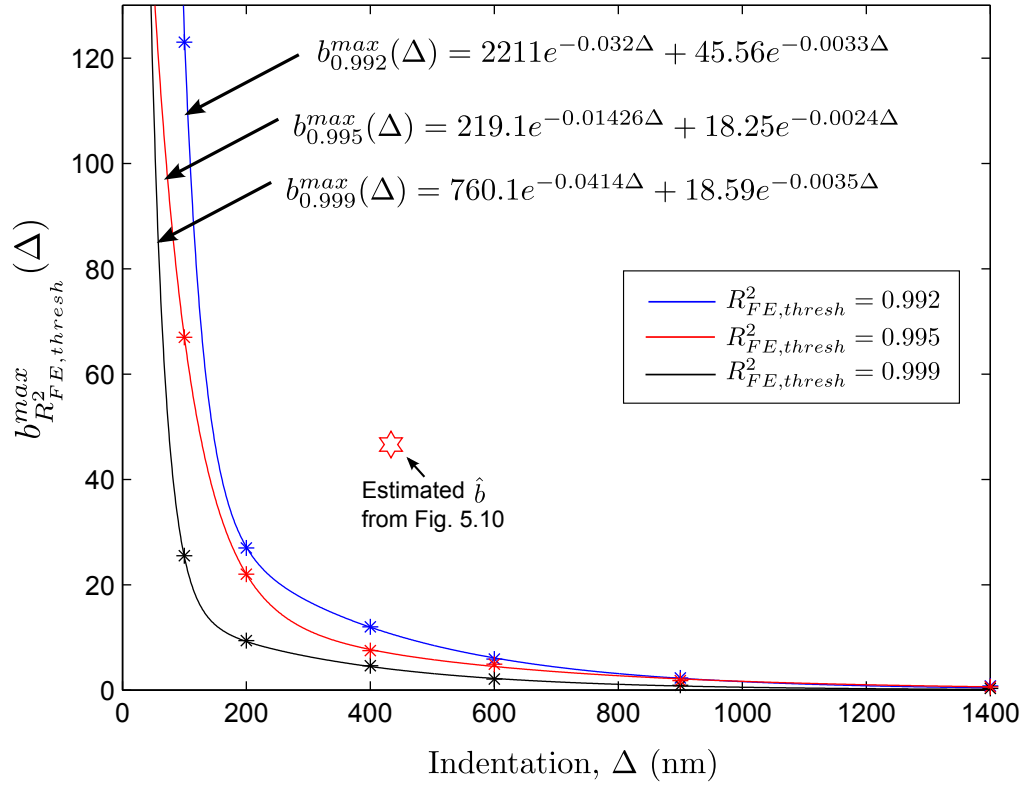


Figure 5.13: Classification curve, showing the variation of  $b_{R_{FE,thresh}^2}^{max}(\Delta)$  with  $\Delta$  for different values of  $R_{FE,thresh}^2$ . Also shown are the curve fits for  $b_{R_{FE,thresh}^2}^{max}(\Delta)$ .

## 5.6 Contact Estimation

In chapter 4, the problem of contact estimation associated with AFM force curves on soft tissue was discussed and a probabilistic EIV-Bayesian Changepoint algorithm was proposed for uncertainty quantification in AFM mechanical characterization. One critical assumption was made in EIV-Bayesian Changepoint algorithm: the post-contact  $F - \Delta$  analytical model was assumed known. It might be recalled that the EIV-Bayesian Changepoint analysis was restricted to those force curves only for which the post-contact regime could be described by the analytical contact model used. For force curves with pronounced hyperelasticity where no contact model exists, the contact estimation problem needs to be revisited.

It was initially envisaged that contact estimation could be integrated in the inverse-finite element algorithm. This would obviate the need to have an explicit analytical contact model for estimating the contact point. Essentially, this approach involved augmenting the cost function (from Eqn. 5.5) with the unknown contact point index  $k$  and simultaneously estimating the set of parameters  $(E_0, b, k)$  that minimized the augmented cost, as shown below:

$$\arg \min_{E_0, b, k} \sum_{i=1}^k [F_i - \beta_{11} - \beta_{12}\delta_i]^2 + \sum_{i=k+1}^n [F_i - F_{FE}(E_0, b)]^2 \quad (5.11)$$

where  $\beta_{11}, \beta_{12}$  are pre-contact regression parameters, which could be estimated by traditional least squares fitting. It might be recalled from chapter 4 that  $\delta$ , was obtained by subtracting the AFM probe,  $d$ , from the vertical probe position,  $z$ , i.e.,

$$\delta = z - d.$$

However, several numerical difficulties were encountered with this approach. Standard gradient-based algorithms and heuristic approaches such as the Nelder-Mead simplex algorithm [85] converged to local minimas, primarily because the curvature of the cost function was significantly lower along the direction of contact (i.e  $k$ ) for smooth transitions compared to the directions of  $E_0$  and  $b$ . Since an inverse-FE approach by itself is computationally expensive, which might have to be implemented on a large number force curves on a given tissue region of interest (ROI), the approach of simultaneous estimation of the contact point and material parameters was not pursued any further.

In the subsequent section, two approaches for estimating the contact are described. First, the bidomain polynomial (BDP) approach without continuity constraint is discussed, which was proposed by [1]. This can be viewed as a deterministic version of a Bayesian Change-point problem<sup>6</sup> that was discussed in chapter 4, nonetheless, a description of this approach is presented for the sake of completeness. Then, a continuity enforced weighted BDP approach is discussed. It should be noted that both these approaches require an explicit contact model.

### 5.6.1 BDP approach without continuity [1]

It might be recalled from chapter 4 that the contact estimation in an AFM force curve was cast as a two-regime regression model with a unknown change-point

---

<sup>6</sup>Since spring constant variations are not considered in this section, the EIV-Bayesian Change-point algorithm reduces to a regular Bayesian Change-point algorithm.

separating the two regimes. The two-regime regression model (Eqn. 4.12 from chapter 4) is restated below:

$$F_i = \begin{cases} \beta_{11} + \delta_i \beta_{12} + \epsilon_1 & \text{if } i \leq k \\ \beta_{21} + f_i \beta_{22} + \epsilon_2 & \text{if } k + 1 \leq i \leq n \end{cases} \quad (5.12)$$

where  $F_i$  is the observed force obtained by multiplying the deflection  $d_i$  by the probe spring constant  $k_c$ ,  $\boldsymbol{\beta}_1 = [\beta_{11} \quad \beta_{12}]^T$  and  $\boldsymbol{\beta}_2 = [\beta_{21} \quad \beta_{22}]^T$  are the pre-contact and post-contact regression coefficients respectively,  $\delta_i$  is the transformed variable obtained as  $\delta_i = z_i - d_i$ ,  $k \in (1, n)$  is the unknown contact index for  $n$  datapoints,  $\epsilon_1 \stackrel{iid}{\sim} N(0, \sigma_1^2)$ ,  $\epsilon_2 \stackrel{iid}{\sim} N(0, \sigma_2^2)$  are the error terms in the pre-contact and post-contact regimes respectively, and  $f_i$  is the contact model.

The bidomain polynomial (BDP) approach seeks to obtain optimal estimates  $(\hat{k}, \hat{\boldsymbol{\beta}}_1, \hat{\boldsymbol{\beta}}_2)$  that minimizes the error between the observed force readings  $F_i$  and the fitted force estimates from the regression model of Eqn (5.12).

As in chapter 4, the force data can be written in compact form as  $\mathbf{F}_1^k = [F_1 \quad F_2 \quad \dots \quad F_k]^T$ ,  $\mathbf{F}_2^k = [F_{k+1} \quad F_{k+2} \quad \dots \quad F_n]^T$  and  $\mathbf{F} = [\mathbf{F}_1^k \quad \mathbf{F}_2^k]$ . The right hand side of Eqn. (5.11) form the design matrices given by:

$$\mathbf{X}_1^k = \begin{bmatrix} 1 & 1 & \dots & 1 \\ \delta_1 & \delta_2 & \dots & \delta_k \end{bmatrix}^T$$

$$\mathbf{X}_2^k = \begin{bmatrix} 1 & 1 & \dots & 1 \\ f_{k+1} & f_{k+2} & \dots & f_n \end{bmatrix}^T \quad (5.13)$$

The optimal estimate for the regression coefficients  $(\hat{\beta}_1^k, \hat{\beta}_2^k)$  at each  $k$  is therefore given by:

$$(\hat{\beta}_1^k, \hat{\beta}_2^k) = \arg \min_{\beta_1, \beta_2} \|\mathbf{F}_1^k - \mathbf{X}_1^k \beta_1\|^2 + \|\mathbf{F}_2^k - \mathbf{X}_2^k \beta_2\|^2 \quad (5.14)$$

Eqn. (5.14) is the least squares problem, whose solution is given by:

$$\begin{aligned} \hat{\beta}_1^k &= [(\mathbf{X}_1^k)^T \mathbf{X}_1^k]^{-1} (\mathbf{X}_1^k)^T \mathbf{F}_1 \\ \hat{\beta}_2^k &= [(\mathbf{X}_2^k)^T \mathbf{X}_2^k]^{-1} (\mathbf{X}_2^k)^T \mathbf{F}_2 \end{aligned} \quad (5.15)$$

The BDP estimate of the contact point obtained by performing a line search on the sum of squared residuals (SSR), and is given by:

$$\hat{k} = \arg \min_{1 < k < n} SSR \quad (5.16)$$

where

$$SSR = \|\mathbf{F}_1^k - \mathbf{X}_1^k \hat{\beta}_1^k\|^2 + \|\mathbf{F}_2^k - \mathbf{X}_2^k \hat{\beta}_2^k\|^2 \quad (5.17)$$

### 5.6.2 Continuity-constrained weighted BDP approach

In the unconstrained BDP approach discussed in section 5.6.1[1], no continuity is considered at the changepoint, i.e.  $\beta_{21}$  is not necessarily equal to  $\beta_{11} + \delta_k \beta_{12}$ .

Not enforcing continuity did not significantly impact the contact point estimate in chapter 4<sup>7</sup>, primarily because the contact model fitted the post-contact deflection data well. For sharply nonlinear force curves for which no contact model exists, it is unlikely that the contact estimation would be accurate.

As a result, a modification to the BDP approach is proposed, with continuity enforced at the contact point. This leads to the following constraint:

$$\beta_{21} = \beta_{11} + \delta_k \beta_{12} \quad (5.18)$$

Due to the constraint in Eqn. (5.18), the regression parameter space reduces to three unknowns:  $\tilde{\boldsymbol{\beta}} = [\beta_{11} \quad \beta_{12} \quad \beta_{22}]^T$ . The modified regression model from Eqn. (5.12) are given by the following equations:

$$\begin{bmatrix} F_1 \\ \vdots \\ F_k \\ F_{k+1} \\ \vdots \\ F_n \end{bmatrix} = \begin{bmatrix} 1 & \delta_1 & 0 \\ \vdots & \vdots & \vdots \\ 1 & \delta_k & 0 \\ 1 & \delta_k & f_{k+1} \\ \vdots & \vdots & \vdots \\ 1 & \delta_k & f_n \end{bmatrix} \times \begin{bmatrix} \beta_{11} \\ \beta_{12} \\ \beta_{22} \end{bmatrix} \quad (5.19)$$

---

<sup>7</sup>It might be recalled that the EIV-Bayesian Changepoint implementation on simulated data (section 4.4.2) yielded the posterior mean of the contact point within 3 datapoints of the ground truth.



In vector form, these equations are given as:

$$\underbrace{\mathbf{F}}_{n \times 1} = \underbrace{\tilde{\mathbf{X}}^k}_{n \times 3} \underbrace{\tilde{\boldsymbol{\beta}}^k}_{3 \times 1}$$

Since the contact model  $f_i$  is unlikely to fit the entire post-contact force data for highly nonlinear force curves, weights are added to the residuals of the regression model to restrict the fitting range near the contact transition. This is accomplished by defining a diagonal weight matrix  $\mathbf{W}^k = \text{diag}(\sqrt{w_{11}^k}, \sqrt{w_{22}^k}, \dots, \sqrt{w_{nn}^k})$  where  $\mathbf{W}^k \in \mathbb{R}^{n \times n}$ .

The weights are assumed Gaussian, and are given as follows:

$$w_{ii} = w_0 e^{-\frac{1}{2\sigma_w^2}(i-k)^2} \quad (5.20)$$

Note the dependence of the weights around the candidate contact point  $k$  - this ensures that the contact transition is captured by the regression model.

Similar to the unconstrained BDP approach, the optimal regression coefficient estimate  $\hat{\tilde{\boldsymbol{\beta}}}^k$  for a given contact point  $k$  is given by:

$$\hat{\tilde{\boldsymbol{\beta}}}^k = \arg \min_{\tilde{\boldsymbol{\beta}}} \|\mathbf{W}^k(\mathbf{F} - \tilde{\mathbf{X}}^k \tilde{\boldsymbol{\beta}})\|^2 \quad (5.21)$$

The weighted least squares solution  $\hat{\tilde{\boldsymbol{\beta}}}^k$  is given by:

$$\hat{\tilde{\boldsymbol{\beta}}}^k = [(\tilde{\mathbf{X}}^k)^T (\mathbf{W}^k)^T \mathbf{W}^k \tilde{\mathbf{X}}^k]^{-1} (\tilde{\mathbf{X}}^k)^T \mathbf{W}^k \mathbf{F} \quad (5.22)$$

The constrained BDP estimate of the contact point obtained by performing a line search on the sum of squared residuals (SSR) and is given by:

$$\hat{k} = \arg \min_{1 < k < n} SSR \quad (5.23)$$

where

$$SSR = ||(\mathbf{F} - \tilde{\mathbf{X}}^k \hat{\boldsymbol{\beta}}^k)||^2 \quad (5.24)$$

### 5.6.3 Choice of $f_i$ for automated data analysis

Central to both BDP model (with and without continuity constraint) is the post-contact regression model denoted by  $f_i$ . As discussed previously, analytical force-indentation relationships are not available beyond neo-Hookean hyperelasticity. In this context, it must be noted that the need to estimate the contact point and estimate hyperelastic material parameters (using inverse FE) arises only when there is prominent hyperelasticity in the force curves - otherwise, the proposed approach in chapter 4 suffices in accurately quantifying mechanical properties from AFM force curves.

It therefore seems prudent to use Dimitriadis's force-indentation relationship as  $f_i$  in the BDP approaches suggested in sections 5.6.1 and 5.6.2. Using Dimitri-

adis's model [44],  $f_i$  is given by:

$$f_i = \begin{cases} 0 & \text{if } i \leq k \\ (\delta_i - \delta_k)^{1.5} + 1.133\sqrt{\gamma}(\delta_i - \delta_k)^2 + 1.283\gamma(\delta_i - \delta_k)^{2.5} & \text{if } k + 1 \leq i \leq n \\ +0.769\gamma\sqrt{\gamma}(\delta_i - \delta_k)^3 + 0.0975\gamma^2(\delta_i - \delta_k)^{3.5} & \end{cases} \quad (5.25)$$

where  $\gamma = R/h^2$ . If Dimitriadis's model fit ( $R_{Dim}^2$ ) exceeds a threshold ( $R_{Dim,thresh}^2$ ) after the contact point is established either using the regular BDP or the constrained weighted BDP approach, no inverse FE analysis is required since the force curve represents linear elasticity in the material, which is adequately captured using Dimitriadis's model. In the case where the post-contact fit to Dimitriadis's model is poor, inverse FE estimation is invoked with the Dimitriadis's solution as the initial condition, which is terminated when the  $R_{FE}^2$  reaches the threshold  $R_{FE,thresh}^2$ . A pseudocode describing the proposed automation strategy is given in below (Algorithm 1).

## 5.7 Results

In this section, the algorithm shown in Algorithm 1 is implemented on AFM force curves of varying degrees of elasticity. The proposed approach is first validated on simulated force curves. Then, the performance of the proposed approach is demonstrated on a tissue elastic map.

**input** : AFM force curve,  $R_{Dim,thresh}^2, R_{FE,thresh}^2$ .  
**output**: Material parameters.

Multiply deflection with probe spring constant to obtain force;

**Contact Estimation:** Estimate contact point using BDP based approaches;

**Dimitriadis Curve fitting:** Fit  $F - \Delta$  to Dimitriadis's contact model to obtain  $E_{Dim}$ ,  $R_{Dim}^2$ ;

**if**  $R_{Dim}^2 > R_{Dim,thresh}^2$  **then**

    | **Linear Elasticity:** Estimated material parameter:  $\hat{E} \leftarrow E_{Dim}$ ;

**else**

    | **Hyperelasticity:**

**end**

initialize  $C_0 \leftarrow E_{Dim}/6$ ,  $b \leftarrow 30$ ;

Invoke **Inverse FE** routine with  $R_{FE,thresh}^2$ ;

Estimated material parameters:  $\hat{E}_0 \leftarrow 6\hat{C}_0$ ,  $\hat{b}$ ;

**Algorithm 1:** Pseudocode for automated force curve analysis

### 5.7.1 Parameter reidentification on simulated force curves

Three AFM force curves (S1-S3) are simulated with varying degrees of hyperelasticity. The parameters used to construct force curves are given in Table 5.2. Additionally, the force values were perturbed by Gaussian noise [ $\sim N(0, 0.05)$ ]. The threshold parameters  $R_{Dim,thresh}^2$  and  $R_{FE,thresh}^2$  were set to 0.980 and 0.999 respectively.

Table 5.2: Parameters used to construct the simulated force curves.

	(Contact $k$ , Datapoints $n$ )	Inden- tation	Linear Elastic Modulus	Hyperelastic Parameters ( $E_0, b$ )
Force Curve S1	(501,900)	400 nm	200 kPa	×
Force Curve S2	(501,900)	400 nm	×	(65 kPa,60)
Force Curve S2	(501,900)	400 nm	×	(45 kPa,120)

Performance of the unconstrained BDP [1] and continuity-constrained weighted BDP methods applied to force curves S1, S2 and S3 are shown in Fig. 5.14. The

weighting parameters used were  $w_0 = 30, \sigma_w = 3$ . In addition, the performance of the continuity-constrained weighted BDP is investigated without additional weights, i.e.  $\mathbf{W}^k = I$ , where  $I$  is the identity matrix. It is clear from Fig. 5.14(a-c) that when the material is linearly elastic, all three approaches produce close contact estimates compared to the ground truth (501<sup>th</sup> datapoint). This is primarily because the Dimitriadis contact model, i.e. [44] produces an elastic response - which was used to obtain force curve S1. The unconstrained BDP estimate [Fig.5.14(a)] can be further corrected using a Bayesian Changepoint scheme, (as demonstrated in chapter 4) and it is likely that the 95% confidence intervals will contain the ground truth.

With increasing hyperelasticity in force curves S2 and S3, it is evident that the performance of all three approaches degrade. However the continuity-constrained weighted BDP approach significantly outperforms the other two approaches. This is primarily because the fitting range is restricted by the assigned weights. In the absence of any weights, the continuity constrained BDP still outperforms the unconstrained BDP approach, however the estimation error is significant.

One of the shortcomings of the continuity-constrained weighted BDP approach is that weights require to be tuned to produce correct estimates of the contact point for sharply nonlinear force curves. It is possible to reduce the contact estimation error in Fig. 5.14(h) further by increasing the weights, however, very large weights ( $\sigma_i < 3$ ) tends to yield false minimas in the sum of squared residuals (SSR) function. Typically,  $w_0 = 30, \sigma_w = 3$  works optimally for force curves with moderate to large nonlinear elasticity (such as force curve S2) in the force curves. For force curves

such as S3 with very large  $b$ , however, this contact estimation error is inevitable using the current approaches.

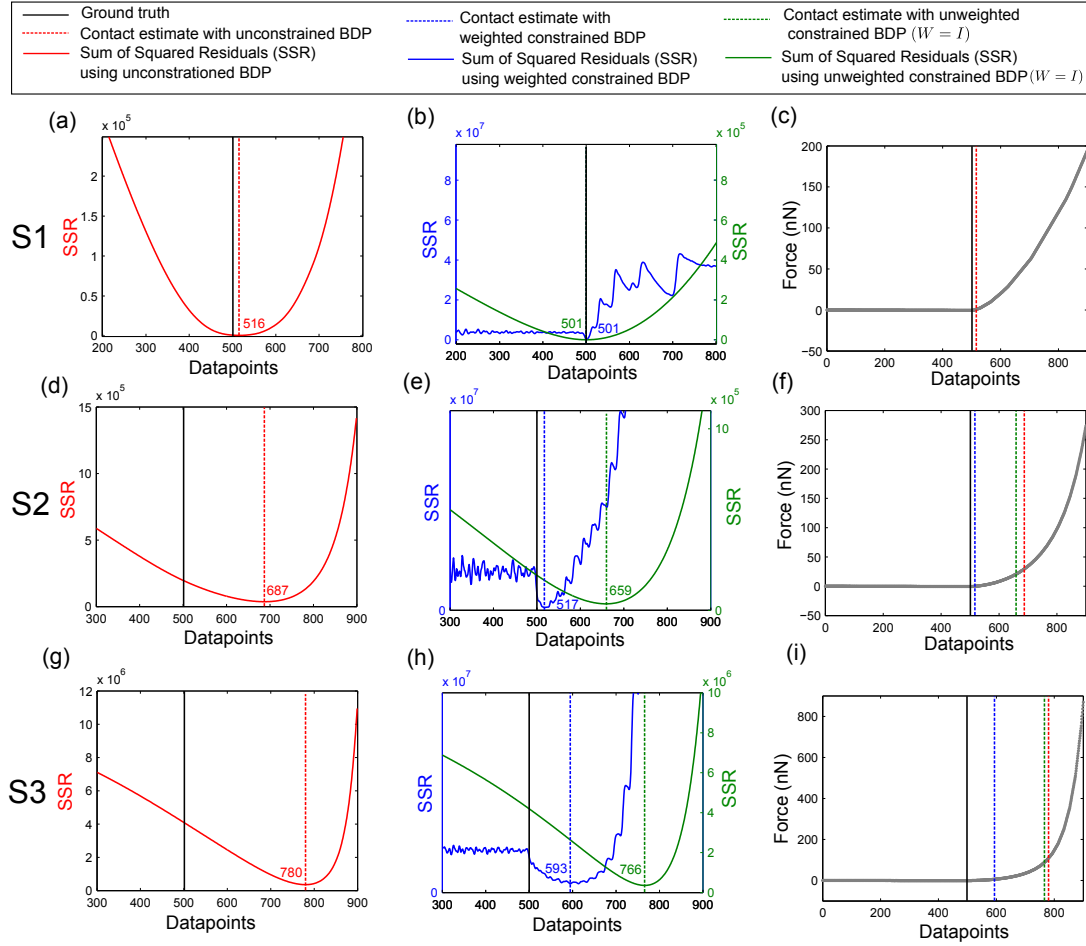


Figure 5.14: Performance of the three contact estimation methods for simulated force curves S1 - S3 (shown row-wise). The first column shows the sum of squared residuals (SSR) using unconstrained BDP (red) for force curves S1-S3 (a),(d),(g) respectively. The second column shows SSR variations using constrained BDP (blue and green) for S1-S3 (b),(e),(h) respectively. The third column shows the corresponding contact point on the force curves S1-S3 (c),(f),(i) respectively. The contact point estimates using the unconstrained and constrained BDP approaches are also shown at the base of the SSR curve.

Fig. 5.15 shows the Dimitriadis curve fitting and inverse FE solution steps of the proposed automation strategy. The continuity-constrained weighted BDP method is chosen for contact estimation since it outperforms the unconstrained BDP

and the unweighted continuity-constrained BDP. For force curve S1, the Dimitriadis contact model produces a very good fit and therefore invocation of the inverse FE routine is not necessary. For force curves S2 and S3, the inverse FE routine is invoked. The estimated  $E_0$  and  $b$  from the inverse FE are very close to the ground truth values for force curve S2. For S3 however, there is an estimation error of 100%, which is a direct consequence of the contact estimation error.

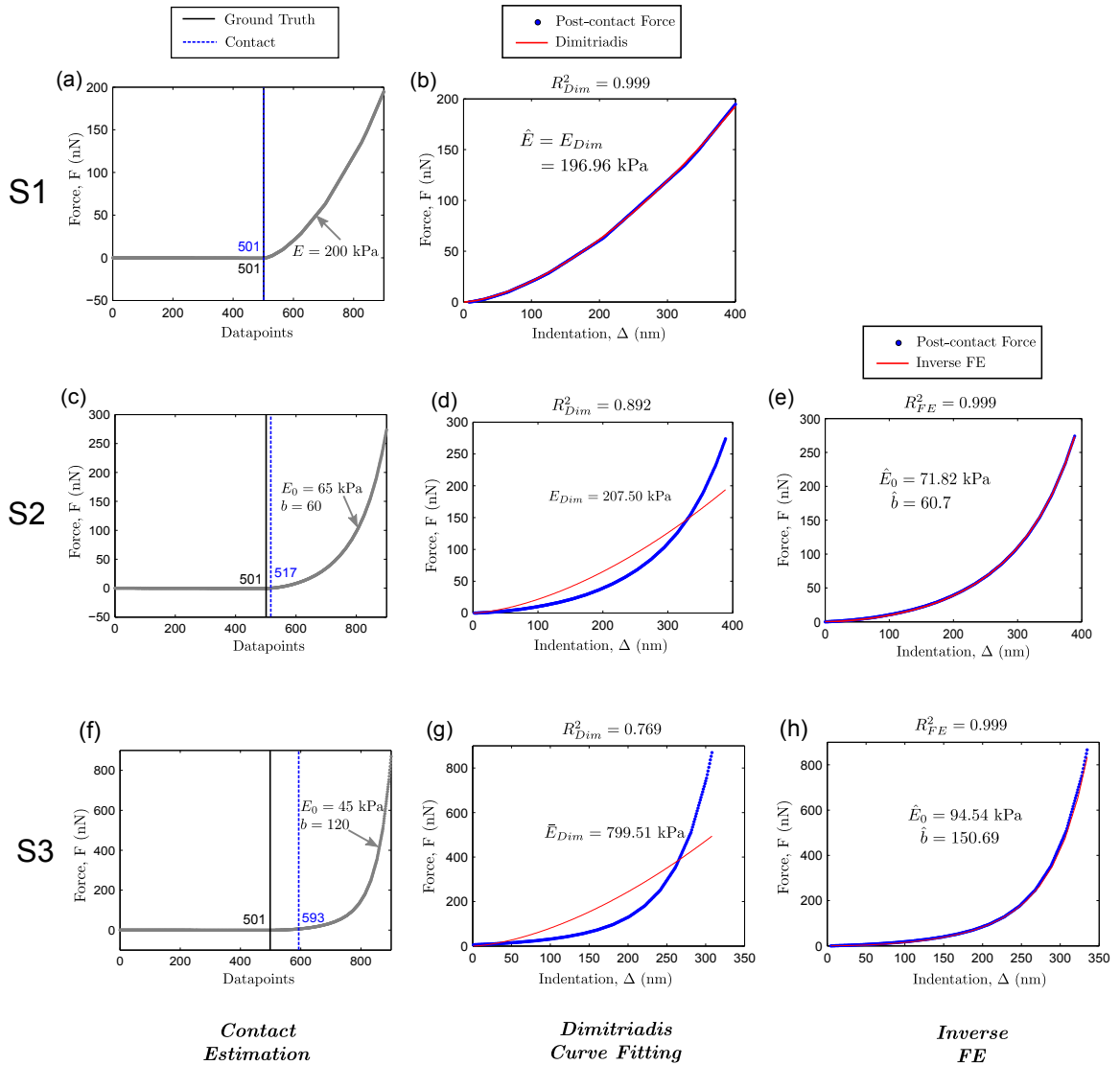


Figure 5.15: Implementation of the proposed algorithm for automated characterization for simulated force curves S1 - S3 (shown row-wise). Note that the inverse FE correction step was not required for curve S1.

The estimated parameters for all three force curves S1-S3 are tabulated in Table 5.3.

Table 5.3: Summary of algorithm performance on force curves S1-S3. Units of  $E$  and  $E_0$  are in kPa. G.T. indicates ground truth.

Force Curve	Contact Point $k$		Material Parameters					
	G.T. ( $k$ )	( $\hat{k}$ )	G.T. ( $E$ )	( $\bar{E}_{Dim}$ )	G.T. ( $E_0$ )	( $\hat{E}_0$ )	G.T. ( $b$ )	( $\hat{b}$ )
S1	501	501	200	196.97	$\times$	$\times$	$\times$	$\times$
S2	501	517	$\times$	$\times$	65	71.82	60	60.78
S3	501	593	$\times$	$\times$	45	94.54	120	150.69

### 5.7.2 Implementation on elastic map

In Fig. 5.3, an elastic map on a tissue ROI was shown where the spatial distribution of the fit quality ( $R^2$ ) was not uniform throughout. The proposed algorithm for automated characterization (Algorithm 1) is implemented on all the force curves acquired in the elastic map to investigate if the inverse-FE correction yields more accurate characterization results. Due to the computational cost involved for the inverse-FE routine, a modest termination criteria for the inverse-FE procedure was set ( $R_{FE,thresh}^2 = 0.992$ ), while  $R_{Dim,thresh}^2 = 0.980$  was used for detecting linear elasticity in the force curve.

In Fig. 5.16, the implementation of the proposed algorithm is shown. Fig. 5.16(a) shows the elastic modulus when no inverse FE corrections are implemented, i.e. the Dimitriadis model is used to fit all the force curves after the contact point is estimated using the continuity-constrained weighted BDP approach. The spatial distribution of the corresponding ( $R^2$ ) in Fig. 5.16(b) shows that the fit quality is still



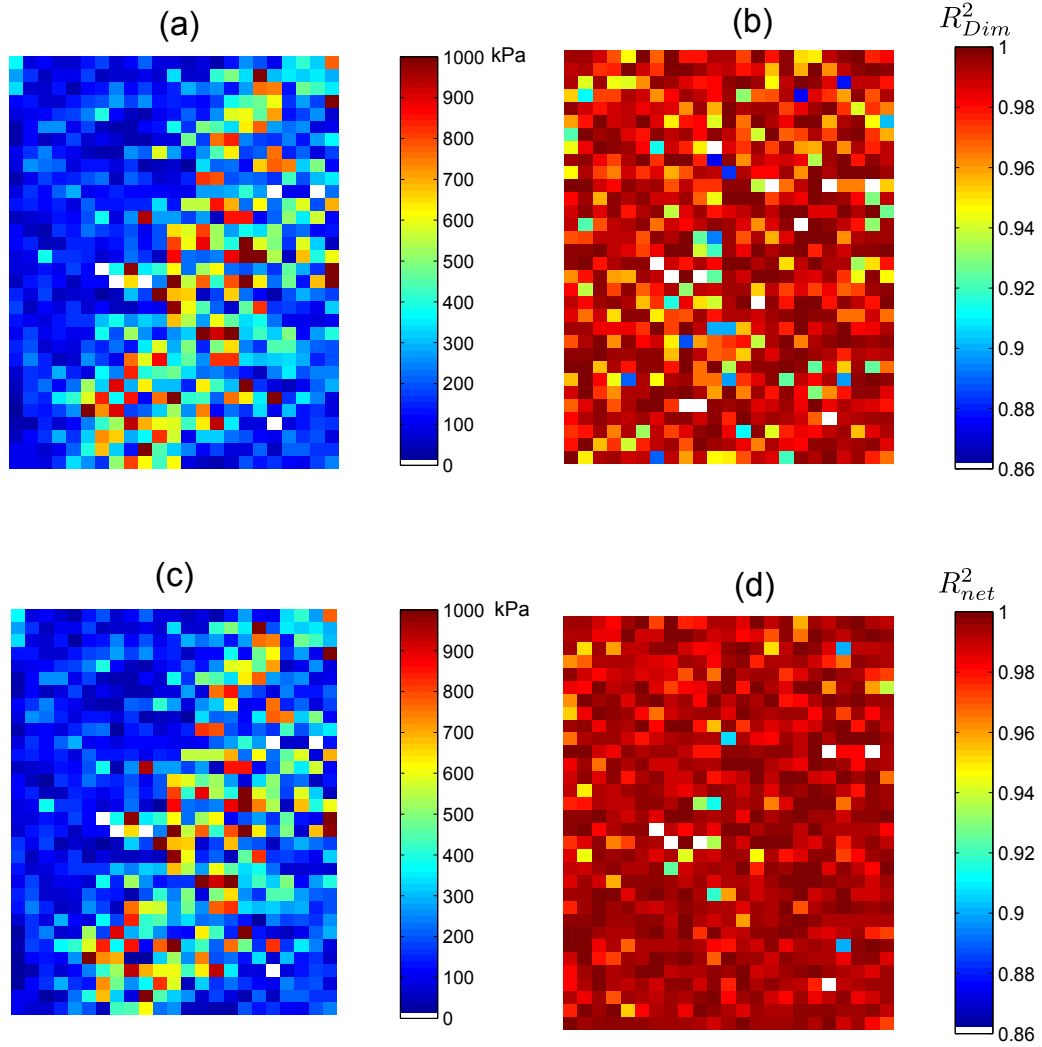


Figure 5.16: Implementation of the proposed algorithm for automated characterization on a tissue ROI shown previously in Fig. 5.3. (a) Elastic map using the Dimitriadis model only without any Inverse FE corrections, (b) Corresponding post-contact  $R_{Dim}^2$  fit, (c) Elastic map ( $\hat{E}$ ) with inverse-FE correction, (d) Corresponding  $R_{net}^2$  fit, where  $R_{net}^2 = \max(R_{Dim}^2, R_{FE}^2)$ . White spaces indicate force curves that were not analyzed due to presence of multiple potential contact points such as those in Fig. 5.7.

non-uniform. When the inverse FE correction is implemented, it becomes apparent that the ( $R^2$ ) distribution improves significantly, because force curves with material nonlinearity are now accounted for using Fung’s hyperelastic parameters.

In the elastic map, there were a few force curves that displayed multiple contact points, as shown previously in Fig. 5.7. These force curves were not analyzed and their corresponding pixel location in the elastic map and  $R^2$  distribution have been marked with blank white spaces.

Fig. 5.17 shows the estimated Fung parameter  $b$  as a function of the estimated indentation, computed using the inverse-FE routine. The inverse-FE routine was invoked for correcting 268 force curves out of a total of 729 in the elastic map shown in Fig. 5.16(a). Also shown in bold red is the predicted value  $b_{0.992}^{max}$  for a linearly elastic response, as obtained from the sensitivity study. It can be seen from Fig. 5.17(a) and Fig. 5.17(b) that hyperelastic force curves can be clearly differentiated from the predicted linear elastic response (classification curve in bold red). This would not have been possible without invocation of the inverse FE-routine.

On closer examination of Fig. 5.17(b), it becomes apparent that there was a significant population of force curves that showed very low values ( $\sim 0.001 - 0.1$ ) in the estimated parameter  $\hat{b}$ . One such representative force curve is shown in Fig. 5.18. These force curves show surprisingly linear force-indentation curves, which is probably due to material softening during the AFM loading. These force curves did not fit well even after invocation of the inverse-FE routine.

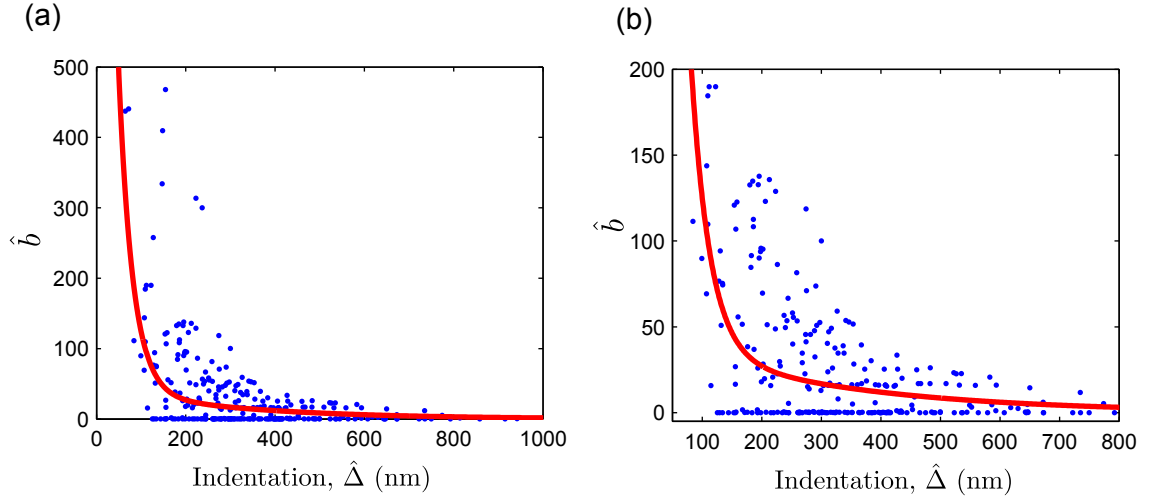


Figure 5.17: (a) Variation of estimated Fung parameter  $\hat{b}$  from the Inverse FE analysis as a function of the estimated indentation (using the contact estimate), (b) zoomed image. Also overlaid in red is  $b_{0.992}^{max}(\Delta)$ .

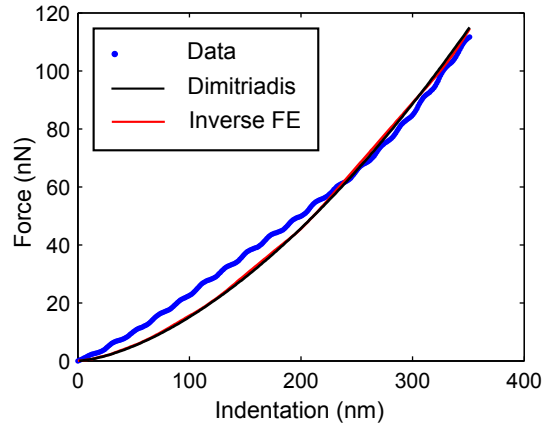


Figure 5.18: Representative force-indentation plot with low estimated  $b$  value  $(\hat{E}_0, \hat{b}) = (153.21 \text{ kPa}, 0.005)$  with  $R_{FE}^2 = 0.977$ . The Dimitriadis solution was  $\bar{E}_{Dim}$  was 146.14 kPa with  $R_{Dim}^2 = 0.975$ .

## 5.8 Conclusions

AFM characterization studies on normal and cancerous breast tissue specimens for histopathological inference necessitates very large scale AFM indentation data acquisition and processing. In this chapter, some of the key issues in automating AFM data analysis on spatially heterogeneous tissue specimens were addressed. The major highlights of this chapter are enumerated as follows:

1. The applicability of the Hertz contact model in extracting elastic modulus from AFM force curves on tissue specimens were highlighted and existing research that overcame Hertzian limitations were reviewed.
2. To account for hyperelasticity beyond neo-Hookean approximation, the Fung type phenomenological hyperelastic model was proposed to extract material properties from highly nonlinear force curves.
3. Through a sensitivity study, bounds of the Fung model parameter  $b$  was obtained that approximated a linear elastic tissue response.
4. A modified version of the BDP contact estimation algorithm[1] was proposed, that could estimate the contact point accurately in nonlinear force curves.
5. An automation strategy was proposed that could accurately estimate material properties and the contact point from simulated force curves with varying degrees of hyperelasticity.
6. On implementation on an entire ROI, it was observed that the proposed automation strategy could significantly improve fit quality in the elastic map of

the ROI, thereby validating the research hypothesis of this chapter.

There are some limitations associated with the proposed approach discussed in this chapter, namely:

1. In this analysis, a constant value of the indenter radius ( $R = 2.5\mu\text{m}$ ) was used. Varying the indenter size is likely to impact the results of the sensitivity studies in section 5.5.3. However, the probe bead size is unlikely to affect the major conclusions of this study, since it would still be possible to differentiate between a linear and an hyperelastic tissue response based on the estimated Fung parameter,  $\hat{b}$  from the inverse FE analysis.
2. It was observed that for force curves possessing very high degrees of hyperelasticity, the contact estimation did not perform satisfactorily. This was primarily because the force-indentation contact relationship used in the regression model was not capable of explaining very high nonlinear tissue response. Establishing a contact model for the Fung type hyperelastic materials remains a subject of future work.
3. Anisotropy of the tissue response in the direction of indentation was not considered in this work. Currently, force curves that display anisotropy (shown in Fig. 5.7) are isolated from the data analysis procedure after visually locating them. An automated strategy using multi-changepoint estimation might be a promising solution to identify and isolate these force curves in an unsupervised manner.

## Chapter 6

### Conclusions and Future Work

#### 6.1 Conclusions

This dissertation summarizes research directed towards performing accurate mechanical characterization on breast tissue specimens with the intent of establishing quantitative mechanical markers for cancer progression in the human breast. Due to variability in the tissue elasticity across patients, it is difficult to conclusively attribute mechanical signatures to the onset and progression of cancer in the tissue specimens, however, this dissertation presents extensive work that has been carried out towards achieving that goal. Several challenges were encountered while carrying out preliminary AFM characterization experiments on tissue, which served as the basis for chapter 2 of this dissertation. In the subsequent chapters 3-5, each of these challenges were carefully examined and their solutions proposed. Based on the research work done and experimental results obtained in this dissertation, the following conclusions can be made:

1. Breast tissue specimens obtained from biopsy samples are highly heterogeneous in their composition and therefore, accurate mechanical characterization should incorporate elastic map acquisitions (as discussed in chapter 3), instead of random pointwise sampling in the annotated areas of the tissue specimen (as discussed in chapter 2).

2. Obtaining representative tissue samples for quantifying mechanical property alterations in cancerous tissue compared to normal tissue is a very challenging exercise. As observed in the results in chapter 3, tissue elasticity is a strong function of the individual patient from whom the biopsies were taken. It is therefore recommended that for future characterization studies, normal and cancer cores be extracted from the same patient.
3. Stromal tissue was consistently found to be more stiff compared to epithelial regions in all the characterization experiments that were conducted. It is therefore recommended that these regions need not be sampled as much as epithelial regions for future characterization studies.
4. A probabilistic approach for tissue elastic modulus estimation provides a greater degree of certainty in the characterization results since it incorporates errors in the AFM probe calibration protocol and contact point uncertainty.
5. The direct implication of tissue heterogeneity is that AFM force curves acquired during raster-scanning need to be carefully post-processed to identify contribution of nonlinear elasticity in the force curves. Least square fitting of the raw AFM data to existing contact models is attractive from the computational point of view; however, as observed in the results in chapter 5, a single contact model does not account for all force curves obtained during raster indentations on the tissue specimens.

## 6.2 Contributions

The contributions presented in this dissertation can be summarized as follows:

1. *Development of a long range positioning system:* A semi-automated positioning system has been proposed that overcomes some of the shortcomings of using manual tissue-AFM probe alignment and manual registration methods. Using image feedback, it was demonstrated that tissue ROIs beyond the range of conventional AFM X-Y stages could be raster-scanned. It was also shown that manual registration needed to be performed only twice during the AFM experiments using the proposed system, in contrast to repetitive manual registration that needed to be periodically carried out to ensure that the probe was localized correctly with the stained image.
2. *EIV-Bayesian Changepoint algorithm:* An integrated probabilistic approach for estimating material properties from raw AFM data after incorporating errors in contact estimation and AFM probe spring constant calibration variability was proposed. It was shown through extensive analysis that the algorithm responded satisfactorily to varying degrees of calibration errors and the accuracy of the results was validated on simulated AFM force curves.
3. *Hyperelastic constitutive modeling of breast tissue:* It is generally the practice for AFM data analysis procedures to curve-fit bulk AFM data to analytical contact models. While computationally inexpensive, might lead to inaccurate estimates of the tissues' elastic modulus when the tissue response is sharply



nonlinear. Using finite element modeling techniques, it was shown possible to account for material nonlinearity through an exponential hyperelastic material model, which significantly improved characterization accuracy.

### 6.3 Future Work

The possible directions for future work in this area are:

1. *Characterization of stained tissue specimens:* In this dissertation, AFM-based tissue characterization was restricted to unstained tissue specimens to preclude any tissue alterations due to staining. If stained tissue response parallels those in unstained tissue, then stained tissue specimens could be used for characterization. This would additionally aid in manual registration of the annotated images with the tissue used for AFM probing.
2. *Characterization of normal and cancerous specimens from the same patient:* Future work might be directed towards patient-specific characterization of normal and cancerous tissue specimens.
3. *Automated registration:* Further throughput improvement with AFM characterization could be achieved if the stained annotations could be automatically registered with the tissue used for AFM probing. This can be performed using multimodal registration techniques.
4. *Non-parametric contact estimation:* In the contact estimation strategies proposed in chapters 4 and 5, an explicit contact model needed to be used. Con-

tact estimation strategies that do not require a contact model might be particularly attractive for estimating the contact point in force curves that are not described by existing contact models.

5. *Integrated computational framework for tissue characterization:* In this dissertation, the various steps involved in AFM characterization (probe spring constant, contact estimation and tissue constitutive modeling) were treated in a piecemeal manner. This was primarily because the EIV-Bayesian Change-point algorithm (in chapter 4) required an explicit contact model and there were no such models for highly nonlinear force curves, as seen in chapter 5. Future work might be directed towards developing contact models for exponential hyperelastic response on the lines of those proposed by Lin *et al.* [74] which also accounts for finite-indentation. This would allow uncertainty quantification of the tissue properties using the probabilistic tools developed in chapter 4. Confidence intervals thus generated could be used in interval-uncertainty incorporated hypothesis tests, as suggested in [56] for inference purposes.

The experimental and computational strategies proposed in this dissertation could have a significant impact on high-throughput quantitative studies of biomaterials, which could elucidate various disease mechanisms that are phenotyped by their mechanical signatures.

## Appendix A

### Finite indentation response of Hertz and Dimitriadis contact models

In this appendix, the ability of Hertz and Dimitriadis contact models to account for finite indentation on thin specimens is investigated by comparing it with a finite element (FE) response.

Simulated contact forces obtained by performing spherical indentation on a linearly elastic FE model of a tissue specimen  $4\mu\text{m}$  thick with varying elastic modulus  $E$  (from 10 kPa to 2500 kPa) were fitted with Dimitriadis and Hertz contact models, resulting in the fitted moduli  $E_{Dim}$  and  $E_{Hertz}$  respectively. The normalized parameters  $E_{Dim}/E$  and  $E_{Hertz}/E$  were obtained for varying indentation depth (from  $\Delta = 50\text{ nm}$  to  $\Delta = 1400\text{ nm}$ ). Two probe bead sizes  $R = 2.5\mu\text{m}$  and  $R = 5.0\mu\text{m}$  were used for investigating the impact of indenter size on predictions from Hertz and Dimitriadis contact models.

Fig. A.1 summarizes the results of the analysis performed. Figs. A.1(a) shows the variation of  $E_{Hertz}/E$  and  $E_{Dim}/E$  for a probe bead radius of  $R = 2.5\mu\text{m}$  with increasing indentation depth and the corresponding fit quality ( $R^2$ ) is shown in Fig. A.1(b). It becomes clear that the Hertz model significantly overestimates the elastic modulus with increasing indentation depth due to the violation in infinitesimal assumptions. The corresponding fit quality too shows deteriorates with increasing indentation. The overestimation in the Hertz response worsens further

for a larger bead size of  $R = 5.0 \mu\text{m}$  [Figs. A.1(c) and (d)].

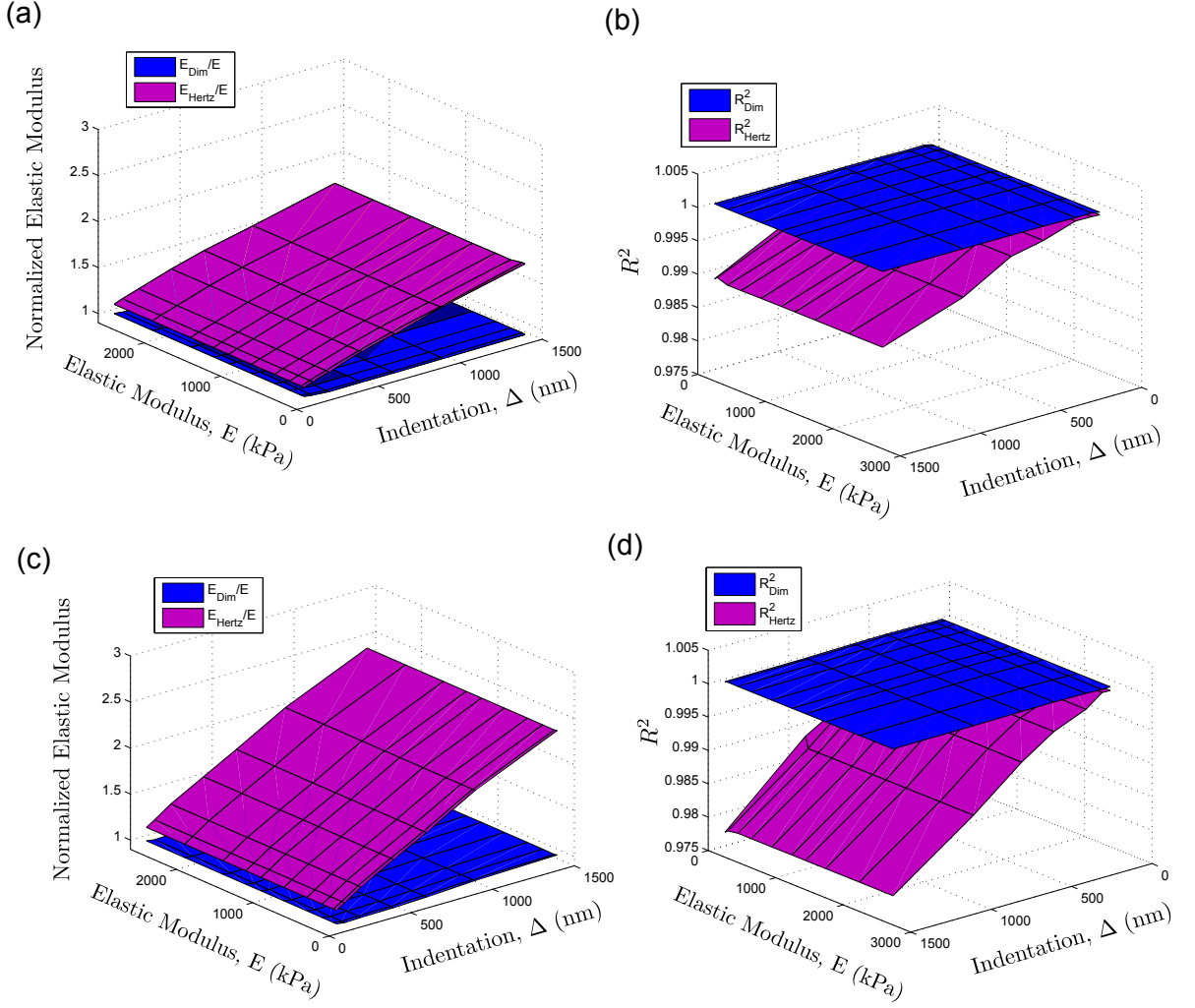


Figure A.1: (a) Variation of  $E_{Hertz}/E$  and  $E_{Dim}/E$  for  $R = 2.5 \mu\text{m}$ , (b) Corresponding  $R^2$  fit quality, (c) Variation of  $E_{Hertz}/E$  and  $E_{Dim}/E$  for  $R = 5.0 \mu\text{m}$  and (d) Corresponding  $R^2$  fit quality.

In contrast, it is clear that for both bead sizes, the Dimitriadis model accurately estimates the elastic modulus ( $E_{Dim}/E \sim 1$ ) for shallow as well as deep indentations. This analysis conclusively proves the applicability of Dimitriadis model in estimating tissue elastic modulus from AFM indentation on thin specimens such as the breast tissue specimens studied in this work.

## Bibliography

- [1] K.D. Costa, A.J. Smith, and F.C.P. Yin. Non-Hertzian Approach to Analyzing Mechanical Properties of Endothelial Cells Probed by Atomic Force Microscopy. *Journal of Biomechanical Engineering*, 128(2):176–184, 2006.
- [2] P.P. Rosen. *Rosen’s Breast Pathology*. Lippincott Williams & Wilkins, third edition, 2008.
- [3] Cancer facts & figures 2013. *Atlanta: American Cancer Society*, 2013.
- [4] D.J. Foran, W. Chen, and L. Yang. Automated image interpretation and computer-assisted diagnostics. *Analytical Cellular Pathology*, 34:279–300, 2011.
- [5] J Ophir, S K Alam, B Garra, F Kallel, E Konofagou, T Krouskop, and T Varghese. Elastography: ultrasonic estimation and imaging of the elastic properties of tissues. In *In Proc. Instn. Mech. Engrs., Part H: Journal of Engineering in Medicine*, pages 203–233, 1999.
- [6] A. Manduca, T.E. Oliphant, M.A. Dresner, J.L. Mahowald, S.A. Kruse, E. Amromin, J.P. Felmlee, J.F. Greenleaf, and R.L. Ehman. Magnetic resonance elastography: non-invasive mapping of tissue elasticity. *Medical Image Analysis*, 5(4):237–254, 2001.
- [7] A.J. Fredman, J.L. Frolik, and B.S. Garra. Lung strain profiles using computed tomography elastography. In *Annual Conference Proceedings of IEEE Engineering in Medicine and Biology Society*, pages 1545–1548, 2004.
- [8] K.D. Costa. Single-cell elastography: Probing for disease with the atomic force microscope. *Disease Markers*, 19(2):139–154, 2003.
- [9] Q.S. Li, G.Y.H. Lee, C.N. Ong, and C.T. Lim. AFM indentation study of breast cancer cells. *Biochem. Biophys. Res. Commun.*, 374(4):609–613, 2008.
- [10] M. Lekka, P. Laidler, D. Gil, J. Lekki, Z. Stachura, and A. Z. Hryniewicz. Elasticity of normal and cancerous human bladder cells studied by scanning force microscopy. *European Biophysics Journal*, 28(4):312–316, 1999.
- [11] S. Park, D. Koch, R. Cardenas, J. Kas, and C.K. Shih. Cell motility and local viscoelasticity of fibroblast. *Biophysical Journal*, 89:4330–4342, 2005.
- [12] J. Katsantosis, A. Tosca, S.B. Koukouritaki, P.A. Theodoropoulos, A. Gravanis, and C. Stournaras. Differences in the G/total actin ratio and microfilament stability between normal and malignant keratinocytes. *Cell Biochem Funct*, 12:267–274, 1994.

- [13] M.J. Paszek, N. Zahir, K.R. Johnson, A. Gefen, C.A. Reinhart-King, and S.S. Boettiger. Tensional homeostasis and the malignant phenotype. *Cancer Cell*, 8(3):241–254, 2005.
- [14] G.J. Mizejewski. Role of integrins in cancer: survey of expression patterns. In *Proceedings of the Society for Experimental Biology and Medicine*, pages 124–138, 1999.
- [15] D.T. Butcher, T. Alliston, and V.M. Weaver. A tense situation: forcing tumour progression. *Nature Rev. Cancer*, 9(2):108–122, 2009.
- [16] J. Kononen, L. Bubendorf, A. Kallionimeni, M. Brlund, P. Schraml, S. Leighton, J. Torhorst, M.J. Mihatsch, G. Sauter, and O.P. Kallionimeni. Tissue microarrays for high-throughput molecular profiling of tumor specimens. *Nature Medicine*, 4:844–847, 1998.
- [17] D. Kim, P.K. Wong, J. Park, A. Levchenko, and Y. Sun. Microengineered platforms for cell mechanobiology. *Annual Review of Biomedical Engineering*, 11:202–233, 2009.
- [18] A. Alessandrini and P. Facci. AFM : a versatile tool in biophysics. *Measurement Science and Technology*, 16:R65–R92, 2005.
- [19] A. Pillarisetti. *Mechanical Characterization and Manipulation of Biological Cells*. PhD thesis, University of Maryland, College Park, 2008.
- [20] W. Chen and D.J. Foran. Advances in tissue microarray technology: Towards improved understanding and diagnosis of cancer. *Anal. Chim. Acta*, 564:74–81, 2006.
- [21] W. Chen, D.J. Foran, and M. Reiss. Unsupervised imaging, registration and archiving of tissue microarrays. In *Proceedings of AMIA Symp*, pages 136–139, 2002.
- [22] W. Chen, D.J. Foran, and M. Reiss. A prototype for unsupervised analysis of tissue microarrays for cancer research and diagnostics. *IEEE Transactions on Information Technology in Biomedicine*, 8:89–96, 2004.
- [23] L. Yang, O. Tuzel, W. Chen, P. Meer, G. Salaru, L.A. Goodell, and D.J. Foran. Pathminer: A web-based tool for computer-assisted diagnostics in pathology. *IEEE Transactions on Information Technology in Biomedicine*, 13(3):291–299, 2009.
- [24] A. Pillarisetti, J.P. Desai, H. Ladjal, A. Schiffmacher, A. Ferreira, and C.L. Keefer. Mechanical phenotyping of mouse embryonic stem cells: increase in stiffness with differentiation. *Cellular Reprogramming*, 13(4):261–269, 2009.
- [25] J.L. Hutter and J. Bechhoeffer. Calibration of atomic-force microscope tips. *Review Sci. Instrum.*, 64(7):1868–1873, 1993.

- [26] K.L. Johnson. One hundred years of hertz contact. *Proc Instn Mech Engrs*, 196(1):363–378, 1982.
- [27] J.E. Sader, I. Larson, P. Mulvaney, and L.R. White. Method for the calibration of atomic force microscope cantilevers. *Rev. Sci. Instrum.*, 66(7):3789–3798, 1995.
- [28] R.S. Gates and J.R. Pratt. Accurate and precise calibration of AFM cantilever spring constants using laser Doppler vibrometry. *Nanotechnology*, 23(37):1–12, 2012.
- [29] David C. Lin, Emiliós K. Dimitriadis, and Ferenc Horkay. Robust Strategies for Automated AFM Force Curve Analysis-I. Non-adhesive Indentation of Soft, Inhomogeneous Materials. *Transactions of the ASME*, 129(3):430–440, 2007.
- [30] A.S. Naini, R.V. Patel, and A. Samani. Measurement of Lung Hyperelastic Properties Using Inverse Finite Element Approach. *IEEE Transactions on Biomedical Engineering*, 58(10):2852–2859, 2011.
- [31] H. Hagaa, S. Sasakia, K. Kawabataa, E. Itob, T. Ushikic, and T. Sambongia. Elasticity mapping of living fibroblasts by AFM and immunofluorescence observation of the cytoskeleton. *Ultramicroscopy*, 82(1-4):253–258, 2000.
- [32] J. Shi and C. Tomasi. Good features to track. In *Computer Vision and Pattern Recognition*, pages 593–600, 1994.
- [33] D.G. Lowe. Distinctive Image Features from Scale-Invariant Keypoints. *International Journal of Computer Vision*, 60(2):91–110, 2004.
- [34] M.S. Nixon and A.S. Aguado. *Feature Extraction & Image Processing*. Academic Press, second edition, 2008.
- [35] Gary Bradski and Adrian Kaehler. *Learning OpenCV*. 2008.
- [36] Y. Sun and B. Nelson. Biological Cell Injection Using an Autonomous MicroRobotic System. *The International Journal of Robotics Research*, 21(10-11):861–868, 2002.
- [37] F. Liu and D.J. Tschumperlin. Micro-mechanical characterization of lung tissue using atomic force microscopy. *Journal of Visualized Experiments*, 54(2911), 2011.
- [38] B. Capella, P. Baschieri, C. Frediani, P. Miccoli, and C. Ascoli. Force-Distance Curves by AFM. *IEEE Engineering in Medicine and Biology*, 16(2):58–65, 1997.
- [39] M.F. Jaasma, W.M. Jackson, and T.M. Keaveny. Measurement and Characterization of Whole-Cell Mechanical Behavior. *Annals of Biomedical Engineering*, 34(5):748–758, 2006.

- [40] L.R. Nyland and D.W. Maughan. Morphology and transverse stiffness of drosophila myofibrils measured by atomic force microscopy. *Biophysical Journal*, 78(3):1490-1497, 2000.
- [41] M. Radermacher. Measuring the elastic properties of living cells by the atomic force microscope. *Methods Cell Biol*, 68:67–90, 2002.
- [42] G.T. Charras, P.P. Lehenkari, and M.A. Horton. Atomic force microscopy can be used to mechanically stimulate osteoblasts and evaluate cellular strain distributions. *Ultramicroscopy*, 86:85–95, 2001.
- [43] M. Radmacher, M. Fritz, C. Kacher, J. Cleveland, and P. Hansma. Measuring the Viscoelastic Properties of Human Platelets with the Atomic Force Microscope. *Biophysical Journal*, 70(1):556–567, 1996.
- [44] E.K. Dimitriadis, F. Horkay, J. Maresca, B. Kachar, and R.S. Chadwick. Determination of elastic moduli of thin layers of soft material using the atomic force microscope. *Biophysical Journal*, 82(5):2798–2810, 2002.
- [45] S.L. Crick and F.C.-P. Yin. Assessing Micromechanical Properties of Cells with Atomic Force Microscopy: Importance of the Contact Point. *Biomechanics and modeling in Mechanobiology*, 6(3):199–210, 2007.
- [46] Pavel Polyakov, Charles Soussen, Junbo Duan, Jerome F. L. Duval, David Brie, and Gregory Francius. Automated force volume image processing for biological samples. *PLoS ONE*, 6(4):e18887, 2001.
- [47] E.A-Hassan, W.F. Heinz, M.D. Antonik, N.P. D’Costa, S. Nageswaran, C.A. Schoenenberger, and J.H. Hoh. Relative microelastic mapping of living cells by atomic force microscopy. *Biophysical Journal*, 74(3):1564–1578, 1998.
- [48] Daniel Rudoy, Shelten G. Yuen, Robert D. Howe, and Patrick J. Wolfe. Bayesian change-point analysis for atomic force microscopy and soft material indentation. *Journal of the Royal Statistical Society: Series C*, 59(4):573–593, 2010.
- [49] J.P. Cleveland, S. Manne, D. Bocek, and P.K. Hansma. A nondestructive method for determining the spring constant of cantilevers for scanning force microscopy. *Review of Scientific Instruments*, 64:403, 1993.
- [50] A. Torii, M. Sasaki, K. Hane, and S. Okuma. A method for determining the spring constant of cantilevers for atomic force microscopy. *Measurement Science and Technology*, 7(2):179–184, 1996.
- [51] R. Proksch, T. Schaffer, J.P. Cleveland, R.C Callahan, and M.B. Viani. Finite optical spot size and position corrections in thermal spring constant calibration. *Nanotechnology*, 15(9):1344–1350, 2004.



- [52] N.A. Burnham, X. Chen, C.S. Hodges, G.A. Mateil, E.J. Thoreson, C.J. Roberts, M.C. Davies, and S.J.B. Tendler. Comparison of calibration methods for atomic-force microscopy cantilevers. *Nanotechnology*, 14(1):1–6, 2003.
- [53] T. Pirzer and T. Hugel. Atomic force microscopy spring constant determination in viscous liquids. *Review of Scientific Instruments*, 80(035110):1–6, 2009.
- [54] B. Ohler. Cantilever constant calibration using laser Doppler vibrometry. *Review of Scientific Instruments*, 78(6):063701, 2007.
- [55] D. Kiracofe and A. Raman. Quantitative force and dissipation measurements in liquids using piezo-excited atomic force microscopy: a unifying theory. *Nanotechnology*, 22:1–11, 2011.
- [56] V. Kreinovich, H.T. Nguyen, and S. Niwitpong. Statistical hypothesis testing under interval uncertainty: An overview. *International Journal of Intelligent Technology and Applied Statistics*, 1(1):1–32, 2008.
- [57] R. Roy, W. Chen, L. Cong, D.J. Foran, and J.P. Desai. Probabilistic Estimation of Mechanical Properties of Biomaterials Using Atomic Force Microscopy. *IEEE Transactions on Biomedical Engineering*, 2013.
- [58] R. Wagner, R. Moon J. Pratt G. Shaw, and A. Raman. Uncertainty quantification in nanomechanical measurements using the atomic force microscope. *Nanotechnology*, 22(45):1–9, 2011.
- [59] R. Long, M. Hall, M. Wu, and C-Y. Hui. Effects of Gel Thickness on Microscopic Indentation Measurements of Gel Modulus. *Biophysical Journal*, 101(3):642–650, 2011.
- [60] C-L. Cheng and J.W. Van Ness. *Statistical Regression with Measurement Error : Kendall’s Library of Statistics 6*. Wiley, first edition, 1999.
- [61] B.P. Carlin, A.E. Gelfand, and A.F.M. Smith. Hierarchical Bayesian Analysis of Changepoint Problems. *Journal of the Royal Statistical Society. Series C (Applied Statistics)*, 41(2):389–405, 1992.
- [62] A. Gelman, J.B. Carlin, H.S. Stern, and D.B. Rubin. *Bayesian Data Analysis*. Chapman and Hall, first edition, 1995.
- [63] D. Stephens. Bayesian Retrospective Multiple-Changepoint Identification. *Journal of the Royal Statistical Society*, 43(1):159–178, 1994.
- [64] C. Gossel and H.Kuchenoff. Bayesian analysis of logistic regression with an unknown change point and covariate measurement error. *Statistics in Medicine*, 20(3):3109–3121, 2001.

- [65] R. Roy, W. Chen, L. Cong, L.A. Goodell, D.J. Foran, and J.P. Desai. A Semi-Automated Positioning System for contact-mode Atomic Force Microscopy (AFM). *IEEE Transactions on Automation Science and Engineering*, 10(2):462–465, 2013.
- [66] K.D. Costa and F.C.P. Yin. Analysis of indentation: Implications for measuring mechanical properties with atomic force microscopy. *Journal of Biomechanical Engineering*, 121(5):462–471, 1999.
- [67] L. Sirghi, J. Ponti, F. Broggi, and F. Rossi. Probing elasticity and adhesion of live cells by atomic force microscopy indentation. *European Biophysics Journal*, 37(6):935–945, 2008.
- [68] David C. Lin, Emilios K. Dimitriadis, and Ferenc Horkay. Robust Strategies for Automated AFM Force Curve Analysis-II - Adhesion-Inuenced Indentation of Soft, Elastic Materials. *Transactions of the ASME*, 129(6):904–912, 2007.
- [69] R.E. Mahaffy, C.K. Shih, F.C. MacKintosh, and J. Kas. Scanning Probe-Based Frequency-Dependent Microrheology of Polymer Gels and Biological Cells. *Physical Review Letters*, 85(4):880–883, 2000.
- [70] J. Domke and M. Radmacher. Measuring the Elastic Properties of Thin Polymer Films with the Atomic Force Microscope. *Langmuir*, 14:3320–3325, 1998.
- [71] K. Sangpradit, H. Liu, L. Seneviratne, and K. Althoefer. Tissue Identification using Inverse Finite Element Analysis of Rolling Indentation. In *In IEEE International Conference on Robotics and Automation*, pages 1250–1255, 2009.
- [72] S. Park, K.D. Costa, and G.A. Ateshian. Microscale Frictional Response of Bovine Articular Cartilage from Atomic Force Microscopy. *Journal of Biomechanics*, 37(11):1679–1687, 2004.
- [73] J.A.C. Santos, L.M.Rebelo, A.C. Araujo, E.B. Barrosa, and J.S. de Sousa. Thickness-corrected model for nanoindentation of thin films with conical indenters. *Soft Matter*, 8(16):4441–4448, 2012.
- [74] D.C. Lin, D.I. Shreiber, E.K. Dimitriadis, and F. Horkay. Spherical indentation of soft matter beyond the Hertzian regime: numerical and experimental validation of hyperelastic models. *Biomech Model Mechanobiol*, 8:345–358, 2009.
- [75] D.C. Lin, D.I. Shreiber, E.K. Dimitriadis, and F. Horkay. Elasticity of rubber-like materials measured by AFM nanoindentation. *eXPRESS Polymer Letters*, 1(9):576–584, 2007.
- [76] D. Tabor. *The Hardness of Materials*. Clarendon Press, Oxford, first edition, 1951.

- [77] B. Oommen and K.J. Van Vilet. Effect of nanoscale thickness and elastic nonlinearity on measured properties of polymeric films. *Thin Solid Films*, 513(1-2):235–242, 2006.
- [78] H. Ladjal, J-Luc Hanus, A. Pillarisetti, C. Keefer, A. Ferreira, and J.P. Desai. Atomic Force Microscopy-Based Single-Cell Indentation: Experimentation and Finite Element Simulation. In *IEEE/RSJ International Conference on Intelligent Robots and Systems*, pages 1326–1332, 2009.
- [79] M.G. Zhong, Y.P. Cao, G.Y. Li, and X.Q. Feng. Spherical indentation method for determining constitutive parameters of hyperelastic soft materials. *Biomech Model Mechanobiol*, 2013.
- [80] M.C. Frassanito, L. Lamberti, A. Boccaccio, and C. Pappalettere. Discussion on hybrid approach to determination of cell elastic properties. In *Optical Measurements, Modeling, and Metrology, Volume 5, Conference Proceedings of the Society for Experimental Mechanics Series*, pages 119–124, 2011.
- [81] P.J. Thurner. Atomic force microscopy and indentation force measurement of bone. *Nanomedicine and Nanobiotechnology*, 1(6):624–649, 2009.
- [82] T. Yamada, Y. Kunioka, J. Wakayama, M. Aimi, Y.S. Noguchi and N. Akiyama, and T. Kayamori. Molecular organizations of myofibrils of skeletal muscle studied by atomic force microscopy. *Advances in experimental medicine and biology*, 538:285–294, 2003.
- [83] H.K. Herisa, A.K. Miria, U. Tripathy, F. Barthelata, and L. Mongeaua. Indentation of poroviscoelastic vocal fold tissue using an atomic force microscope. *Journal of the Mechanical Behavior of Biomedical Materials*, 28:383–392, 2013.
- [84] G.U. Unnikrishnan, V.U. Unnikrishnan, and J.N. Reddy. Constitutive material modeling of cell: A micromechanics approach. *ASME Journal of Biomechanical Engineering*, 129(3):315–323, 2007.
- [85] J.A. Nelder and R. Mead. A simplex method for function minimization. *Computer Journal*, 7(4):308–313, 1965.
- [86] O.H. Yeoh. Some forms of the strain energy function for rubber. *Rubber Chemistry and Technology*, 66(5):754–771, 1993.
- [87] Y.C. Fung. *Biomechanics: Mechanical Properties of Living Tissues*. Springer, second edition, 1993.